Università degli Studi di Ferrara

DOCTORAL COURSE IN:

PHYSICS

CYCLE XXXVII

COORDINATOR Prof. Paolo Lenisa

Development of Reconstruction algorithms and Truth-Matching Tools for calibration studies of the SAND Electromagnetic Calorimeter at DUNE

Scientific-Disciplinary Sector (SDS): PHYS-01/A

Ph.D candidate:
Riccardo D'Amico

Supervisors:
Prof. Eleonora Luppi
Prof. Luca Tomassetti

Academic Years 2021/2025

Abstract

The Deep Underground Neutrino Experiment (DUNE) is a next-generation long-baseline accelerator programme that will probe neutrino oscillations with unprecedented sensitivity. It will observe a high-intensity wide-band beam using a Near-Detector (ND) complex at Fermilab and a Far Detector (FD) ∼1300 km away at the Sanford Underground Research Facility. The System for on-Axis Neutrino Detection (SAND) is one of the three ND subsystems, providing continuous on-axis monitoring and supporting a broad physics programme. This work presents the design and validation of a dedicated reconstruction–clustering algorithm for the SAND electromagnetic calorimeter (ECAL), together with a truth-matching procedure that associates Monte Carlo particles with the clusters they create. The truth-matching algorithm is used to validate the reconstruction framework, yielding in simulation an ECAL energy resolution
$\sigma_E/E = (5.02 \pm 0.15)\%/\sqrt{E\ [\mathrm{GeV}]}$, and to explore an in-situ calibration strategy based on muons produced by neutrino interactions in the surrounding rock and in SAND itself.

In parallel, a cosmic-ray stand was developed and commissioned at Laboratori Nazionali di Frascati (LNF) to characterise ECAL modules under controlled conditions, providing independent measurements of ADC and TDC responses that complement and validate the simulation-based calibration studies. The tools developed here provide the foundation for a comprehensive, data-driven calibration programme for the SAND ECAL.

Contents

Introduction

Neutrino oscillations have established that neutrinos are massive particles and that lepton flavours mix, providing clear evidence of physics beyond the original formulation of the Standard Model. Over the past decades, a broad experimental programme based on solar, atmospheric, reactor and accelerator neutrinos has determined the oscillation parameters with increasing precision. Important questions, however, remain open, including the ordering of the neutrino mass eigenstates, the size of leptonic Charge conjugation and Parity (CP) violation and the impact of nuclear effects on the interpretation of long-baseline measurements. Addressing these questions requires intense and well-characterised accelerator beams, together with detectors capable of reconstructing neutrino interactions with controlled systematic uncertainties.

The Deep Underground Neutrino Experiment (DUNE) is a next-generation long-baseline accelerator programme designed to address these questions. A high-intensity neutrino beam produced at Fermilab will be observed by a Near Detector (ND) complex and by a Far Detector (FD) at a baseline of about 1300 km. The ND plays a central role in constraining the flux before oscillations and the neutrino-interaction models used in the oscillation analysis, and in monitoring the stability of the beam over the lifetime of the experiment.

Within this context, the present thesis focuses on the System for on-Axis Neutrino Detection (SAND), one of the three subsystems of the DUNE ND complex, and in particular on the calibration of its electromagnetic calorimeter (ECAL). SAND combines a solenoidal magnet, a high-granularity ECAL, a liquid-argon active target and a modular low-density target-tracker to provide a continuous on-axis characterisation of the neutrino beam. For SAND to fulfill its role as a beam monitor and near detector, the ECAL response must be calibrated and modeled with sufficient accuracy, using methods that are compatible with the underground environment and with normal beam operation.

The structure of the thesis reflects this progression from general context to specific calibration methods:

Chapter 1 reviews the phenomenology of neutrino oscillations and the current experimental status.

Chapter 2 introduces the DUNE experiment, describing the neutrino beam, the ND complex and the FD, and outlining how near-detector data are used to constrain the oscillation analysis.

Chapter 3 presents the SAND detector, detailing its main subsystems and their roles; particular attention is given to the ECAL layout, segmentation and readout, since these aspects are central to the calibration work.

Chapter 4 describes the simulation and reconstruction framework used in this

thesis. It summarises the chain from neutrino flux and interaction generators to the energy deposits in the SAND geometry, and the subsequent digitization and reconstruction of detector signals. For the ECAL, a dedicated digitization model and a reconstruction chain have been developed and integrated in the SAND analysis framework. These include clustering of digitized cells, time and energy reconstruction, basic quality controls and a truth-matching procedure that associates reconstructed clusters with Monte Carlo particles and energy deposits. This infrastructure provides the basis for performance studies and for the calibration methods discussed in the final chapter.

Chapter 5 constitutes the core of the thesis. It presents the calibration strategy for the SAND ECAL and its validation in simulation and in a dedicated test stand. On the simulation side, beam-induced muons from neutrino interactions in the surrounding rock and in SAND itself are used as an abundant source of minimum-ionising particles. Their distributions and occupancies are studied, and procedures are developed for energy calibration via the minimum-ionising peak and for timing alignment across channels, exploiting the ECAL reconstruction and truth-matching tools introduced earlier. In parallel, a preliminary vertex reconstruction based solely on calorimetric observables is implemented and its stability is examined under realistic conditions.

Complementing these studies, a cosmic-ray stand has been designed and commissioned at the INFN Frascati National Laboratories to characterise individual ECAL modules under controlled conditions. Equipped with the original KLOE readout chain and a custom data-acquisition system, the stand provides measurements of ADC and TDC responses to cosmic muons and serves as an independent test bench for the detector and for the calibration models implemented in the SAND framework. Together, these elements define and validate a practical, data-driven path to the calibration of the SAND ECAL.

Chapter 1

Neutrino physics

Among all fermions in the Standard Model, neutrinos are the most weakly interacting particles and their existence remained unsuspected until the early 20th century. The story begins with β-decay studies in the late 1920s, with the calorimetric measurements by Ellis and Wooster [1]: the emitted electron spectrum was continuous rather than discrete, contradicting expectations for a two-body decay and apparently violating energy conservation. Faced with this crisis, Wolfgang Pauli proposed in a now-legendary letter of 4 December 1930 a "desperate remedy": the emission of a new, electrically neutral, light particle in β-decay to carry away the missing energy and momentum [2]. Pauli referred to it as a neutron, but this name was reassigned in 1932 when James Chadwick discovered the heavy neutron [3]. Within a year, Enrico Fermi and his collaborators in Rome adopted the diminutive neutrino to distinguish Pauli's hypothesized particle. In 1934, Fermi published his theory of β-decay [4], embedding the neutrino into a quantitative framework of a contact weak interaction and successfully explaining the continuous spectrum. The publication of the theory was initially rejected by the journal Nature for being "too remote from reality" before appearing in Zeitschrift für Physik. Direct detection would take another two decades. In 1956, Clyde Cowan and Frederick Reines reported the observation of antineutrinos from a nuclear reactor via the inverse β-decay process [5]. Two years later, the Goldhaber experiment demonstrated that neutrinos are produced with left-handed helicity [6]. From the 1960s onward, neutrinos became probes of astrophysics and particle physics alike. In 1968, Raymond Davis Jr. and collaborators, using a radiochemical chlorine detector inspired by Pontecorvo's ideas, measured a solar electron-neutrino flux significantly lower than predicted by Bahcall's solar models [7, 8], inaugurating the solar neutrino problem. Decades later, the puzzle was resolved when the Sudbury Neutrino Observatory (SNO) in 2002 demonstrated that solar ν_e transform into ν_μ and ν_τ [9]. Meanwhile, the Super-Kamiokande collaboration announced in 1998 the disappearance of atmospheric ν_μ, evidence for neutrino oscillations [10], later confirmed by the K2K long-baseline experiment around 2004 [11]. That same year, KamLAND observed long-baseline reactor antineutrino disappearance [12], cementing the oscillation framework and establishing that neutrinos are massive and can change flavor.

1.1 Neutrinos in the Standard Model

The Standard Model (SM) is a gauge theory which describes the electromagnetic weak and strong interactions in the framework of the quantum field theory and is based on the local symmetry group $SU(3)_C \times SU(2)_L \times U(1)_Y$ where C denotes color, L stands for left-handed chirality and Y for weak hypercharge. Within the Standard Model the neutrino particles are described as electrically neutral, colorless fermions which interact only via weak and gravitational interactions. In the minimal SM, the three known neutrino flavors are represented by the left-handed Weyl spinors $\nu_{\ell L}$ ($\ell = e, \mu, \tau$) paired with its charged-lepton partner in an $SU(2)_L$ doublet

$$L_\ell = \begin{pmatrix} \nu_{\ell L} \\ \ell_L^- \end{pmatrix}, \quad Y(L_\ell) = -\frac{1}{2} \tag{1.1}$$

Where Y is the weak hypercharge. Beyond the minimal terms $\mathcal{L}_{min}$ (kinetic and gauge interactions) the most general $SU(3)_C \times SU(2)_L \times U(1)_Y$ gauge-invariant renormalizable Lagrangian can be written with the SM fields (the Higgs doublet H and the observed fermions: the doublet L, $Q = \binom{u_L}{d_L}$ and the singlets l_R, u_R, d_R) can only contain the following Yukawa and Higgs-potential terms:

$$\mathcal{L}_{SM} = \mathcal{L}_{min} + (\lambda_l^{ij} l_R^i L^j H^* + \lambda_d^{ij} d_R^i Q^j H^* + \lambda_u^{ij} u_R^i Q^j H^* + h.c.) + m^2|H|^2 - \frac{\lambda}{4}|H|^4 \tag{1.2}$$

with i, j flavour indices. The Higgs vev[1] and quarks mass terms:

$$m_R l_R l_L + m_d d_R d_L + m_U u_R u_D \tag{1.3}$$

but with no experimental evidence of right-handed neutrino [6] these leptons cannot be coupled with the Higgs field and no Dirac mass term can appear in the Lagrangian. Hence in the SM νs are present as massless fermions, fully described by the kinetic Lagrangian term plus the gauge interactions with the massive vector bosons Z (for neutral interactions NC) and $W^\pm$ (for charged interactions CC)

$$\mathcal{L}_{CC} = -\frac{g}{\sqrt{2}} \sum_{\alpha=e,\mu,\tau} (\bar{\nu}_{\alpha L} \gamma^\mu \alpha_L^- W_\mu^+ + \bar{\alpha} \gamma^\mu \nu_{\alpha L} W_\mu^-); \quad \text{(Charged Current)} \tag{1.4}$$

$$\mathcal{L}_{NC} = -\frac{g}{2cos\theta_W} \sum_{\alpha=e,\mu,\tau} \bar{\nu}_{\alpha L} \gamma^\mu \nu_{\alpha L} Z_\mu; \quad \text{(Neutral Current)} \tag{1.5}$$

[1] The vacuum expectation value of the neutral component of the Higgs doublet. In unitary gauge, $\langle H \rangle = \left(0,\ v/\sqrt{2}\right)^T$ with $v \simeq 246$ GeV.

1.2 Neutrinos beyond the Standard Model

Even if the SM has demonstrated huge successes in providing experimental predictions, it leaves some phenomena unexplained. As it will described in depth in section 1.3, the experimental evidence of neutrino oscillation is proof of the fact that neutrinos do have mass and to explain the existence of this phenomena a theory beyond the Standard Model (BSM) is required. To introduce a neutrino mass term there are different possibilities:

- Assuming the neutrino to be a Dirac particle and introducing the neutrino right-handed component in the electroweak theory thus adding a mass term in the Lagrangian generated with the Higgs mechanism that conserves the lepton number;

$$\mathcal{L}_{m_\nu} = \sum_{\alpha=e,\mu,\tau} -m^D_{\nu_\alpha}[\bar{\nu}_{\alpha L}\nu_{\alpha R} + \bar{\nu}_{\alpha R}\nu_{\alpha L}] \tag{1.6}$$

  These right handed fields are called *sterile* since they do not enter into the standard charged and neutral currents but only in gravitational interactions. The left handed fields are instead called *active*. To account the experimental evidences the Yukawa couplings should be $\lesssim 10^{-11}$ [13]

- Rewrite the Dirac equation in terms of left-handed fields only, using the charge-conjugation matrix $\mathcal{C}$, in which the fields can be written as a superposition of the two components:

$$\nu = \nu_L + \nu_R = \nu_L + \nu^C_L \tag{1.7}$$

  From Eq.1.1 follows that a particle described as such, a $Majorana$ particle, is its own anti-particle:

$$\nu^C = (\nu_L + \nu^C_L)^C = \nu^C_L + \nu_L = \nu \tag{1.8}$$

  and the mass term can be written using only the left-handed component of the field:

$$-\frac{1}{2}m\bar{\nu}^C_L\nu_L \tag{1.9}$$

  Eq. 1.2 is not invariant under $SU(2)\times U(1)$ transformations and it violates the lepton number conservation.

Up to date, there is no experimental evidence whether neutrinos are Dirac or Majorana particles. This remains one of the open questions (see section 1.5) in the neutrino physics.

1.3 The Neutrino oscillation phenomenon

Following the analogy with kaon-antikaon oscillations, the idea of to attribute the same phenomenon in the neutrino system was first discussed by Pontecorvo in 1957, later the transformation of a neutrino of a certain flavor into a neutrino of a different flavor was hypothesized with the implication that such phenomenon would mean that neutrinos must have non-zero masses and non-zero mass difference between flavours. Moreover the oscillations imply that neutrinos weak interactions and mass eigenstates do not coincide, thus it is natural to introduce in the charge current Lagrangian in the SM 2 unitary 3×3 matrices V_l and V_ν such that:

$$\mathcal{L}_{CC}^{leptons} = \frac{g}{\sqrt{2}} \left[\begin{pmatrix} \bar{e}_L & \bar{\mu}_L & \bar{\tau}_L \end{pmatrix} U_{PMNS} \gamma^\mu \begin{pmatrix} \nu_{1L} \\ \nu_{2L} \\ \nu_{3L} \end{pmatrix} W_\mu^+ + h.c. \right] \tag{1.10}$$

Where $U_{PMNS} = V_l^\dagger V_\nu$ is the so called Pontecorvo-Maki-Nakagawa-Sakata mixing matrix.
Using this matrix the left-handed flavor neutrino fields are defined as:

$$\nu_L = \begin{pmatrix} \nu_{eL} \\ \nu_{\mu L} \\ \nu_{\tau L} \end{pmatrix} = U_{PMNS} \begin{pmatrix} \nu_{1L} \\ \nu_{2L} \\ \nu_{3L} \end{pmatrix} = U_{PMNS} n_L \tag{1.11}$$

with $\nu_{1,2,3L}$ the mass eigenstates. The PMNS mixing matrix is parametrized by three mixing angles θ_{12},θ_{23}, θ_{13} and by one or three CP violating phases, depending on wheter the massive neutrinos are Majorana or Dirac particles:

$$\begin{aligned} U_{PMNS} &= \begin{pmatrix} U_{e1} & U_{e2} & U_{e3} \\ U_{\mu 1} & U_{\mu 2} & U_{\mu 3} \\ U_{\tau 1} & U_{\tau 2} & U_{\tau 3} \end{pmatrix} \\ &= \begin{pmatrix} 1 & 0 & 0 \\ 0 & c_{23} & s_{23} \\ 0 & -s_{23} & c_{23} \end{pmatrix} \begin{pmatrix} c_{13} & 0 & s_{13} e^{i\delta_{CP}} \\ 0 & 1 & 0 \\ -s_{13} e^{i\delta_{CP}} & 0 & c_{13} \end{pmatrix} \begin{pmatrix} c_{12} & s_{12} & 0 \\ -s_{12} & c_{12} & 0 \\ 0 & 0 & 1 \end{pmatrix} P \end{aligned} \tag{1.12}$$

Where $P = diag(1, e^{\lambda_2}, e^{\lambda_3})$, $c_{i,j} = cos\theta_{i,j}$ and $s_{i,j} = sin\theta_{i,j}$.
$\delta_{CP} \in [0, 2\pi]$ is the Dirac phase while $\lambda_{1,2}$ are called Majorana phases, and are both equal to 1 for Dirac particles.

1.3.1 Oscillation in vacuum

The mass eigenstates $|\nu_i\rangle$ are the eigenstates of the Hamiltonian

$$\mathcal{H}_{vacuum} |\nu_i\rangle = E_i |\nu_i\rangle \tag{1.13}$$

with $E_i = \sqrt{\vec{p}^2 + m_i^2}$; hence, they are described by plane waves

$$|\nu_i(t)\rangle = e^{-iE_i t} |\nu_i\rangle \tag{1.14}$$

If the mass eigenstates evolve in time with different frequencies, due to mass difference, the superposition changes in time and a pure flavor $|\nu_\alpha\rangle$ at time $t = 0$ becomes a flavor mixture at $t > 0$.
The flavor state at time t after a distance L travelled in vacuum is described by

$$|\nu_\alpha(t)\rangle = \sum_i U_{\alpha i} e^{-iE_i t} |\nu_i\rangle \tag{1.15}$$

and applying the unitarity property of the mixing matrix the mass eigenstates can be written in terms of flavor eigenstates

$$|\nu_i\rangle = \sum_\alpha U_{\alpha i} |\nu_\alpha\rangle \tag{1.16}$$

and replacing Eq. 1.16 in Eq. 1.15

$$|\nu_\alpha(t)\rangle = \sum_{\beta=e,\mu,\tau} \left(\sum_i U^*_{\alpha i} e^{-iE_i t} U_{\beta i} \right) |\nu_\beta\rangle \tag{1.17}$$

The oscillation amplitude of this neutrino produced at $t = 0$ with flavor α which undergoes to a CC interaction at time $t > 0$ producing a charged lepton of flavor β is:

$$A_{\nu_\alpha \to \nu_\beta}(t) = \langle \nu_\beta | \nu_\alpha(t) \rangle = \sum_i U^*_{\alpha i} U_{\beta i} e^{iE_i t} \tag{1.18}$$

And the oscillation probability is:

$$P_{\nu_\alpha \to \nu_\beta}(t) = |A_{\nu_\alpha \to \nu_\beta}(t)|^2 = \sum_{i,j} U^*_{\alpha i} U_{\beta i} U_{\alpha j} U^*_{\beta j} e^{-i(E_i - E_j)t} \tag{1.19}$$

For ultrarelativistic neutrinos the energy eigenvalues 1.13 can be approximated

by

$$E_i \simeq E + \frac{m_i^2}{2E} \tag{1.20}$$

thus the oscillation probability depends on the squared neutrino mass difference

$$E_i - E_j \simeq \frac{\Delta m_{ij}^2}{2E} \tag{1.21}$$

in which $\Delta m_{ij}^2 = m_i^2 - m_j^2$ and $E = |\vec{p}|$.
The oscillation probability can be written in terms of the mass difference an the source-detector distance L being $t = L/c$ in natural units:

$$P_{\nu_\alpha \to \nu_\beta}(L, E) = \sum_{i,j} U_{\alpha i}^* U_{\beta i} U_{\alpha j} U_{\beta j}^* e^{-i\frac{\Delta m_{ij}^2 L}{2E}} \tag{1.22}$$

Similarly to the case of neutrinos, it can be obtained the antineutrino oscillation probability

$$P_{\bar{\nu}_\alpha \to \bar{\nu}_\beta}(L, E) = \sum_{i,j} U_{\alpha i} U_{\beta i}^* U_{\alpha j}^* U_{\beta j} e^{-i\frac{\Delta m_{ij}^2 L}{2E}} \tag{1.23}$$

Considering a simplified case with just two neutrino flavors the oscillation probability depends only on one mixing angle and the intial ν_α, from a monocromatic source, evolves as a mixture of the mass states, and after a distance x it becomes

$$|\nu(x)\rangle = e^{ip_1 x} cos\theta \, |\nu\rangle_1 + e^{ip_2 x} sin\theta \, |\nu\rangle_2 \tag{1.24}$$

The probabiliy of detecting a new neutrino flavor at $x = L$ will become

$$P_{\bar{\nu}_\alpha \to \bar{\nu}_\beta}(L, E) \sim sin^2 2\theta sin^2 \frac{\Delta m_{12}^2 L}{4E} \tag{1.25}$$

One can then define the oscillation length as the value of the baseline L for which the transition probability is maximal, i.e. equal to $sin^2 2\theta$, as:

$$L^{osc}[km] = 2.47 \frac{E[GeV]}{\Delta m^2 [eV^2]} \tag{1.26}$$

In Fig. 1.1 the solid line represent Eq.1.25 as a function of the argument of the sine function, but in real experiments the neutrino source is not monochromatic and the detector has finite spatial and energy resolution, therefore it is impossible to measure the oscillation probability for precise values of L/E. To account for this it is always necessary to average Eq.1.25 over an appropriate distribution of L/E, for example in fig. 1.1 the dashed line represent the oscillation probability

folded with a gaussian distribution $\phi(L/E)$ with average $<L/E>$ and standard deviation $\sigma_{L/E}$.

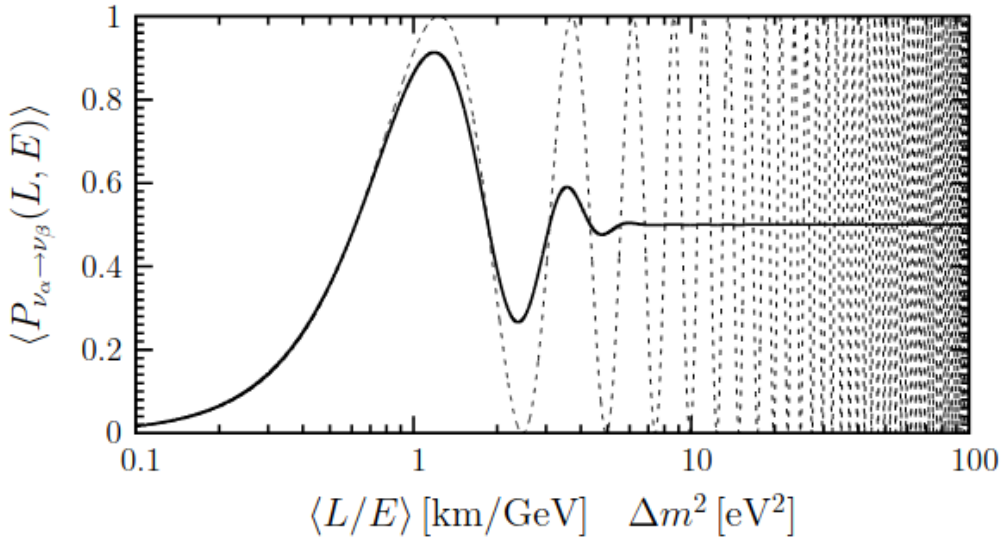

Figure 1.1: Probability of $\nu_\alpha \to \nu_\beta$ for $sin^2 2\theta = 1$ as a function of $<L/E>$ and Δm^2. Solid line: transition probability in Eq. 1.25. Dashed line: averaged transition probability over a Gaussian distribution of L/E that simulates the effect of the experiment's finite spatial and energy resolutions [13]

Experiments are designed choosing the appropriate value of L/E to be sensitive to the given value of Δm^2, that as shown in fig. 1.1 is:

$$\frac{L}{E} \approx \frac{2}{\Delta m^2} \tag{1.27}$$

Using this value one can classify the oscillation experiments as follows:

- **Short Baseline (SBL)**: Experiments with sensitivity range:

$$\frac{L}{E} \approx [0.1, 10^2] eV^2 \tag{1.28}$$

- **Long Baseline (LBL)**: Experiments with sensitivity:

$$\frac{L}{E} \approx [10^{-4}, 10^{-3}] eV^2 \tag{1.29}$$

- **Very Long Baseline (VLB)**: Experiments with sensitivity:

$$\frac{L}{E} \approx [10^{-12}, 10^{-5}]eV^2 \tag{1.30}$$

In the simplified case of only two flavors there is no CP violation, this however changes when taking into account all the lepton flavors.
The transformation channels in Eq. 1.22 and Eq. 1.23 are related by a CP transformation, which correspond to the interchange between particles and antiparticle with also opposite helicity. If CP simmetry is to be conserved, Eq. 1.22 and Eq. 1.23 must be equal. The probability 1.22 can be rewritten in terms of its real and immaginary parts of the quadratic products [13]

$$\begin{aligned} P_{\nu_\alpha \to \nu_\beta}(L,E) = \delta_{\alpha\beta} - 4\sum_{i>j} \Re[U^*_{\alpha i}U_{\beta i}U_{\alpha j}U^*_{\beta j}] sin^2\left(\frac{\Delta m^2_{ij}L}{4E}\right) \\ +2\sum_{i>j} \Im[U^*_{\alpha i}U_{\beta i}U_{\alpha j}U^*_{\beta j}] sin\left(\frac{\Delta m^2_{ij}L}{2E}\right) \end{aligned} \tag{1.31}$$

in which the real part is CP conserving while the imaginary term violates the CP invariance and it is the only term that contributes to CP asymmetry. In terms of the Jarlskog invariant the CP violation can be defined as

$$J_{\alpha\beta} = \Im[U_{\mu 3}U_{e2}U^*_{\mu 2}U^*_{e3}] = \frac{1}{8} sin(2\theta_{12}) sin(2\theta_{23}) cos(\theta_{13}) sin(\delta_{CP}) \tag{1.32}$$

For $\alpha \neq \beta$ the oscillation probability is said *transition probability*, while for $\alpha = \beta$ it is called the *survival probability* in which case Eq. 1.31 has no immaginary part.
While J value quantifies the level of CP violation, the asymmetry parameter is defined as:

$$A_{\alpha\beta} \equiv \frac{P(\nu_\alpha \to \nu_\beta) - P(\bar{\nu}_\alpha \to \bar{\nu}_\beta)}{P(\nu_\alpha \to \nu_\beta) + P(\bar{\nu}_\alpha \to \bar{\nu}_\beta)} = 4J \sum_{k>j} s_{\alpha\beta;kj} sin\left(\frac{\Delta m^2_{ij}L}{2E}\right) \tag{1.33}$$

where $s_{\alpha\beta;kj} = \pm 1$ when (α, β, γ) is an even and odd permutation of (e, μ, τ) respectively. Moreover it is possible to show [13] that:

$$A^{CP}_{e\mu} = A^{CP}_{\mu\tau} = A^{CP}_{\tau e} = -A^{CP}_{\mu e} = -A^{CP}_{\tau\mu} = -A^{CP}_{e\tau} \tag{1.34}$$

i.e. that CP violation does not depend on the oscillation channel.

1.3.2 Oscillation in matter

In the case neutrinos propagate through matter, the oscillation probability is further modified with respect to the propagation in vacuum, because ν's are affected by coherent elastic scattering with particles in the medium and in particular ν_e have different interaction channels with matter with respect to ν_μ and ν_τ . Also incoherent inelastic scatterings can occur but the probability of incoherent scatterings is small and it can be safely neglected [13].
In dense medium with electron, protons and neutrons all three neutrino flavors are affected by coherent forward elastic weak NC interactions that can occur with any fermion in the medium. The contribution of the NC scattering can be introduced in the total neutrino Hamiltonian. For any flavor neutrino ν_α, the NC potential is given by:

$$V_{NC} = \frac{\sqrt{2}}{2} G_F[-n_e(1 - 4sin^2\theta_W) + n_p(1 - 4sin^2\theta_W) - n_n] \tag{1.35}$$

in which G_F is the Fermi constant and n_e, n_p and n_n are the electron, proton and neutron number density respectively and θ_W is the Winberg angle. Assuming that in a neutral medium the electron and proton contributions cancel out the NC potential simplifies to:

$$V_{NC} = \frac{\sqrt{2}}{2} G_F n_n \tag{1.36}$$

Since this contribution is equivalent to all neutrino flavors, it generats an overall phase shift which is irrelevant for the neutrino mixing.
However ν_e can also be affected by coherent weak CC interactions with electrons in the medium. Hence the total Hamiltonian has an extra potential term that accounts for the $\nu_e - e$ elastic scattering:

$$V_{CC} = \sqrt{2} G_F n_e \tag{1.37}$$

This term in the Hamiltonian affects only electronic neutrinos, since neither μ nor τ particles are present in matter, thus introducing a phase shift that is relevant for flavor transition. The neutrino mass states are eigenstates of the vacumm Hamiltonian as per Eq. 1.13, the total Hamiltonian in matter is given by:

$$\mathcal{H} = \mathcal{H}_{vacuum} + \mathcal{H}_{MSW} \tag{1.38}$$

in which the matter Hamiltonian $\mathcal{H}_{MSW}$ that acts on flavor states is

$$\mathcal{H}_{MSW} = \pm 2 G_F n_e(\vec{x}) \begin{pmatrix} 1 & 0 & 0 \\ 0 & 0 & 0 \\ 0 & 0 & 0 \end{pmatrix} \quad \begin{cases} + \text{ for } \nu \\ - \text{ for } \bar{\nu} \end{cases} \tag{1.39}$$

in which $\vec{x}$ is the neutrino position.
The solution of the Schrödinger equation with the potential described in Eq.1.39 gives the matter eigenstates $\nu^m_{1,2,3}$ and the modified oscillation probabilities for all neutrino flavors can be derived. For the purpose of this thesis it is relevant to describe the probability of $\nu_\mu \to \nu_e$ with matter effect included [14]:

$$\begin{aligned} P(\nu_\mu \to \nu_e) \simeq\ & \sin^2\theta_{23}\,\frac{\sin^2 2\theta_{13}}{(A-1)^2}\,\sin^2[(A-1)\,\Delta_{31}] \\ & + \alpha^2 \cos^2\theta_{23}\,\frac{\sin^2 2\theta_{12}}{A^2}\,\sin^2(A\,\Delta_{31}) \\ & + \alpha\,\frac{\cos\theta_{13}\,\sin 2\theta_{12}\,\sin 2\theta_{13}\,\sin 2\theta_{23}\,\cos\delta_{\mathrm{CP}}}{A\,(1-A)}\cos\Delta_{31}\,\sin(A\,\Delta_{31})\,\sin[(1-A)\,\Delta_{31}] \\ & - \alpha\,\frac{\cos\theta_{13}\,\sin 2\theta_{12}\,\sin 2\theta_{13}\,\sin 2\theta_{23}\,\sin\delta_{\mathrm{CP}}}{A\,(1-A)}\sin\Delta_{31}\,\sin(A\,\Delta_{31})\,\sin[(1-A)\,\Delta_{31}] \end{aligned} \tag{1.40}$$

in which

$$\alpha \equiv \frac{\Delta m^2_{21}}{\Delta m^2_{31}} \tag{1.41}$$

$$\Delta_{31} \equiv \frac{\Delta m^2_{31}\,L}{4E} \tag{1.42}$$

$$A \equiv \frac{2VE}{\Delta m^2_{31}} = \frac{2\sqrt{2}\,G_F\,n_e\,E}{\Delta m^2_{31}} \tag{1.43}$$

The first term in Eq.1.40 describes oscillations driven by Δm^2_{31} in the so-called *1–3 sector*. The second term corresponds to oscillations in the *1–2 (solar) sector*, driven by Δm^2_{21}, but its contribution is suppressed by the factor α^2. The third term is a CP-conserving interference term (proportional to $\cos\delta_{\mathrm{CP}}$). The fourth term is proportional to the Jarlskog invariant J and encodes CP-violating effects. For $\delta_{\mathrm{CP}} = \pm\pi/2$ (maximal violation), this term can modify the oscillation probability by up to $\pm 30\%$. All terms account for matter effects through the parameter A, which depends on Δm^2_{31}. In matter, these effects can either enhance or suppress the oscillation probabilities $P(\nu_\mu \to \nu_e)$ and $P(\bar{\nu}_\mu \to \bar{\nu}_e)$, depending on the true neutrino mass ordering.

1.4 Neutrino experiments and previous results

The current understanding of the parameters in the three–neutrino framework has emerged from a wide variety of experiments. These are typically categorized ac-

cording to the oscillation parameters to which they are most sensitive, determined primarily by the characteristic L/E of each setup:

- Solar neutrino experiments, sensitive to $\sin^2\theta_{12}$ and Δm^2_{21};
- Reactor neutrino experiments, sensitive to θ_{13};
- Atmospheric neutrino experiments, sensitive to $\sin^2\theta_{23}$ and Δm^2_{32};
- Long-baseline accelerator experiments, sensitive to $\sin^2\theta_{23}$, Δm^2_{31}, and θ_{13}.

Solar neutrino evidence

The first clear evidence for neutrino flavor transformation came from solar neutrino experiments. Early radiochemical experiments - such as Homestake (which used chlorine instead of gallium) [15], GALLEX [16], GNO [17], and SAGE [18] - measured the capture of solar electron neutrinos via

$$\nu_e + {}^{71}\mathrm{Ga} \rightarrow {}^{71}\mathrm{Ge} + e^-,$$

with thresholds down to $E_\nu \gtrsim 233$ keV. All consistently reported an $\sim 50\%$ deficit in the observed ν_e flux relative to the predictions of the Standard Solar Model (SSM) [19], establishing the so-called "solar neutrino problem."

Water Cherenkov detectors, first Kamiokande [20] and later Super–Kamiokande [21], measured neutrino–electron elastic scattering,

$$\nu_x + e^- \rightarrow \nu_x + e^-,$$

with an energy threshold of ~ 7 MeV. They confirmed the solar neutrino deficit with more than 6σ significance, but could not distinguish whether the discrepancy originated from an inaccurate solar model or from neutrino oscillations.

The decisive breakthrough was provided by the Sudbury Neutrino Observatory (SNO) [22], a heavy-water Cherenkov detector operating in Canada from 1999 to 2006. Thanks to 1 kt of D_2O, SNO was uniquely sensitive to three distinct interaction channels:

1. Elastic scattering (ES): $\nu_x + e^- \rightarrow \nu_x + e^-$;
2. Charged current (CC): $\nu_e + d \rightarrow p + p + e^-$;
3. Neutral current (NC): $\nu_x + d \rightarrow p + n + \nu_x$.

The free neutron produced in the NC interaction was detected via capture on salt, emitting 8 MeV γ rays observed as Cherenkov light. Since the cross sections of all

three channels are well known, SNO could separately measure the ν_e flux (from CC) and the total flux of all active neutrinos (from NC).

SNO reported the total flux of ^{8}B solar neutrinos as

$$\phi(\nu_e + \nu_\mu + \nu_\tau)_{\mathrm{SNO}} = (4.94 \pm 0.21_{\mathrm{stat}} \pm 0.36_{\mathrm{syst}}) \times 10^6 \ \mathrm{cm}^{-2}\,\mathrm{s}^{-1}, \tag{1.44}$$

in excellent agreement with the Standard Solar Model prediction [19]

$$\phi_\nu^{\mathrm{tot}}(\mathrm{SSM}) = \left(5.49^{+0.95}_{-0.89}\right) \times 10^6 \ \mathrm{cm}^{-2}\,\mathrm{s}^{-1}. \tag{1.45}$$

This result established, beyond doubt, that the observed solar ν_e deficit is due to flavor oscillations.
Moreover, the SNO experiment provided a direct measurement of the integrated ν_e flux relative to the total active neutrino flux, reporting

$$R \equiv \frac{\phi(\nu_e)}{\phi(\nu_e + \nu_\mu + \nu_\tau)} = 0.340 \pm 0.023_{\mathrm{stat}} \pm 0.030_{\mathrm{syst}}, \tag{1.31}$$

which clearly demonstrates the existence of a non-vanishing flux of $\nu_\mu + \nu_\tau$. The total flux was found consistent with the Standard Solar Model (SSM), and the observed suppression of ν_e was naturally explained in terms of flavor oscillations during propagation from the solar core to the Earth.

The Borexino experiment [23], a 278-ton liquid scintillator detector operating at the Gran Sasso Laboratory (Italy) since 2007, has provided precision measurements of low-energy solar neutrinos. In particular, Borexino measured both the ^{7}Be electron neutrino flux and the pep neutrino flux [2]:

$$\phi(^7\mathrm{Be}) = (3.10 \pm 0.15) \times 10^9 \ \mathrm{cm}^{-2}\,\mathrm{s}^{-1}, \tag{1.32}$$

$$\phi(\mathrm{pep}) = (1.6 \pm 0.3) \times 10^8 \ \mathrm{cm}^{-2}\,\mathrm{s}^{-1}, \tag{1.33}$$

corresponding to roughly 62% of the SSM prediction.

These findings were independently confirmed by the KamLAND experiment in Japan [24]. KamLAND is a long-baseline reactor antineutrino experiment located in the Kamioka mine (also hosting Super-Kamiokande). With its 1 kt liquid scintillator detector, KamLAND is exposed to $\bar{\nu}_e$ produced by more than 50 nuclear reactors in Japan, corresponding to a total thermal power exceeding 60 GW and an average baseline of ~ 180 km. The experiment observed $\bar{\nu}_e$ disappearance and a distortion of the positron energy spectrum, consistent with oscillations.

[2] "pep" denotes the p–e^-–p reaction $p + e^- + p \to d + \nu_e$ in the solar pp chain; it produces monoenergetic electron neutrinos with $E_\nu \simeq 1.44$ MeV.

Within the two-flavor oscillation framework, with $\theta = \theta_{12}$ and $\Delta m^2 = \Delta m^2_{21}$, KamLAND reported:

$$\Delta m^2_{21} = (7.53 \pm 0.18) \times 10^{-5}\ \text{eV}^2, \tag{1.34}$$

$$\tan^2\theta_{12} = 0.44 \pm 0.03. \tag{1.35}$$

These results were in excellent agreement with solar neutrino measurements, providing a coherent picture of flavor transformation driven by the Δm^2_{21} mass splitting.

Atmospheric neutrino evidence

Cosmic rays, composed primarily of energetic protons and heavy nuclei, interact in the upper atmosphere producing mesons (mostly pions and kaons). Their subsequent weak decays generate neutrinos, with an expected flux ratio of $\nu_e : \nu_\mu \simeq 1 : 2$ at production. Atmospheric neutrinos typically have energies in the GeV range and are created at altitudes of tens of kilometers above the Earth's surface. Depending on the zenith angle, they may travel distances from $L \sim 10$ km (downgoing) to $L \sim 10^4$ km (up-going, traversing the Earth) before reaching underground detectors. This wide L/E range makes them an excellent probe of oscillations driven by Δm^2_{32} and θ_{23}.

The first indication of an anomaly was reported by the Kamiokande experiment, which measured a deficit in the ν_μ flux compared to expectations [25], consistent with earlier observations by the IMB experiment [26]. The definitive discovery came from the Super–Kamiokande experiment in 1998 [21], which measured the zenith-angle distribution of ν_μ and ν_e events. A strong disappearance of upward-going ν_μ was observed, while the ν_e flux remained consistent with predictions. These results were confirmed by the MACRO [27] and Soudan-2 [28] experiments.

The survival probability in the two-flavor approximation is given by

$$P(\nu_\mu \to \nu_\mu) = 1 - \sin^2(2\theta_{23}) \sin^2\left(\frac{\Delta m^2_{32} L}{4E}\right), \tag{1.36}$$

and Super–Kamiokande data were consistent with nearly maximal mixing $\sin^2 2\theta_{23} \simeq 1$ and $\Delta m^2_{32} \sim 2.5 \times 10^{-3}\,\text{eV}^2$.

More recently, high-energy atmospheric neutrinos have been studied by ANTARES [29] and IceCube [30], which detect Cherenkov light from muons produced in charged-current ν_μ interactions. These experiments extend the L/E reach to much higher energies (5–50 GeV) and provide measurements of oscillation parameters consis-

tent with those from accelerator and reactor experiments:

$$\Delta m^2_{32} = (2.31^{+0.11}_{-0.13}) \times 10^{-3}\,\mathrm{eV}^2, \qquad \sin^2\theta_{23} = 0.51^{+0.07}_{-0.09},$$

assuming normal mass ordering (see section 1.5.1).

Long-baseline accelerator neutrino evidence

The first accelerator-based long-baseline experiments confirmed the atmospheric oscillation results in a controlled setting, by sending an artificial ν_μ beam over hundreds of kilometers. The pioneering KEK-to-Kamioka (K2K) experiment (1999–2004) [31] sent a beam with a mean energy of 1.3 GeV from KEK to the Super–Kamiokande detector, 250 km away. K2K observed a clear deficit of ν_μ events, as well as a distortion of the energy spectrum, consistent with oscillations driven by $\Delta m^2_{32} \sim 2.8 \times 10^{-3}\,\mathrm{eV}^2$ and nearly maximal mixing.

The Main Injector Neutrino Oscillation Search (MINOS) at Fermilab further improved the precision of the oscillation parameter measurements [32]. Using the NuMI beam and a 5.4 kt magnetized iron calorimeter located in the Soudan mine at a distance of 735 km, MINOS compared near and far detectors, establishing ν_μ disappearance with high significance and providing early indications of ν_e appearance. These results confirmed the Super–Kamiokande atmospheric anomaly with controlled beam conditions.

The current generation of long-baseline experiments, T2K in Japan and NOνA in the United States, have played a central role in pinning down the atmospheric oscillation parameters. T2K sends a narrow-band beam from J-PARC to Super–Kamiokande (295 km baseline), optimised around the first oscillation maximum [33]. It has observed both $\nu_\mu \to \nu_e$ and $\bar{\nu}_\mu \to \bar{\nu}_e$ appearance, providing the first hints of a nonzero CP-violating phase δ_{CP}. NOνA, operating with a longer baseline of 810 km and a highly segmented liquid scintillator detector at Ash River, has complementary sensitivity due to its higher neutrino energies [34]. Both experiments have measured Δm^2_{32} and θ_{23} with increasing precision and explored the neutrino mass ordering.

Although each experiment individually reports a mild preference for the normal mass ordering, recent combined analyses show some tension between their best-fit regions [35]. The T2K best-fit point lies in a region disfavored by NOνA, though areas of overlap remain. These results highlight the importance of joint fits and global analyses to resolve degeneracies and provide a consistent determination of the neutrino oscillation parameters.

Short-baseline neutrino experiments

Short-baseline (SBL) oscillation experiments can be divided into two main classes. At baselines of order $L \sim 1$–2 km and neutrino energies of a few MeV, reactor-based measurements probe the θ_{13} mixing angle and Δm^2_{31} by studying the disappearance of electron antineutrinos via inverse beta decay (IBD) in gadolinium-doped liquid scintillator detectors. The most precise determination of θ_{13} was obtained by the Daya Bay experiment, which reported $\sin^2 2\theta_{13} = 0.0851 \pm 0.0024$ [36]. Complementary measurements were provided by Double Chooz [37] and RENO [38], albeit with larger uncertainties. Together, these results established a non-zero value of θ_{13} with high precision, a crucial input for CP-violation searches in the lepton sector.

At much shorter baselines ($L \lesssim 100$ m) and higher values of L/E, a series of anomalies have emerged that are not easily explained within the three-flavor framework. The LSND experiment at Los Alamos [39] reported evidence for $\bar{\nu}_\mu \to \bar{\nu}_e$ appearance, a result later supported by MiniBooNE [40], which observed an excess of electron-like events in both neutrino and antineutrino modes. Reactor experiments at very short distances also found a persistent deficit of $\bar{\nu}_e$ events relative to updated flux predictions, the so-called "reactor antineutrino anomaly" [41]. Finally, calibration measurements of solar neutrino detectors with intense radioactive sources (GALLEX and SAGE) revealed the "gallium anomaly" [42]. These observations have been widely interpreted as hints for oscillations involving one or more light sterile neutrinos at the eV scale, though no definitive confirmation has been achieved.

1.5 Open Questions of neutrino physics

The pioneering stage of neutrino physics, which established the existence of non-zero neutrino masses and flavor oscillations, is essentially complete. Today, the field has entered an era of precision measurements, where the focus is on resolving the fundamental unknowns that remain beyond the minimal three-flavor oscillation paradigm. Despite remarkable experimental progress, several questions remain unanswered:

- What is the absolute scale of neutrino masses?
- What is the correct ordering of the neutrino mass states (normal or inverted)?
- Are neutrinos Dirac or Majorana fermions?
- Is the atmospheric mixing angle θ_{23} exactly maximal, or does it lie in the

lower or upper octant?

- Is CP symmetry violated in the lepton sector, and what is the value of the CP-violating phase δ_{CP}?
- What is the underlying origin of neutrino masses and flavor mixing?
- Is the number of massive neutrino states equal to three, or are additional sterile states involved?

Next-generation neutrino experiments with artificial sources and advanced detectors are specifically designed to address these open issues. In the following, we discuss in more detail three of the most pressing open questions: the mass ordering, the θ_{23} octant, and the leptonic CP-violating phase.

1.5.1 Mass ordering

In the minimal three-flavor oscillation framework, oscillations are governed by two independent squared-mass splittings: Δm^2_{21} and Δm^2_{31}. Solar neutrino experiments, combined with reactor measurements, have precisely determined Δm^2_{21} and established its sign as positive due to the matter effects experienced by neutrinos propagating through the Sun. By contrast, the sign of Δm^2_{31} remains unknown because atmospheric and accelerator experiments are only sensitive to its magnitude.

This ambiguity leads to two possible neutrino mass orderings:

- **Normal ordering (NO):** $m_1 < m_2 < m_3$, with $\Delta m^2_{31} > 0$ and $\Delta m^2_{21} > 0$;
- **Inverted ordering (IO):** $m_3 < m_1 < m_2$, with $\Delta m^2_{31} < 0$ and $\Delta m^2_{21} > 0$.

A schematic representation of both orderings is presented in Fig. 1.2.
It is possible to define a lower bound on the sum of the neutrino masses, depending on the ordering. For normal ordering one finds

$$\sum m_\nu \gtrsim \sqrt{\Delta m^2_{21}} + \sqrt{|\Delta m^2_{31}|} \simeq 0.06 \text{ eV}, \tag{1.46}$$

while for inverted ordering

$$\sum m_\nu \gtrsim 2\sqrt{|\Delta m^2_{31}|} + \frac{\Delta m^2_{21}}{2\sqrt{|\Delta m^2_{31}|}} \simeq 0.10 \text{ eV}. \tag{1.47}$$

The distinction between the two orderings is of paramount importance. It affects the interpretation of neutrinoless double-beta decay searches, the extraction of cosmological neutrino mass constraints, and models of neutrino mass generation.

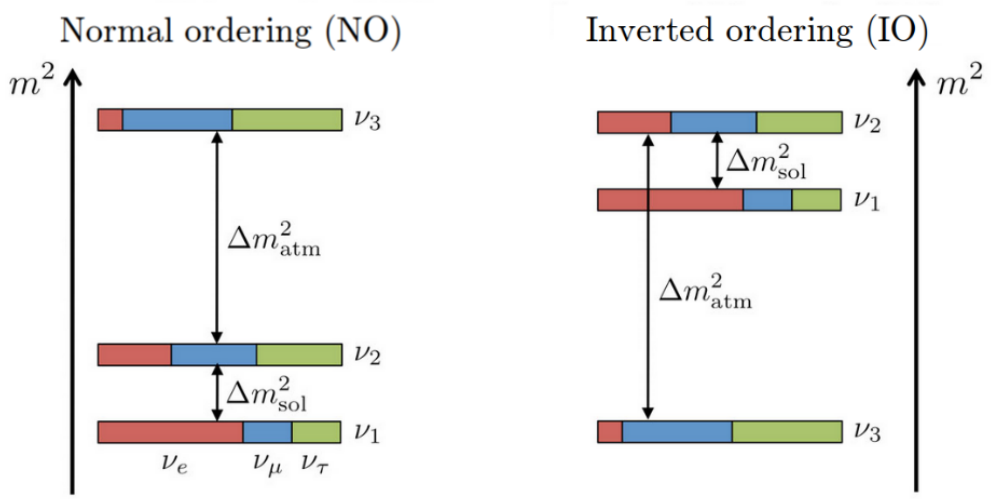

Figure 1.2: Schemes of the two possible mass orderings: the normal ordering (right) and the inverted ordering (left)

Current global fits, combining long-baseline accelerator, reactor, and solar neutrino data, show a preference for the normal ordering, with the inverted ordering disfavored at the ~ 1.5–2σ level [43, 44].

1.5.2 The θ_{23} octant

The atmospheric mixing angle θ_{23} plays a central role in the neutrino mixing matrix. Its current best-fit value is close to $\pi/4$, corresponding to maximal mixing between ν_μ and ν_τ. However, present data cannot yet establish whether $\sin^2\theta_{23}$ lies below or above 0.5, i.e. whether θ_{23} belongs to the lower ($\theta_{23} < \pi/4$) or upper ($\theta_{23} > \pi/4$) octant.

Determining the octant is crucial, since it carries implications for the underlying flavor symmetries and for theoretical models that aim to explain the observed pattern of mixing angles. Current measurements from MINOS, T2K, and NOνA provide constraints on θ_{23}, but the ambiguity between the octants remains. Recent global fits mildly favor non-maximal mixing in the upper octant, but maximal mixing is still compatible within uncertainties [45, 46, 47].

1.5.3 CP violation in the lepton sector

A major open question is whether neutrino oscillations violate CP symmetry. This is parameterized by the phase δ_{CP} in the PMNS mixing matrix. If δ_{CP} takes values different from 0 or π, neutrino and antineutrino oscillation probabilities

differ, signaling CP violation.

Hints of CP violation have emerged from T2K and NOνA data, with a preference for values of δ_{CP} near $3\pi/2$. Positive values of δ_{CP} around $\pi/2$ are disfavored at more than 2σ, although the full 0–2π range remains allowed. The possibility of large CP violation in the lepton sector is especially intriguing, since it could be connected to the matter-antimatter asymmetry of the Universe via leptogenesis. Resolving the value of δ_{CP} with high precision is one of the central goals of next-generation long-baseline experiments such as DUNE and Hyper-Kamiokande [46, 47, 48, 49].

Chapter 2

The DUNE experiment

2.1 Overview

The Deep Underground Neutrino Experiment (DUNE) is a next-generation, international facility designed to address some of the most fundamental open questions in particle physics. Its primary scientific program focuses on long-baseline neutrino oscillations, neutrino astrophysics, and the search for nucleon decay. The experiment is currently under development in the United States and will consist of three major components [48]:

- a high-intensity, wide-band (anti)neutrino source provided by the Long-Baseline Neutrino Facility (LBNF) at Fermilab (Illinois);
- the Near Detector (ND) complex, located 574 m downstream of the neutrino production point;
- the Far Detector (FD), installed 1.5 km underground at the Sanford Underground Research Facility (SURF) in South Dakota. The FD will be composed of four modular Liquid Argon Time Projection Chambers (LArTPCs), for a total active mass of about 70 kt.

The baseline separating the source and the far site is 1285 km, following the neutrino beamline through the Earth. A schematic layout of the experimental infrastructure is shown in Fig.2.1.

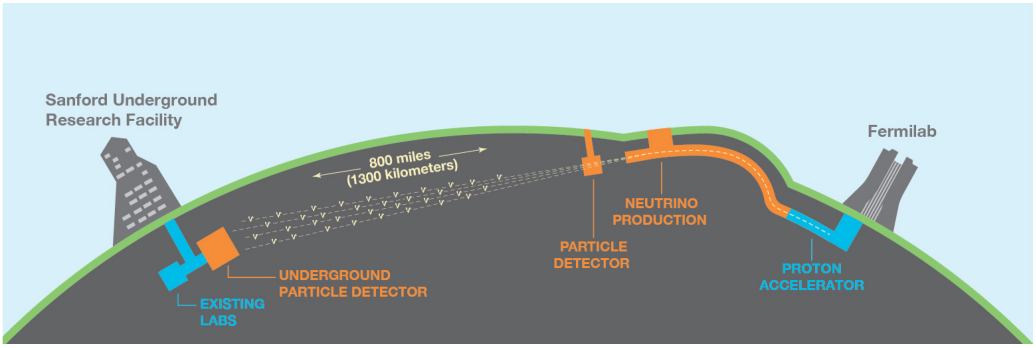

Figure 2.1: Schematic view of DUNE experiment with the LBNF beamline and the ND at Fermilab in Illinois and the FD in South Dakota [50]

The scientific objectives of DUNE are divided into *primary* and *secondary* goals [48, 51, 50]. The primary physics program includes:

- precision measurements of neutrino oscillation parameters, in particular the determination of the neutrino mass ordering and the search for CP violation in the three-flavour framework;
- detection and study of the neutrino burst from a core-collapse supernova within the Milky Way, should such an event occur during the experiment's operational lifetime;
- searches for proton decay in multiple possible channels, thereby testing Grand Unified Theories well beyond current experimental limits.

In addition to these flagship goals, DUNE's unique capabilities open the door to a broad range of secondary physics opportunities, such as:

- searches for physics beyond the Standard Model, including sterile neutrinos, non-standard interactions (NSIs), non-unitarity of the PMNS matrix, and possible violations of Lorentz and CPT symmetries;
- studies of oscillation phenomena using atmospheric and solar neutrinos;
- searches for light dark matter through neutral-current–like interactions in the ND, as well as boosted dark matter signals in the FD;
- a comprehensive neutrino–nucleus interaction program, with precision cross-section measurements and studies of nuclear effects relevant for oscillation analyses;
- exploration of astrophysical and geophysical phenomena with medium- and low-energy neutrinos.

Thanks to this breadth of physics opportunities, DUNE is poised to play a leading role in shaping the future of neutrino physics and in probing fundamental symmetries of nature.

2.2 The Neutrino Beam

The LBNF beamline facility, schematically shown in Fig. 2.2, will provide the high-power neutrino source for DUNE. The beam is produced by a megawatt-class proton accelerator at Fermilab and directed towards the Far Detector in South Dakota, 1285 km away. To optimise the sensitivity to oscillation physics at this baseline, the facility will deliver a wide-band, high-purity ν_μ ($\bar{\nu}_\mu$) beam with energies in the range 0.5–10 GeV, and peaking around 2.5 GeV. This energy

coverage ensures access to both the first and second oscillation maxima, located at ∼2.4 GeV and ∼0.8 GeV, respectively.

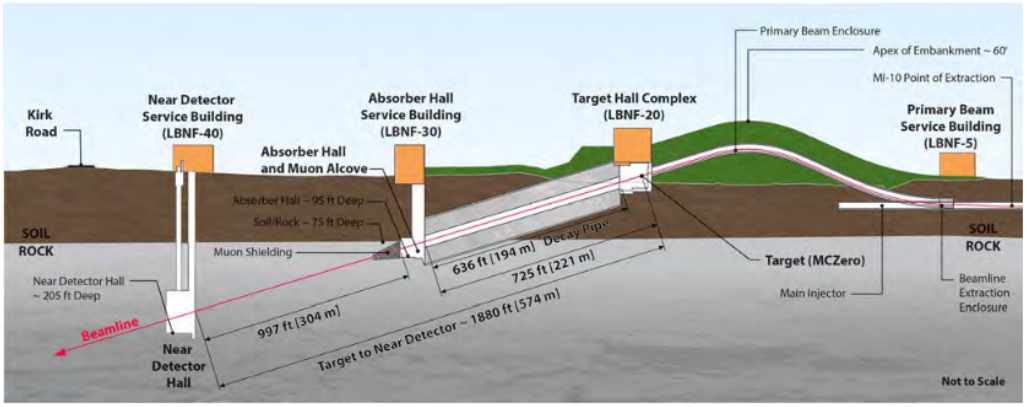

Figure 2.2: Longitudinal section of the LBNF beamline facility at Fermilab[52]

The primary proton beam is extracted from the Main Injector (MI) at the MI-10 straight section using a single-turn extraction. Proton energies are tunable in the range 60–120 GeV. With the Proton Improvement Plan II (PIP-II) upgrade, a single extraction will deliver approximately 7.5×10^{13} protons per cycle (0.7–1.2 s), corresponding to an initial beam power of 1.2 MW. A further upgrade, foreseen by 2030, aims to double the power to 2.4 MW.

Table 2.1 summarizes the main beamline parameters.

Table 2.1: Main parameters of the LBNF proton beam.[52]

Proton energy range	60–120 GeV
Extraction method	Single-turn from MI-10
Protons per cycle	7.5×10^{13}
Spill Duration	9.6 μs
POT per Year	1.1×10^{21}
Cycle length	0.7–1.2 s
Initial beam power	1.2 MW
$\Delta p/p$	$11 \times 10^{-4}(99\%)$
Beam divergence (x,y)	$(15, 17)\mu rad$
Decay pipe length	194 m
Decay pipe diameter	4 m
Target material	Graphite–beryllium
Horn current	$\mathcal{O}(10^5)$ A

Furthermore the spill structure is composed of 6 batches, 84 bunches of σ 1.5 ns each, 2 empty bunches and a $\Delta t = 19$ ns between bunches. After extraction, the

proton beam is transported over a man-made hill, reaching a height of 18.3 m above ground before being bent downward towards the target, located in the LBNF Target Hall. Roughly 85% of the protons interact in a graphite–beryllium target, producing secondary mesons (mainly pions and kaons). These charged hadrons are focused by three magnetic horns with double-parabolic inner conductors, operated at currents of several hundred kA, and directed into a 194 m long, 4 m diameter decay pipe. Meson decays in flight yield the neutrino beam, while hadrons that do not decay are absorbed in a dedicated hadron absorber, consisting of water-cooled aluminum and steel cores surrounded by steel and concrete shielding.

The horns can be operated in two opposite polarity modes: Forward Horn Current (FHC) to focus positive hadrons, producing a ν_μ-dominated beam, or Reverse Horn Current (RHC) to focus negative hadrons, producing a $\bar{\nu}_\mu$-dominated beam. In the oscillation energy region, the resulting fluxes are characterized by:

- a wrong-sign contamination below 10% (e.g. $\bar{\nu}_\mu$ in ν_μ-mode), arising from unfocused hadrons decaying along the beam axis;
- an intrinsic $\nu_e/\bar{\nu}_e$ contamination of $\lesssim 1\%$, due to kaon decays and tertiary muons from pion decays.

Uncertainties on the flux prediction primarily originate from hadron production at the target and from beamline parameter variations, such as horn currents and the horn/target alignment. Figure 2.3 shows the simulated neutrino fluxes for both horn polarities, as obtained with Geant4 simulations.

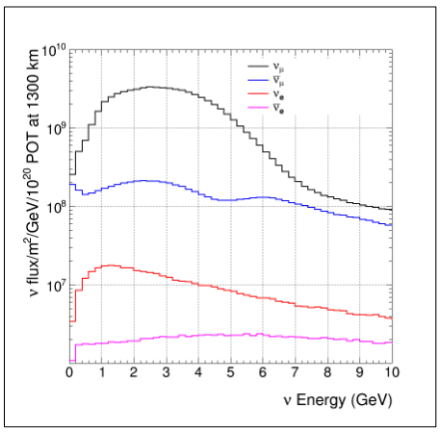

(a) Simulated flux components for ν_μ-mode (FHC).

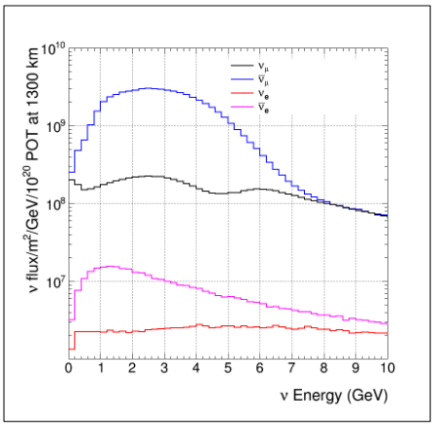

(b) Simulated flux components for $\bar{\nu}_\mu$-mode (RHC).

Figure 2.3: Simulated neutrino flux components at the DUNE Far Detector for both horn polarities. Results are obtained with Geant4 simulations: (a) Forward Horn Current (FHC) producing a ν_μ-dominated beam; (b) Reverse Horn Current (RHC) producing a $\bar{\nu}_\mu$-dominated beam.

2.3 The Far Detector

The DUNE Far Detector (FD) will be constructed at the Sanford Underground Research Facility (SURF) in Lead, South Dakota, located 1,480 m underground (equivalent to 4,300 m.w.e. shielding) to reduce the background from cosmic rays. The FD is positioned 1,285 km downstream of the Long-Baseline Neutrino Facility (LBNF) target at Fermilab, along the neutrino beam axis.

The full FD design foresees four Liquid Argon Time Projection Chamber (LArTPC) modules, each with an active mass of about 17.5 kton. In Phase I, two modules (FD1 and FD2) are scheduled for construction, while the remaining two (FD3 and FD4) are planned for Phase II.

Both FD1 and FD2 adopt single-phase LArTPC technology but feature different drift configurations. FD1 implements a horizontal drift design, already validated through the ProtoDUNE-SP prototype at CERN (about 1/20th of the final FD module size). FD2, instead, will employ a vertical drift design, currently under development to enhance modularity and scalability.

The final configuration of FD3 and FD4 is still under evaluation, with the possibility of adopting alternative designs based on the operational performance of the first two detectors.

Figure 2.4 illustrates the underground cavern at SURF and the planned arrangement of the detector modules.

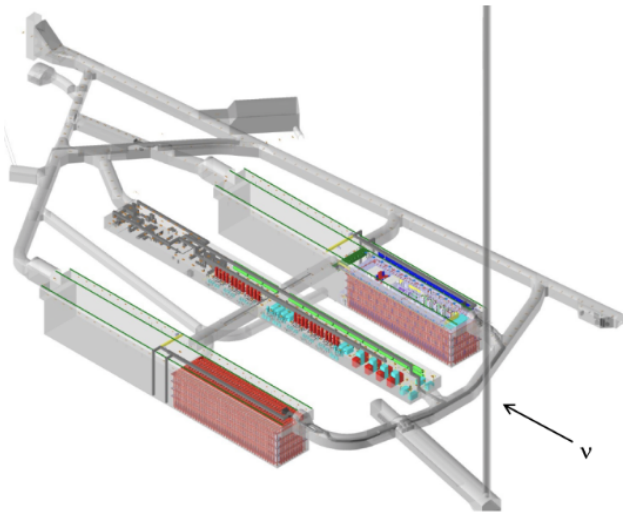

Figure 2.4: Underground caverns for the DUNE FD and cryogenics systems at SURF in South Dakota.

2.3.1 Horizontal Drift (FD1)

The first DUNE Far Detector module (FD1) will adopt a single-phase, horizontal-drift LArTPC design, enclosed within a cryostat measuring 65.8 m × 17.8 m × 18.9 m. The detector has a total liquid argon mass of 17.5 kt, of which at least 10 kt of fiducial volume. An overview of the FD1 layout is shown in Figure 2.5. The active volume is divided into four drift regions by alternating Anode Plane Assemblies (APAs) and Cathode Plane Assemblies (CPAs). Each drift region measures 58.2 m (length) × 3.5 m (width) × 12.0 m (height). A uniform electric field of 511 V/cm is maintained by applying a 180 kV bias to the CPAs, causing ionization electrons to drift horizontally toward the APAs.

The anode walls are built from 150 APAs, arranged in a 2 × 25 grid, with each APA measuring 6.2 m × 2.32 m. Every APA contains three layers of sense wires and is instrumented with ten photon detectors. The wires form a fine grid that collects drifting ionization electrons, while the photon detectors (X-ARAPUCAs) capture scintillation light. The X-ARAPUCA system uses a dichroic short-pass filter to wavelength-shift the 128 nm argon scintillation photons, trapping them within a reflective cavity until they are detected by SiPMs (Silicon Photomultipliers). This provides essential timing information that complements the charge readout from the wire planes. Figure 2.6 shows a schematic of the X-ARAPUCA design.

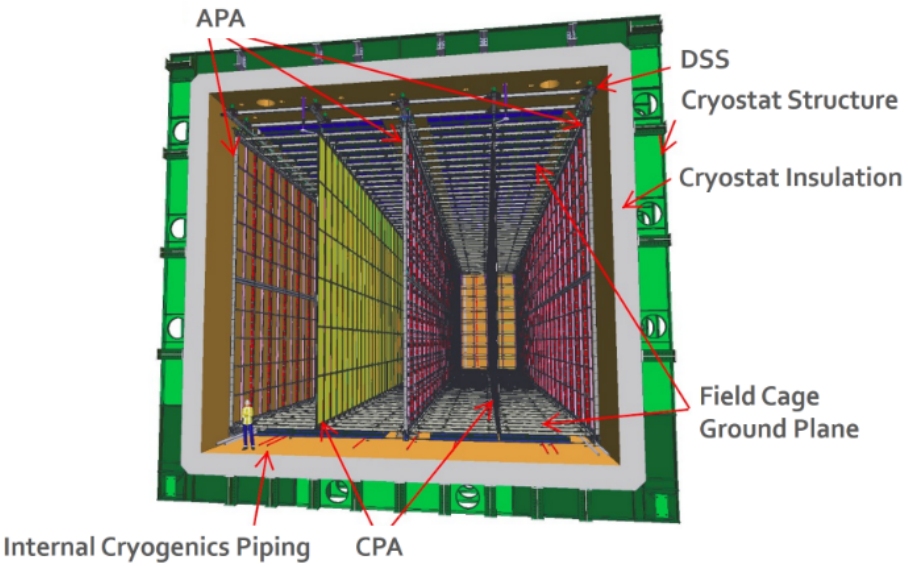

Figure 2.5: 10 kt DUNE far detector module, showing the alternating 58.2 m long, 12.0 m high anode and cathode planes, as well as the field cage that surrounds the drift regions between the anode (APA) and cathode plane (CPA) [53]

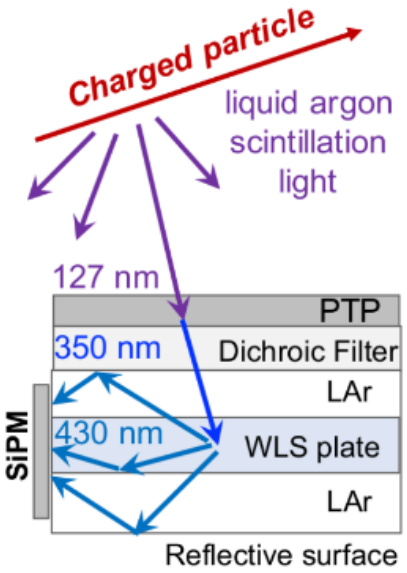

Figure 2.6: Schematic of the X-ARAPUCA working principle [53]

The readout electronics for each APA wall are mounted at the top (upper module) and bottom (lower module) of the detector. On the opposite side of each drift volume, the CPA walls are formed by 100 modules (arranged in a 2 × 25 grid).

The entire active region is surrounded by a field cage, which ensures that the electric field remains uniform across the drift regions, with deviations controlled to better than 1%.

2.3.2 Vertical Drift (FD2)

The second DUNE Far Detector module (FD2) will implement a single-phase vertical drift LArTPC, representing a novel design optimised to maximize fiducial mass and reduce the complexity of readout cabling. The cryostat dimensions are comparable to those of FD1, with an active mass of 17.5 kt and a fiducial mass of approximately 10 kt. A scheme of the detector is shown in figure 2.7.

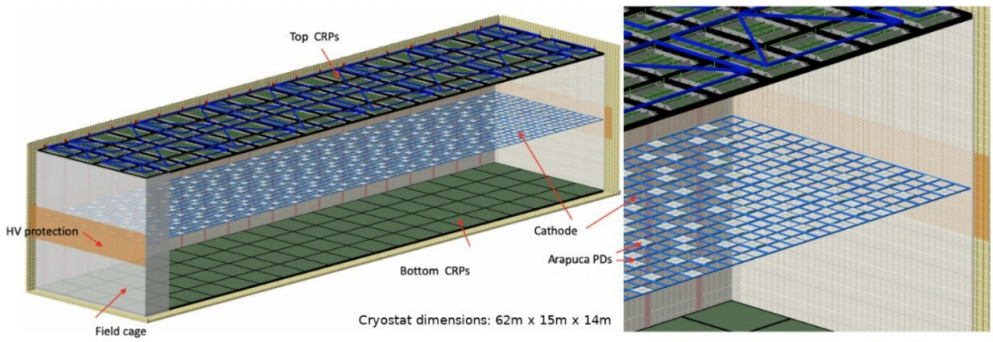

Figure 2.7: Scheme of the vertical drift module, with a zoomed view of the mounting of the photo-sensors

In this configuration, the electric field is oriented vertically, allowing ionization electrons to drift toward anodes located at both the top and bottom of the detector across a maximum drift length of about 6 m. A uniform electric field of 500 V/cm is established by applying a high-voltage bias of around 300 kV to the central cathode positioned at mid-height of the detector, with electrons drifting vertically toward charge-readout planes (CRPs) installed at the top and bottom of the active volume.

Each CRP is equipped with large collection tiles based on segmented pads arranged in a 2D projective readout geometry, enabling fine granularity without the need for long wires as in FD1. n addition to charge collection, scintillation photons are recorded by a photon detection system (PDS) installed along the cryostat walls and on the cathode plane, ensuring precise event timing. This design minimizes the amount of material in the active volume and facilitates modular installation and maintenance.

The advantages of the vertical drift design include a reduced number of read-

out channels relative to the active volume, simplified cold electronics cabling, and an enhanced fiducial-to-active volume ratio. This approach has been validated through the ProtoDUNE-VD program at CERN, where two full-scale prototypes demonstrated stable long drifts and efficient charge collection. Results from these prototypes confirm the feasibility of achieving the performance required for DUNE's physics program.

2.4 The Near Detector (ND)

The Near Detector complex, situated ∼600 meters from the neutrino beam source, consists of three main detectors:

- **ND-LAr**: A Liquid argon time projection chamber;
- **TMS**: A Temporary Muon Spectrometer design for DUNE Phase I, to be raplaced in Phase 2 with ND-GAr, a gaseous Argon TPC;
- **SAND**: The System for on Axis Neutrino Detection;

While both ND-LAr and TMS/ND-GAr will be mounted on rails to allow them to move off-axis relative to the beam direction, SAND will remain fixed in the on-axis position.
The data collection program for off-axis position is commonly known as Precision Reaction-Independent Spectrum Measurement (PRISM).
The ND is designed to measure the ν beam close to its production point, before oscillation, playing also a crucial role in reducing systematic uncertainties and refining the neutrino interaction model. A scheme of the ND is shown in Fig 2.8 and a brief overview of ND-LAr, ND-GAr and TMS is provided below while the SAND detector will be described in detail with all its components in the next chapter 3.

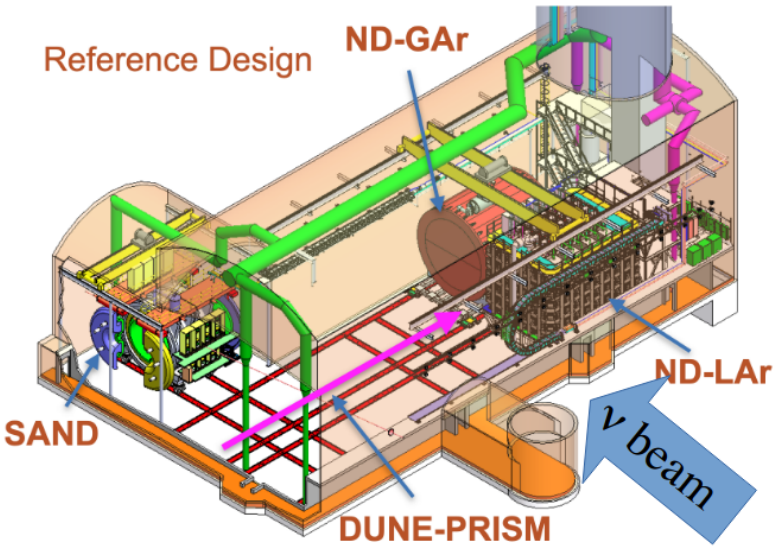

Figure 2.8: Near Detector scheme, showing ND-LAr and ND-GAr off-axis

ND-LAr

ND-LAr is a liquid argon time projection chamber (LArTPC) designed to handle the high events rates that result from the intense neutrino flux at the near site. The design consists of numerous (a 5×17 matrix in the current design) small, optically isolated, TPC modules each equipped with individual pixelated readouts that provide timing information. The small size of each TPC reduces drift distances minimizing the event overlap. The ND-LAr will have a fiducial mass of 67 tons and a total active volume of $5 \times 7 \times 3\ m^3$ with the capability to detect $\approx 10^8 \nu_\mu$ events annually.

ND-GAr

The ND-GAr will feature a high-pressure gaseous argon TPC (HPgTPC) enclosed within an electromagnetic calorimeter both immersed into a 0.5 T magnetic field. This setup will enable the reconstruction of muon momentum and charge for events that occur outside the ND-LAr volume. With an approximate fiducial volume of 1 ton, the ND-GAr is expected to detect around 1.6 $\times 10^6 \nu_\mu$ charged current (CC) events annually when positioned on-axis, providing an independent dataset of neutrino interactions with argon. These events will be analyzed with a low momentum threshold for charged particles, exceptional tracking resolution, and nearly uniform angular coverage, offering systematic uncertainties that differ from those associated with liquid argon detectors.

SAND

The System for on-Axis Neutrino Detection (SAND) will be the only Near Detector that remains permanently in the on-axis position. SAND's primary role will be to monitor the neutrino flux directed towards the Far Detector, while also facilitating an extensive neutrino physics program. Its design largely incorporates components from the KLOE experiment, including the reuse of the magnet and electromagnetic calorimeter (ECAL). Inside the ECAL, a target/tracking system and a small liquid argon volume are installed.

2.5 Physics Program and sensitivities

As introduced in sec. 2.1 DUNE primary science goals are:

- Using $\nu_\mu/\bar{\nu}_\mu$ beams from Fermilab for a comprehensive program of measurements, including:
  - Measurements of the CP phase;
  - Determination of the neutrino mass ordering, i.e. the sign of $\Delta m^2_{31} = m^2_3 - m^2_1$;
  - Measurement of the mixing angle θ_{23}, and the octant in which the angle lies;
  - Sensitive tests of the three-neutrino paradigm;
- Search for proton decay in several decay modes;
- In the occurrence of a core-collapse supernova in our galaxy during the lifetime of the DUNE experiment, detect and measure the corresponding ν_e flux towards the Earth that will be generated;

2.5.1 Oscillation parameters sensitivity

Using a complete end-to-end simulation, including reconstruction and event selection processes, the sensitivity to oscillation parameters has been evaluated. The results of this analysis, that incorporates the geometries of both the Far and Near Detectors along with flux uncertaintes and the neutrino interaction, indicate that DUNE will be capable of making precise measurements of long-baseline neutrino oscillation parameters simultaneosly with no external constraints.
Fig 2.9 shows this capability, illustrating the $90\% C.L.$ regions in the $sin^2 2\theta_{13} - \delta_{CP}/\pi$ and $\Delta m^2_{32} - sin^2\theta_{23}$ planes for 7,10 and 15 years of operations and are compared with the current global fit result from world data, showing how DUNE will

be able to resolve potential degeneracies and tightly constrain these parameters.

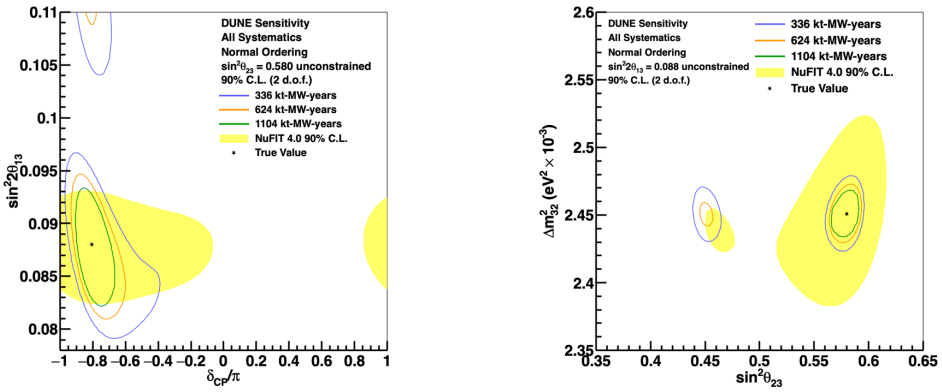

(a) (b)

Figure 2.9: (a) 90% confidence level in $sin^2 2\theta_{13} - \delta_{CP}/\pi$ plane; (b) 90% confidence level in $\Delta m^2_{32} - sin^2\theta_{23}$ plane. The yellow region corresponds to the 90% C.L. of the NuFIT global fit for comparison. [54]

The DUNE experiment will also determine the neutrino mass ordering by disentangling matter effects from CP violation effects. This is made possible by the long 1300 km baseline, which amplifies the impact of matter effects. These effects introduce a large asymmetry between the oscillation probabilities of neutrinos and antineutrinos that depends directly on the mass ordering. At this distance, the asymmetry is expected to reach about $\pm 40\%$, significantly larger than the maximum asymmetry induced by the CP-violating phase δ_{CP}. This strong enhancement enables DUNE to achieve simultaneous sensitivity to both the mass ordering and δ_{CP} [48].

Figure 2.10 shows the projected sensitivity as a function of exposure for a fixed δ_{CP}. DUNE can determine the mass ordering with at least 5σ confidence, independent of δ_{CP}, after an exposure of about 100 kt $\cdot$ MW $\cdot$ years (roughly three years of data) [54]. In favorable conditions, such as certain δ_{CP} values and tighter external constraints on θ_{13}, this significance could be reached in less than a year, as shown in the left panel of Fig. 2.11.

For CP violation, the sensitivity strongly depends on the true value of δ_{CP}. If $\delta_{CP} = -\pi/2$ (maximal CP violation), DUNE can achieve 3σ (5σ) sensitivity with exposures of about 100 (350) kt $\cdot$ MW $\cdot$ years, respectively. For non-maximal CP violation, a 5σ discovery is possible for around half of all δ_{CP} values with 10 years of data, while about 13 years are required to reach 3σ sensitivity for 75% of δ_{CP} values. This is illustrated in the right panel of Fig. 2.11, where the role of external

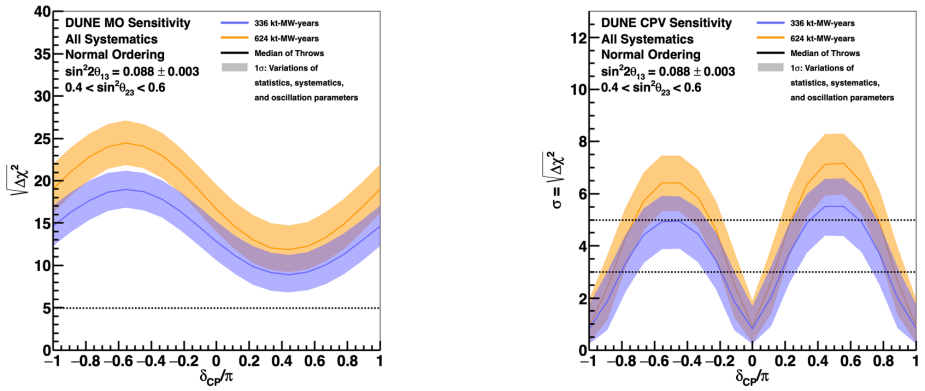

(a) (b)

Figure 2.10: (a) Sensitivity to neutrino mass ordering (left); (b) Sensitivity to CP Violation. with the Phase II Near Detector, shown for different exposure levels as a function of the true δCP value. The solid lines indicate the median sensitivity, while the shaded bands represent the 68% confidence interval, accounting for variations in statistics, systematics, and oscillation parameters [54]

constraints on θ_{13} is again highlighted.

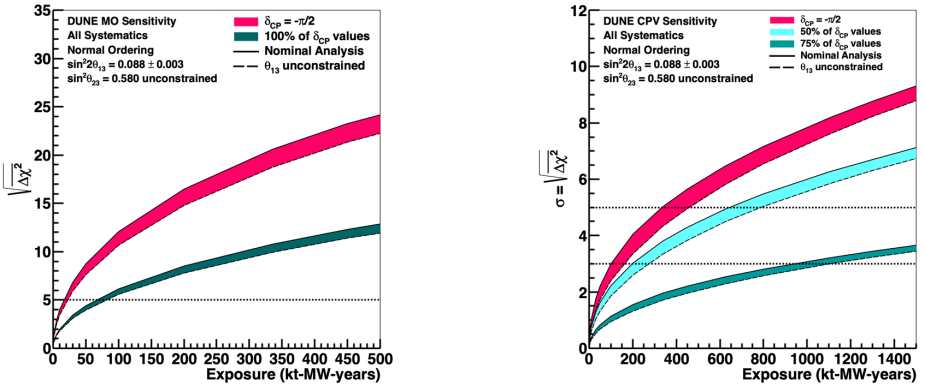

(a) (b)

Figure 2.11: (a) Sensitivity to neutrino mass ordering; (b) Sensitivity to CP Violation. with the Phase II Near Detectoras a function of exposure in kt MW-years. The width of the bands illustrates the difference between the nominal analysis (solid line), which includes the external constraint from reactor antineutrino experiments on $sin^2\theta_{13}$, and an analysis without this constraint (dotted line) [54]

The oscillation disappearance channel $\nu_\mu \to \nu_\mu$ is especially sensitive to $\sin^2 2\theta_{23}$, while the appearance channel $\nu_\mu \to \nu_e$ depends on $\sin^2 \theta_{23}$. By combining mea-

surements from both channels, DUNE will be able to resolve the θ_{23} octant and test the hypothesis of maximal mixing. Figure 2.12 shows the projected sensitivity to the θ_{23} octant as a function of the true value of $\sin^2 2\theta_{23}$, for exposures corresponding to 10 and 15 years of data.

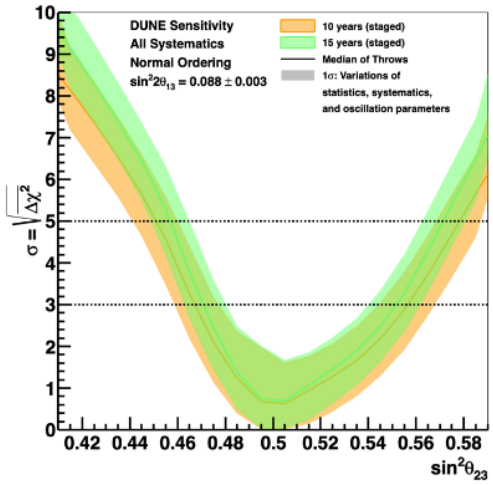

Figure 2.12: $sin^2\theta_{23}$ Sensitivity. [51]

Achieving these physics goals will require stringent control of systematic uncertainties. This will be ensured primarily through the constraints provided by the Near Detector. The sensitivities reported here are based on detailed studies of systematic effects, incorporating inputs from both the Near and Far Detectors.

2.5.2 Supernova Neutrinos

DUNE, thanks to the substantial mass employed by its detectors, will be able to detect low-energy neutrinos in the range of 5 to few tens of MeV, giving it the capability to observe in particular electron neutrinos from galatic core-collapse supernovas. Though these events are expected to occur only a few times per century, it is likely that one could be detected during the experiment's operation period. The neutrino signal produced by the core-collapse supernova evolves over time, from a sharp burst of ν_e that corresponds to the neutronization phase of the core collapse, to the following phases of acceleration and cooling that lasts respectively several hunders milliseconds and $\approx$ 10 seconds. As shown in Fig. 2.13 the neutrino flux during these phases include nearly equal proportions of all ν and $\bar{\nu}$ flavors. The study of this signal can yield insights into the dynamics of the core collapse, the nature of the progenitor star, explosion mechanics and properties of the neutrino themselves.

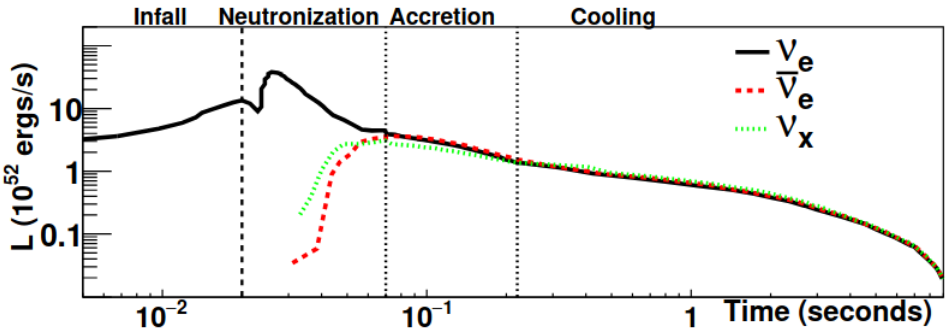

Figure 2.13: Supernova luminosity as function of time from the core bounce of an electron capture supernova [51]

DUNE sensitivity allow for other meaningfull studies sush as:

- Determine parameters of the electron neutrino spectrum (Fig. 2.14)by obeserving neutrinos from supernova at distance of 10 kpc, $\mathcal{O}(3000)$ are expected to be seen during the experiment operational time.
- Reconstrut the direction of incoming neutrinos to pintpoint supernova's location in the sky, contribuiting to global multi-messanger astronomy efforts;
- Investigate flavor oscillation probabilities during supernova burst that are highly affected by the burst's dynamic itself and by the neutrino mass ordering.

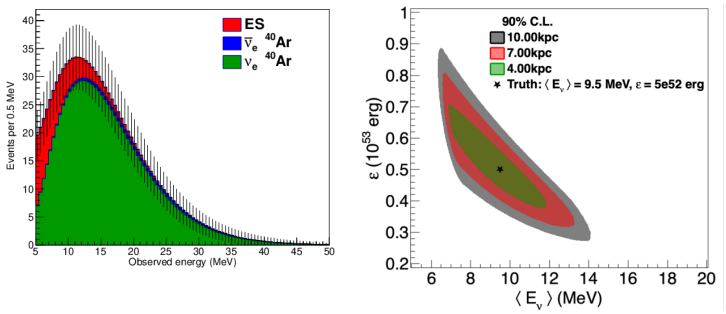

Figure 2.14: (Left) Expected spectrum as a function of the observed energy assuming no flavor transformation; (Right) Sensitivity regions to E_ν and supernova energy ϵ for three different supernova distances with 40k fiducial mass.[54]

2.5.3 BSM Studies

Thanks to the Far Detector's undergorund location that reduces significantly the natural background, DUNE has enhanced sensitivity to nucleon decay and other processes that increase its potential for Beyond Standard Model searches such as:

- Probe a broad range of possible sterile neutrino mass splittings, thanks to both the long and short baseline, by looking at disappearance of charged current and neutral-current neutrino interaction.
- Search for dark matter both at near and far detector due to the unprecedented neutrino beam intensity that allows for testing the production of low mass dark matter
- Search for Heavy Neutral Leptons in the Near Detector facility;
- Search for baryon number violation processes, such as proton decay in the channel $p \to K^+\bar{\nu}$ or neutron decay $n \to e^- K^+$

Chapter 3

System for on-Axis Neutrino Detection

As introduced in 2.4 the System for on-Axis Neutrino Detection (SAND) is one of the three detector components of the DUNE Near Detector (ND).
Designed to be a multipurpose detector, it will be able to detect neutrino interactions on different target materials, including argon and hydrogen, performing precision tracking and calorimetry measurements. DUNE accelerator-based physics studies rely on assumptions about flux uncertainties, where parameters like horn positions and currents are within set tolerances. These parameters are monitored by beamline instrumentations, but possible deviations are best detected by analyzing neutrino energy spectra in the ND. Beamline distorsions are most evident on-Axis while becoming diluted off-axis. The DUNE-PRISM physics program requires both ND-LAr and ND-GAr to collect data off-axis 50% of the time and depends on the known relationships between off-axis angles and the neutrino energy spectrum. Thus for DUNE-PRISM to function effectively, beam stability is crucial for data colletion and distortions must be quickly identified and modeled, requiring continuous on-axis beam monitoring: a task that will be carried out by SAND.

3.1 Physics Program

The number of events for the exclusive process X, with signal detected in both ND and FD detectors can be written as:

$$N_X(E_{rec}) = \int_{E_\nu} dE_\nu \Phi(E_\nu) P_{osc}(E_\nu) \sigma_X(E_\nu) R_{phys}(E_{vis}, E_\nu) R_{det}(E_{vis}, E_{rec}) \quad (3.1)$$

in which:

- Φ is the coming (anti) neutrino flux;
- σ_X is the cross-section for the process X;
- R_{phys} is the physics response function introduced by the nuclear smearing resulting in the visible final state particles;

- R_{det} is the acceptance for the visible final state particle;
- E_ν and E_{rec} are the true and reconstructed energy of the neutrino respectively.
- E_{vis} is the total energy of the visible final state particles;
- $P_{osc}(E_\nu)$ is the neutrino oscillation probability.

All the main terms of Eq. 3.1 are folded together into the observed events distributions and cannot be decoupled by using a single detector or nuclear target. The success of the DUNE oscillation program critically depends on the precise control of systematic uncertainties, in particular those related to neutrino cross-sections and energy reconstruction on argon. The use of argon alone as a nuclear target in the Near Detector is not sufficient, since nuclear effects, final-state interactions, and model dependencies introduce large uncertainties that cannot be unfolded with a single target. Moreover, degeneracies among interaction modeling, nuclear effects, and detector smearing prevent a reliable constraint of the energy scale using only NDLAr and DUNE-PRISM. For this reason, the ND complex is complemented by SAND that employs additional nuclear targets and subsystems. SAND provides continuous monitoring of the beam spectrum, independent cross-section measurements on multiple targets (including light nuclei), and complementary information to reduce the model-dependence of the oscillation analysis. In this way, it plays a central role in ensuring the robustness of the DUNE physics program.

3.1.1 Flux Measurements

The flux measurements that SAND will be able to perform on-axis of all neutrino flavor at DUNE ND are the following:

- Absolute ν_μ flux from elastic scattering $\nu e \to \nu e$. The signal will be a single target electron moving forward as a final state, the cross-section of the process is well known;
- Absolute and relative $\bar{\nu}_\mu$ flux from $\bar{\nu}_\mu p \to \mu^+ n$ QE on Hydrogen with $Q^2 \sim 0$. At such low values of Q^2 the cross-section is a constant determined by neutron β decay;
- Relative ν_μ and $\bar{\nu}_\mu$ fluxes vs E_ν from $\nu(\bar{\nu}) \to \mu^\pm p \pi^\pm$ on H with $E_\nu < 0.5\ GeV$;
- Relative $\bar{\nu}$ fluxes vs E_ν from $\bar{\nu} p \to \mu^+ + n$ (QE with $E_\nu < 0.25\ GeV$);
- Ratio of $\bar{\nu}_\mu/\nu_\mu$ fluxes vs E_ν from coherent π^-/π^+ production on Carbon target: performed by measuring the ratios within the same beam polarity

and coherent interaction on C inside the CH_2 and graphite target;

- Ratio of ν_e/ν_μ and $\bar{\nu}_e/\bar{\nu}_\mu$ from (anti)neutrino CC interactions on Hydrogen;

3.1.2 Constraints on nuclear effects

To constraint nuclear effects in Argon presents in Eq. 3.1 it is necessary to obtain a comparison between different neutrino-nucleus interaction topologies.
Interactions of (anti)neutrinos with Hydrogen are of particular importance since scattering on H and elastic scattering on electrons are the only types of interactions free of nuclear effects. Thus, CC interactions on a Hydrogen target provide insights on the structure of the free nucleon and useful information on systematics uncertainties related to the nuclear smearing.
To achieve this, the SAND Tracker design, discussed in 3.2.2, will have different nuclear targets, including CH_2 and graphite (pure C) plates, that will allow by subtracting the background from C from interactions in CH_2 to identify $\nu(\bar{\nu}) - H$ interactions. This can be done by exploiting the kinematic of the two processes, on a H target at rest the ν CC events are predicted to be perfectly balanced in the transverse plane to the direction of the beam, therefore the resulting muons and hadron vectors are expected to be found on the same plane. On the other hand, ν interactions on heavier nuclei are largely affected by initial and final nuclear smearing, resulting in a significant missing transverse momentum. The kinematic selection shows that a purity of $80-95\%$ can be achieved on the selected H samples and the efficiencies on the kinematic selection would be in the range of $75-95\%$ depending on the processes.
By combining the information provided by the Tracker and a LAr meniscus (see sec. 3.2.1 on GRAIN below) SAND will be able to constraint the nuclear smearing for the ND beam spectrum. From Eq. 3.1, SAND will directly constraint $\sigma_{\nu(\bar{\nu})} R_{phys}$, by comparing (anti)neitrino interactions between Ar and H. For H targets $R_{phys} \equiv 1$ and the cross section can be measured thanks to the large expected statistics. The unfolding of the convolution $\sigma_\nu R_{phys} R_{det}$ depends on the detector resolution $\sigma(p)/p$ and the calibration precision (0.2% is expected exploiting the reconstruction of $K^0 \to \pi^+\pi^-$).

3.1.3 Precision measurements on nucleon structure investigation

SAND will be able to perform precise masurement of the weak mixing angle $sin^2\theta_W$ in (anti)neutrino scattering at the DUNE energies. A measurment of the angle can be obtained by the ratio of NC and CC deep inelastic scattering (DIS) neutrino interactions $\mathcal{R} \equiv \sigma_{NC}/\sigma_{CC}$. Another possibility to measure the mixing parameter can be provided studying NC $\nu_\mu e$ elastic scattering, extracting the

value of $sin^2\theta_W$ from the ratio $\mathcal{R}_{\nu_e} \equiv \sigma(\bar{\nu}_\mu e \to \bar{\nu}_\mu e)/\sigma(\nu_\mu e \to \nu_\mu e)$.
Furthermore due to the possibility to integrate various thin nuclear targets within the Tracker, SAND will allow to inspect nucleon structure disentangling nuclear effects. Using both ν and $\bar{\nu}$ DIS, the parton distribution functions, cross sections, perturbative and non-perturbative corrections can be studied in a wide range of transfer momentum Q^2 and Bjorke variable x.
SAND will also investigate the isospin and the number of valence quarks of the target taking advantage of the presence of H and other nuclei in the Tracker. The aviability of large samples of (anti)neutrino interactions on Hydrogen will allow a precision test of the Adler sum rule $S_A = 0.5 \int_0^1 dx/x(F_2^{\bar{\nu}p} - F_2^{\nu p}) = I_p$ giving the isospin of the target, and the Gross-Lewellyn Smith (GLS) sum rule $S_{GLS} = 0.5 \int_1^0 dx/x(xF_3^{\bar{\nu}p} + xF_3^{\nu p})$. The Adler sum, in the quark-parton model, corresponds to the difference between number of valence u and d quarks of the target. The structure functions $F_2^{\bar{\nu}p}$ and $F_2^{\nu p}$ can be obtainend from the differential cross section on H, as well as the sum as a function of the momentum transfer Q^2. The GLS sum gives instead the number of valence quarks in the nucleon and can be also used to obtain the strong coupling constant $\alpha_s(Q^2)$.

3.1.4 Search for new physics

SAND will also allow studies on possible BSM physics effects looking for deviations from SM predictions in specific observables.
Possible oscillations into sterile neutrinos can be identified studying CC ratios $\mathcal{R}_{e\mu}(L/E) \equiv (\nu_e N \to e^- X)/(\nu_\mu N \to \mu^- X)$ and $\bar{\mathcal{R}}_{e\mu}(L/E) \equiv (\bar{\nu}_e N \to e^+ X)/(\bar{\nu}_\mu N \to \mu^+ X)$ and NC/CC ratios $\mathcal{R}_{\nu p}$ and $\bar{\mathcal{R}}_{\bar{\nu}p}$ as a function of the source-detector distance and the neutrino energy ratio. Finally, the unique set of features provided by SAND can significantly enhance the physics sensitivity of the ND complex in the search for heavy sterile neutrinos, light Dark Matter, dark photons and more.

3.2 Design

The SAND design is mostly based on the reproposal of the electromagnetic calorimeter (ECAL), described in detail in 3.2.3, and the superconducting magnet of the K LOng Experiment (KLOE) [55]. The KLOE detector was primarly designed for the study of charge parity (CP) violation in the neutral kaon system decay at the $DA\Phi NE$ Φ-factory and took data from April 1999 to March 2018 with stable performance for the entire period. This well known performance of the KLOE devices [56] is enhanced in SAND with a LAr active target (GRAIN) and a low density tracking system. The configuration of the subdetectors is shown in Fig. 3.1 and results in a multipurpose detector that allows for the precision measure-

ments required for its broad physics program discussed in sec. 3.1 A description

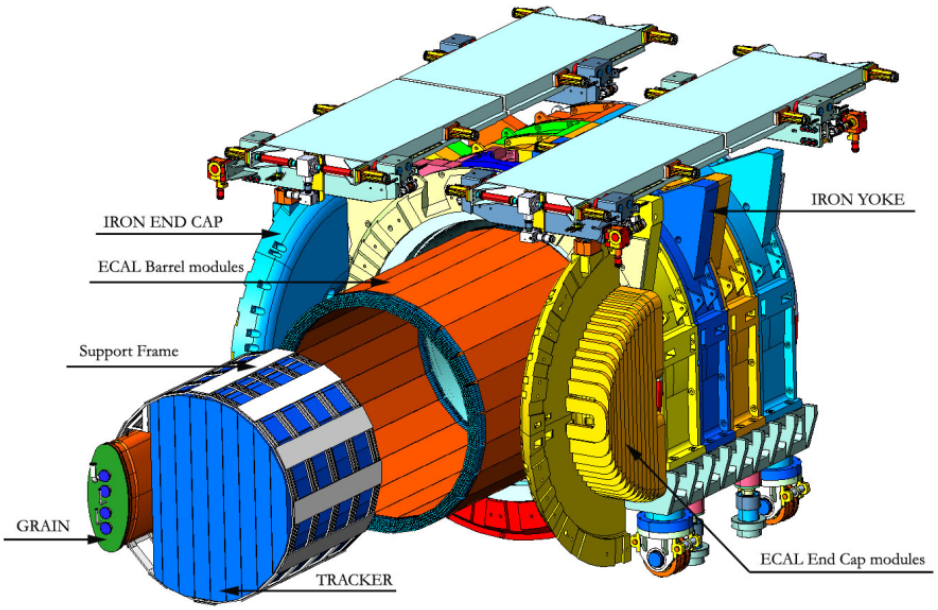

Figure 3.1: System for on-Axis Neutrino Detection scheme.

of the different detector components is illustrated in the following sections.

3.2.1 GRAIN

In the upstream part of the SAND inner volume, in front of the tracking system, a volume of about 1 ton of active liquid Argon target will be placed, called the GRanular Argon for INteractions of Neutrinos (GRAIN). This volume provides on axis data for neutrino-Argon interactions as supplement to those off-axis taken by ND-LAr. An overview of GRAIN is presented in Fig. 3.2. The volume is not designed to be only a passive target but will also be able to actively reconstruct the charged particle trajectories propagating in the liquid Argon using only the scintillation light. In fact due to the high event rate and pile-up expected for events in GRAIN, the established technology for tracking and reconstruction in LAr, the TPC, cannot be easily applied.
While one potential solution is to use a design similar to ND-LAr, emplyoing arrays of small LArTPCs, a novel R&D program is exploring a tracking and calorimetry system based entirely on imaging LAr scintillation light. The outer vessel is 190 cm high, 200 cm wide and with a maximum thickness along the beam direction of 83 cm. It is constructed from carbon fiber and honeycomb to minimize external material. The inner vessel is made of stainless steel, with a height of 147 cm, a width of 150 cm and a maximum depth of 47 cm. The overall thickness of vessels,

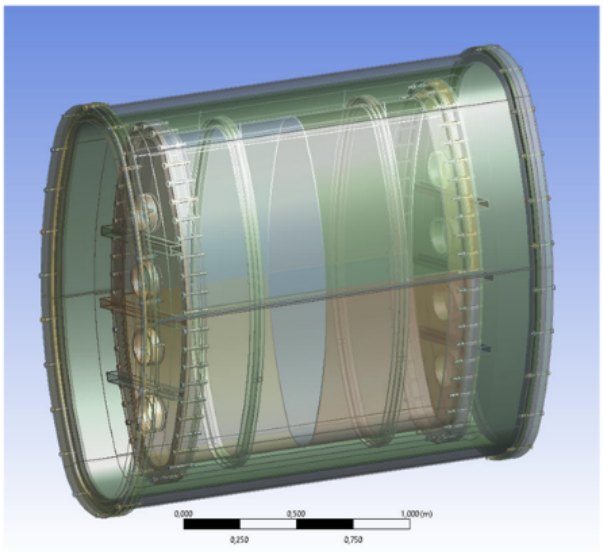

Figure 1.81: GRAIN cryostat.

Figure 3.2: GRAIN cryostat and internal vessel overview. The internal vessel has an elliptical transverse base with axes measuring 49cm and 148cm and a longitudinal length of 150cm. It is designed to store 1 t of LAr and withstand an internal pressure of 1.5 bar

6 mm, was kept as thin as possible to minimize the energy loss, showering and multiple scattering in the passive material. The presented design minimizes vessel material resulting in a thickness that is only a small fraction of a radiation length, while the LAr volume's overall depth is about one radiation length reducing energy loss, showering and scattering allowing the outgoing particles to be analyzed by downstream detector elements. The GRAIN design is optimised to provide calorimetric information and spatial reconstruction of the neutrino-argon interactions. To this end, an optical system coupled to a fast, segmented photon detector is needed. The light collection is performed by Vacuum Ultraviolet camers operating at LAr temperatures and two optical systems are currently in development: one based on lenses and one based on Coded Aperture Masks. Both systems use SiPM matrices with a wavelength-shifter to convert UV light into visible light where SiPMs have their optimal photon detection efficency.

3.2.2 Tracker

As per DUNE Conceptual Design Report [48], SAND inner tracker has to include the following capabilities:

- low avarage density ($\rho < 0.1 g/cm^3$) to minimize multiple scattering and

allow precision magnetic spectrometry;

- enough targhet mass to have a sufficient interaction rate;
- The two requirements above lead to a total thickness of each tracker module (see below) of ≈ 1 radiation length to precisely measure curvatures in particular for electron/positrons;
- possibility to measure interactions on free protons (H) by subtracting measurements taken on pure carbon targets and polypropylene targets as discussed in sec. 3.1;
- Deplyoing other nuclear targets for $\nu - Ar$ $\nu - H$ interaction comparisons.

To achieve these goals two solutions are viable: Straw Tube Target Tracker (STT) and a Drift Chamber. While different, both options have uniformely distributed target mass across the tracking volume mantaining low density and retaining 97% of the total detector mass, thanks to the use thin layers of 100% chemically pure materials. Both solutions that will be explored in the following , have about the same target mass and average density with a slightly shorter total radiation length for the STT.

STT Tracker

The defulte STT module, showed in Fig. 3.3, consists of:

- 5 mm thick solid polypropylene target slab;
- polypropylene radiator composed of 105 foils of 18 μm thick, with air gaps 117μm thick;
- four layers of straws arranged in a XXYY pattern, each straw having a 5mm diamaeter and 12 μm Mylar walls coated with Al, and a 20 μm tungsten wire coated with gold.

In the current design a total number of 86 modules and a total of 344 straw planes are present.

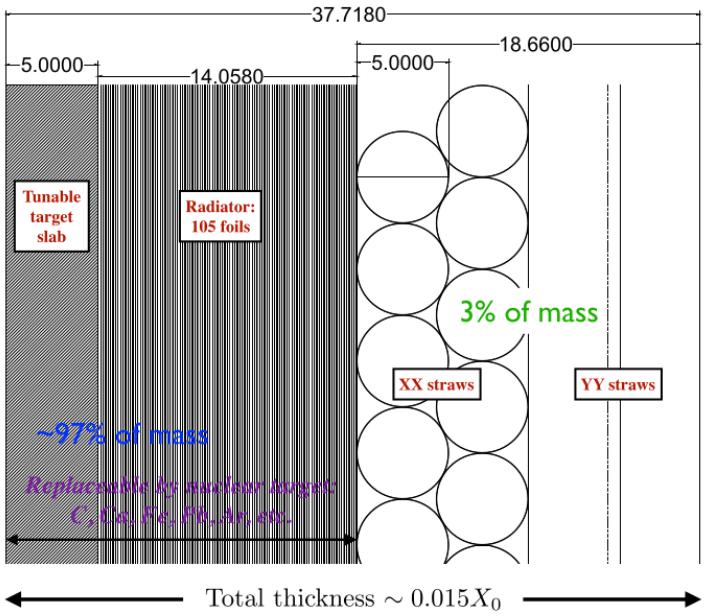

Figure 3.3: Default STT module, with a tunable polypropylene target, a radiator, and four layers of straw with a XXYY arrangement. All dimensions are in mm.

Drift tracker

The basic volume of the geometry, shown in Fig. 3.4, is made of:

- 5mm (4mm) of solid polypropylene (Carbon) target;
- three planes of wires with alternated signal and field wires spaced along the planes by 1 cm. Each plane of wires is 1 cm thick and it is separated from the next by a 20μm thickness mylar plane for a total of 4 planes.

The stations composed by planes of wires are filled with a mixture of Ar/CO_2 gas in proportion 85/15 at 1 atm plus 10 mbar overpressure with a density of 0.002 g/cm^3. In the current design, a module with Carbon target followed by 9 modules with CH_2 target packed in an unique Carbon frame define a so called supermodule.
The orientation of the wires can differ from station to station.

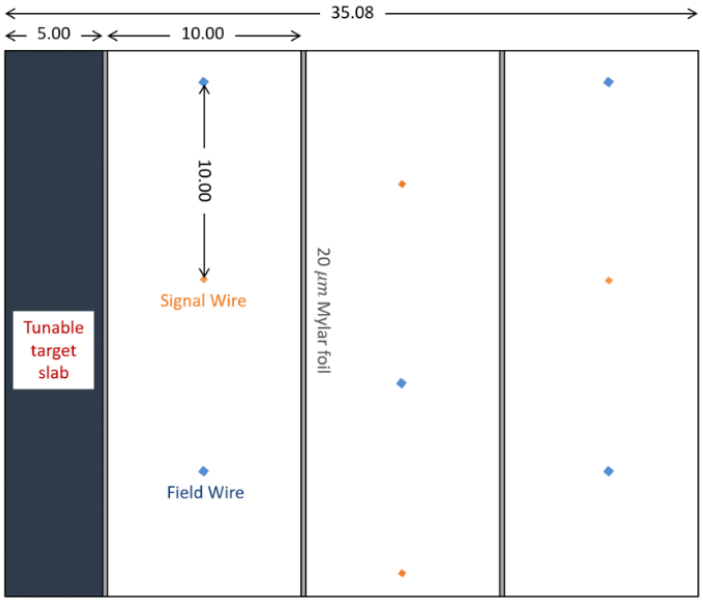

Figure 3.4: Default drift module with a target, three drift planes with alternated field and signal wires interspaced with thin Mylar foils. The height of each module depends on the module position inside the SAND tracking module and can range from about 3 to 4 meters. All dimensions are in mm.

3.2.3 The SAND Electromagnetic Calorimeter

Design and performance of the KLOE electromagnetic calorimeter (ECAL) are presented in this section.The ECAL is a lead-scintillating fiber sampling calorimeter, and scintillating fibers offer high light transmission over several meters, sub-ns timing accuracy and very good hermeticity. A scheme of the ECAL is shown in Fig. 3.5

Design and Structure

The KLOE ECAL is a fine sampling lead-scintillating calorimeter with photomultiplier tubes (PMT) readout. The central part(barrel) approximating a cylindrical shell of 4 m inner diameter, 4.3 m active length and 23 cm thickness ($\sim$ 15 radiation length), consists of 24 modules with trapezoidal cross section and fibers running parallel to the cylinder axis. Two endcaps close the barrel hemetically. Each of them consists of 32 "C" shaped modules arranged vertically along the chords of the circle inscribed in the barrel. In the endcap modules fibers run perpendicular to the cylinder axis so that the whole ECAL fibers are mostly transverse to the particle trajectories. The modules are read out on the two sides through Plexi-

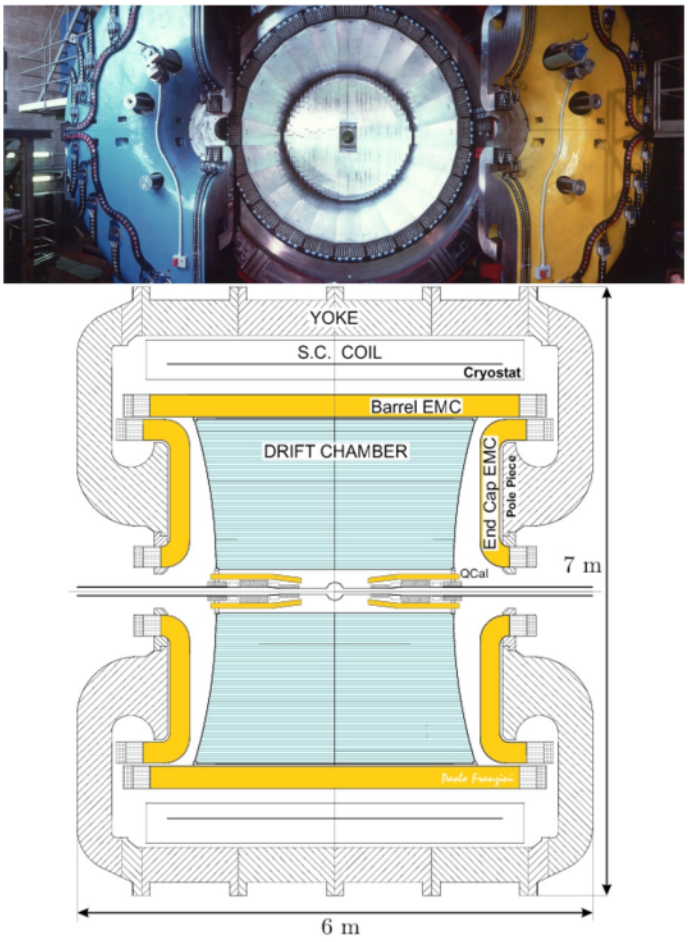

Figure 3.5: KLOE Picture (top), KLOE scheme (bottom) [56].

glas light guides optically coupled to fine mesh PMTs. The readout granularity is $\sim 4.4 \times 4.4\ cm^2$, corresponding to the dimensions of the basic elements of each module, called cells, arranged in five layers. Each barrel module has 60 channels per side while endcap modules have 10, 15 or 30 channels per side depending on their width. The total number of readout channels is 4880, corresponding to a total of 2440 cells which are read-out at both ends. Both in the barrel and in the endcaps, PMT axes are almost parallel to the magnetic field, in order to decrease the field effects on PMT response, and to increase hermeticity.
The basic calorimeter structure consists of an alternating stack of 1 mm scintillating fiber layers glued between thin grooved lead foils, obtained by passing 0.5 mm thick lead foils through rollers of a proper shape. The grooves in the two sides of each foil are displaced half a pitch, so that fibers are located at the corners of adjacent, quasi-equilateral triangles, resulting in an optimal and uniform

arrangement of the fibers in the stack. The final composite has a fiber : lead : glue volume ratio of approximately 48 : 42 : 10, a density of $\sim 5 g/cm^3$ and a radiation length X_0 of $\sim 1.6 cm$. Furthermore it is self-supporting and can be easily machined, as shown in Fig. 3.6. The efficiency for low-energy photons is high due to the very small lead foil thickness($< 0.1 X_0$)

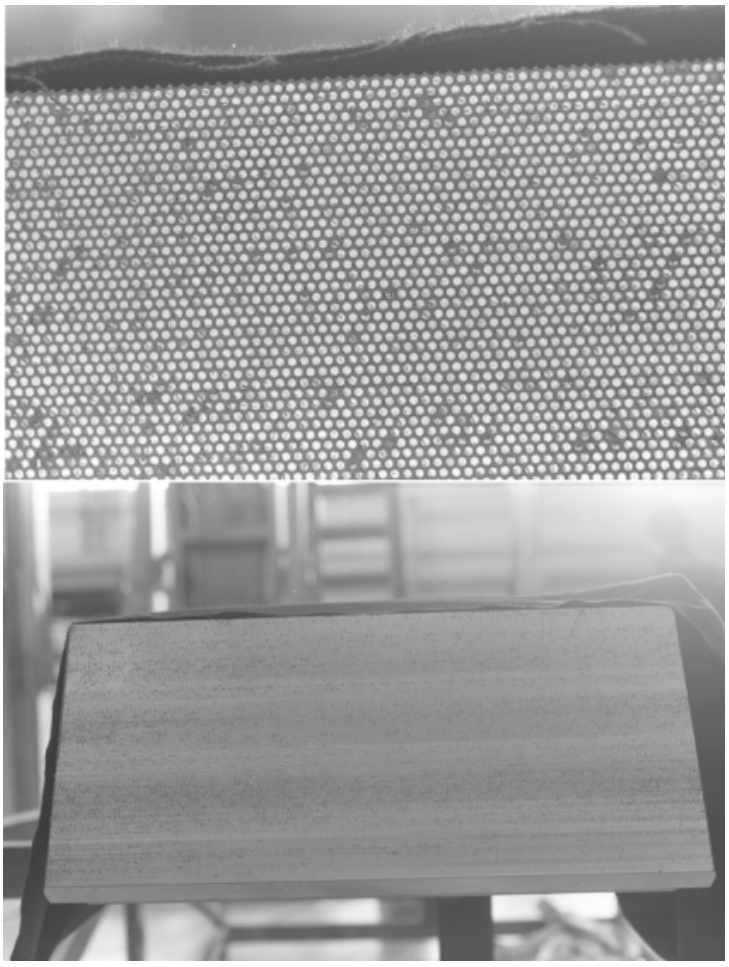

Figure 3.6: KLOE ECAL lead-fiber structure detail (top) and barrel module cross section view (bottom).

Scintillating Fibers

Two types of fibers (Kuraray SCSF-813 and Pol.Hi.Tech. 0046) with a total length of 15,000 km have been used to assembly the ECAL. The former have higher light output and longer attenuation length, the latter are less expensive. The performance differences are not significant, and the Kuraray fibers are used

in the inner half of the calorimeter. All fibers have an attenuation length between 3 and 5 m and produce $\sim$ 1 PE for 1 mm of crossed fiber at a distance of 2 m from a PMT. The emitted light is in the blue-green region ($\lambda_{peak} \sim 460nm$)

PhotoMultipliers

The light guides matching the module end faces to the photo-tube windows begin with a mixing section and terminate with a Winston cone , passing from an approximately squared to a circular area with a concentration factor of $\sim$ 4 as shown in Fig. 3.7. The PMTs must operate in a magnetic field with the suit-

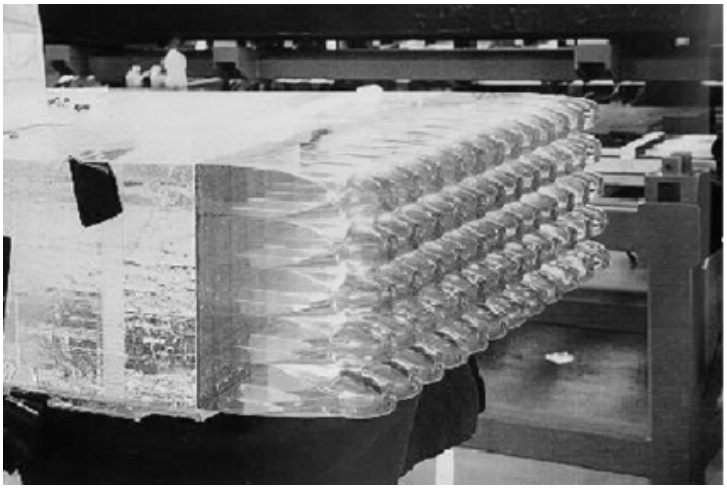

Figure 3.7: Light guides at one end of a KLOE ECAL barrel module before PMT installation.

able efficiency, linearity, timing resolution and dynamic range. The Hamamatsu R5946/01 1.5" tubes have been chosen because the electron multiplication occurs between dynodes made of fine mesh, very close to each other. Then the effect of the magnetic field on the electron path is very small. The field intensity at the PMT location is less than 0.2 T, and the PMT alignment is such that the component transverse to the tube axis is less than 0.07 T. Measurements show that the PMT gain decreases by 10% when the field is on, but linearity and resolution are not affected. The PMTs are operated with grounded cathodes in order to eliminate leakage, a possible origin of noise and field distortions. A thin aluminum cylinder holds each PMT mechanically in place, and a spring pushes it gently against the light guide. Bicron optical gel BC-630 forms the optical contact between the PMT and the light guide. Each PMT is connected to a base which hosts the high voltage divider and a preamplifier (see Fig. 3.8). The PMT-base has low noise, high bandwidth and high output dynamic range in order to avoid distortion of the

Figure 3.8: KLOE PMT-base.

fast pulses from the PMT. The cables carrying high and low voltage, a test pulse and the output signal are connected to the PMT-base through its rear connector.

Performances in KLOE

In KLOE the signal from the PMT is split three ways. One split signal is used for analog sums for trigger purposes. Two split signals are sent to ADC and to TDC boards after discrimination. The TDC signal is delayed by a monostable while a continuous sampling technique is used for the ADC. The ADC is coupled to an analog integrator, and the signal of the integrator is sampled every 450 ns by two sample and hold circuits. After the trigger, a third sampling of the integrator is performed and the value of the buffered signal is subtracted to compute the signal charge. A detailed description on the time and energy calibration of these signals and the alternative strategies for calibration in the ND site, will be illustrated in 5.

The ECAL time resolution has been evaluated using $\phi \to \eta\gamma, \phi \to \pi^0\gamma, e^+e^- \to e^+e^-\gamma$ events as showed in Fig. 3.9 , and by the standard deviation of the $t - r/c$ distribution σ_t is obtained :

$$\sigma_t = \frac{54ps}{\sqrt{E(GeV)}} \oplus 140ps \tag{3.2}$$

in which the 140 ps constant term is due to residual detector miscalibration of the order of 100ps, time jitter of the RF coincidence and the uncertainty on the interaction point position due to the finite length of the bunches.

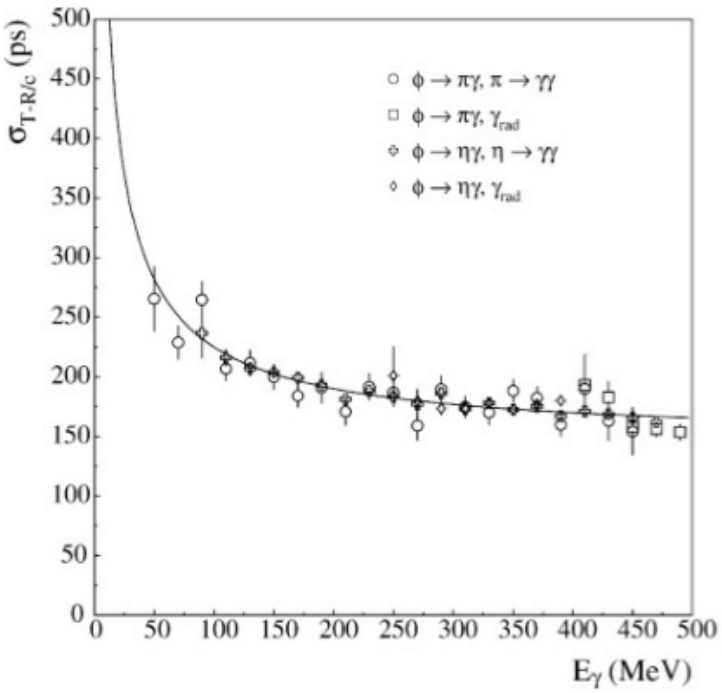

Figure 3.9: KLOE ECAL photon time resolution vs energy with fit result superimposed.

The energy resolution is studied using $e^+e^- \to e^+e^-\gamma$ events.
From the comparison between the reconstructed cluster energies and the e^+e^- momenta the energy resolution and the detector response are obtained, as shown in Fig. 3.10 .
The ECAL response is linear within 2% for $E_\gamma > 75MeV$ with a deviation of 5% at lower energies; the energy resolution is:

$$\frac{\sigma(E)}{E} = \frac{5.7\%}{\sqrt{E(GeV)}} \tag{3.3}$$

The Importance of the ECAL

The ECAL impact on the SAND event reconstruction and background rejection capabilities is important, especially for time resolution, affecting the particle identification capabilities with the ToF technique, and for detection efficiency of low-energy photons and neutrons [57]. The energy resolution appears a less critical parameter, being at the level of some percent for the highest photon and electron energies of few GeVs (with longitudinal leakage that starts becoming important

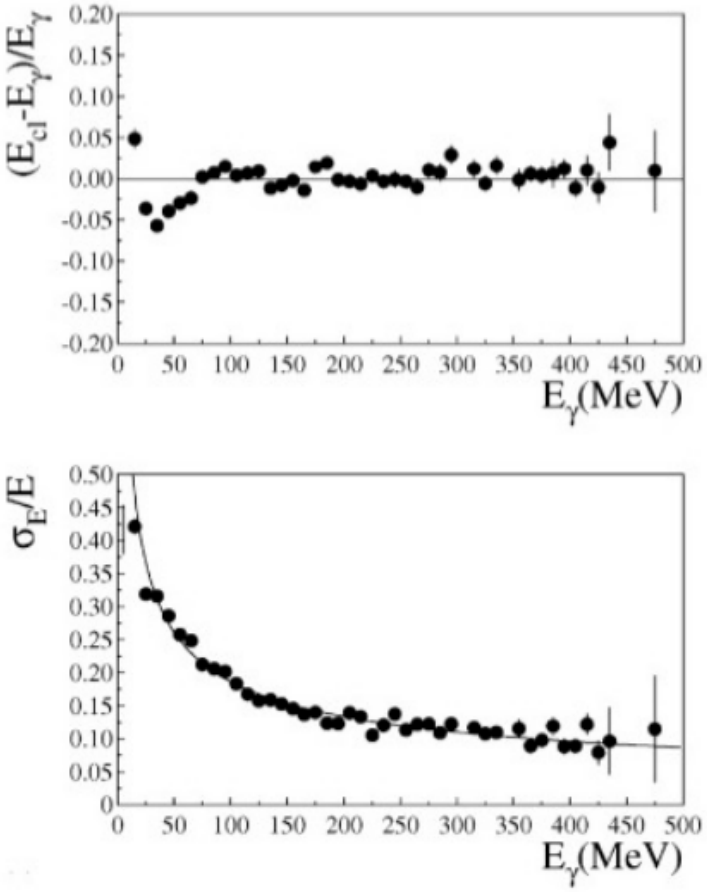

Figure 3.10: KLOE ECAL energy linearity (top) and resolution (bottom) vs energy with fit result superimposed.

for a $15X_0$ thick calorimeter, corresponding to a constant term of $\sim 2\%$), and dominated for hadrons by large fluctuations due to the limited shower containment. These fluctuations can be reduced by adding information on the event from the tracker system and by imposing kinematic constraints, when possible.

3.2.4 The Supeconductive magnet

The KLOE superconductive solenoid magnet and iron yoke were designed to produce 0.6 T axial magnetic field over a cylindrical volume (4.3 m long with a diameter of 4.8 m). The return yoke, which has a mass of 475 tons, contains a cryostat characterized by an outer diameter of 5.76 m, an inner diameter of 4.86 m and an overall length of 4.40 m. The coil is positioned inside the cryostat and it is operated at a nominal current of 2902 A. Thermo-siphoning cycles perform the cooling of the coil: gaseous helium at 5.2 K is injected at 3 bar (absolute pressure) from

the cryogenic plant and liquefied through Joule-Thompson valves into a liquid He reservoir in thermal contact with the coil. Liquid He is used to directly cool the current leads, while gaseous He at 70 K from the cryogenic plant is used to cool the radiation shields.

Chapter 4

Simulation and Reconstruction Algorithms for SAND

The precise characterization of the SAND electromagnetic calorimeter (ECAL) relies on a detailed understanding of its simulation and reconstruction chain. In this chapter, the workflow developed for the study of ECAL performance within the DUNE Near Detector complex is presented. The discussion begins with an overview of the SAND geometry [58] as implemented in the simulation framework, followed by a description of the full simulation chain, from the generation of particles to the detector response. Special emphasis is placed on the truth-matching algorithm, which constitutes a key element of this workflow by establishing a direct connection between Monte Carlo particles and the reconstructed calorimeter clusters.

The methods introduced in this chapter are not only essential for validating the reconstruction algorithms, but also provide the basis for the calibration strategies that will be explored in Chapter 5. In particular, the truth-based studies presented here open the possibility of assessing the calibration potential of different particle samples under realistic conditions. Together, the workflow described in this chapter and the calibration program of the next chapter define the methodology for achieving a precise energy and time reconstruction in the SAND ECAL.

Although the main emphasis is placed on the ECAL, the following sections also include a brief overview of the simulation and reconstruction methods developed for GRAIN and the tracker, in order to place the calorimeter studies in the broader SAND framework.

4.1 SAND geometry

The dunendggd package is a tool developed in order to build proposal geometries for the DUNE ND. It is based on the General Geometry Description (gegede) which is a module that allows to generate the description of constructive geometries in gdml files, with applications in GEANT4 and ROOT. The geometry used in this work of thesis is modeled to reproduce the KLOE yoke, magnet, its electromagnetic calorimeter and the inner tracking system and GRAIN of SAND; in

Fig. 4.1 an overview of the geometry is shown.

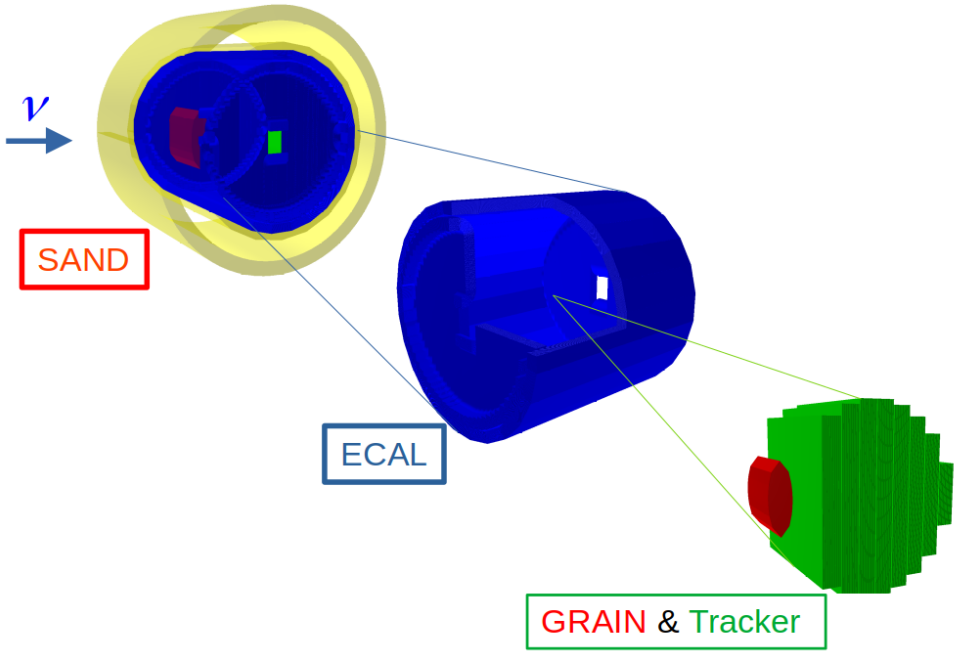

Figure 4.1: Overview of the SAND geometry, in yellow for the outerlayer there is the IronYoke, followed by the superconductive magnet, in blue the ECAL, in red GRAIN and in green the tracker, based on the STT technology in this view.

The coordinates system is chosen such that the center position of SAND is $(x_0, y_0, z_0) = (0.00, -2384.73, 23910.00)$ in mm, the x axis pointing along the cylindrical volume axis, the y axis vertically towards the top of the detector, while the z axis is the horizontal projection of the beam direction. The magnet geometry is represented by an external iron yoke and a copper coil is inserted between the inner and outer aluminium walls of the cryostat. The internal volume of the magnet is a cylinder 4.3 m height with a radius of 2.23 m.

GRAIN Geometry

The outer vessel is modeled as a multi-layered structure of carbon fiber and honeycomb, with a total thickness of 62 mm. The endcaps are represented as 16 mm steel plates. The inner vessel is entirely constructed from aluminum. Both vessels are designed as elliptical modules, with the outer vessel having axes of 192.4 cm and 85.4 cm, and a length of 193.2 cm, while the inner vessel has axes of 23.75 cm and 72.8 cm, with a length of 65 cm.

Tracker Geometry

Currently, two tracker configurations have been simulated: the STT tracker and the drift chamber. A summary of these configurations is provided in table 4.1.

	CH_2/C modules	CH_2 Mass [t]	C Mass [t]	Radiator Mass [t]	Mylar Mass [t]	Gas Mass [t]	Density g/cm^3	Radiation Length [m]
STT	68/2	3.2	0.7	1.3	-	0.1	0.17	2.7
DRIFT	72/2	3.4	0.7	-	0.1	0.1	0.15	3.0

Table 4.1: Main numbers for the two simulated versions of the tracker. The STT-based version does not have clearance between modules.

The basic module of the simulated STT tracker consists of:

- a 5mm tick solid polypropane (CH_2) target slab;
- a polypropylene radiator composed of 105 foils 18 µm thick, alternating with air gaps 117 μm thick;
- four layers of straws arranged in an XXYY pattern, with each straw having a 5 mm diameter, 12μm Maylar walls coated with Al, and 20μm tungsten wire gold coated.

The current simulated design has a total number of 86 modules (about 70 with CH2 target) with a total of 344 straw planes. This configuration foresees about 200×10^3 straws, with an average straw length of about 3.2 m giving a total overall length of 700km.

The base drift module is made of:

- 5 mm (4 mm) solid polypropylene CH_2 (Carbon) target;
- three stations (planes of wires) with alternated signal and field wires spaced along the station by 1 cm. Each station is 1 cm thick and separated from the next one by a 20 μm Mylar plane.

The simulated stations are filled with Ar/CO_2 gas in the proportion 85/15 at 1 atm plus a 10 mbar overpressure and a density 0.002 g/cm^3 . The current design foresees 1 module with carbon target, followed by 9 modules with polypropylene target packed in a unique carbon frame that define a so-called supermodule. The SAND inner volume, in its current simulated design, is filled with eight symmetrical supermodules with respect to the SAND center. All clearances in the SAND inner volume are aligned with the current engineering requirements for the construction.
The simulations presented throughout this thesis use the drift-chamber configuration; however, the analyses discussed rely exclusively on calorimetric information.

Consequently, the results are independent of the tracker technology and can be fully replicated using the STT configuration.

ECAL Geometry

The structure and geometry of ECAL is described in Sec. 3.2.3. In the simulation, the real geometry of ECAL has been implemented, both for the barrel trapezoidal modules and for the endcap C- shaped modules. The structure of scintillating fibers embedded in grooved lead foils has been replaced with alternate planes of lead and plastic scintillator. Each module is constructed as a stack of 209 slabs of 700 μm plastic scintillator interleaved with 400 μm of lead. This structure reproduces the total thickness of 23 cm of the modules, corresponding to 15 X_0. The differences with respect to the real structure have been absorbed in the digitization procedure, described in sec. 4.4 by appropriately setting the number of photo-electrons per unit deposited energy to reproduce the ECAL performance measured in the KLOE experiment (described in 3.2.3).

4.2 Neutrino Event Generation

The GENIE code [59] is a neutrino event generator for the experimental neutrino physics community. It has a focus on low-energies ($\leq$ 1 TeV) and it is currently used by a large number of experiments working in the neutrino oscillation field. The final project goal is the development of a "canonical" neutrino interaction physics MC whose validity extends to all nuclear targets and neutrino flavors from MeV to PeV scales. A GENIE based application to generate neutrino-induced events in the ND has been developed. The first step at the run time is defining the detector geometry from a standard GDML file. The user has the possibility to simulate the neutrino interactions in the whole geometry described in the input file or select a part of the detector as active volume. The detector is aligned such that the beam axis pass through its center. By default, the beam points down by 101 mrad, being this inclination the one needed to get to the FD. The code is able to simulate single or multi-flavor neutrino beams crossing the detector, according to standard DUNE flux. The neutrino energy and type are randomly generated according to the input spectrum file and all neutrinos are simulated with a direction parallel to the beam axis.

4.3 Particle Propagation

After the generation of the neutrino interactions, the primary particles - exiting from the interaction vertex - are propagated in the detector geometry to simu-

late the energy deposition and geometry effects. This step is performed with the Energy Deposition Simulation (EDEP-SIM) software [60] a wrapper around the Geant4 simulation tool. In most cases, it exploits the QGSP_BERT physics list to simulate the possible processes that could happen during the particle propagation. This is the former Geant4 default physics list, and it is recommended for high energy collider and cosmic ray physics, up to 10 TeV. It includes elastic, inelastic, and capture processes for the purely hadronic part, while the electromagnetic processes include Multiple Coulomb Scattering (MCS), Bremsstrahlung and ionization for electrons, muons, pions, kaons and (anti)protons. For the photons, e^+/e^- pair production, Compton and Rayleigh scatterings and photoelectric effect are included. The simulation implements a detailed energy deposition model, the NEST (Noble Element Simulation Technique) model, for both ionizing and non-ionizing (scintillation) energy losses in liquid argon. NEST provides data driven models to compute the scintillation and ionization yield, taking into account the energy and field dependence, as well as the intrinsic fluctuations and recombination physics. There is, however, no treatment of the optical photons propagation. The propagation of optical photons produced in the ECAL scintillation fibers, described in 4.4, and in GRAIN is thus treated separately. Particle propagation is stopped based on configurable energy and time cuts. By default, a lower limit of 1 keV is applied to all particles excluding neutrons, for which the energy cut is instead set to zero. In addition, neutrons have a default time cut of 10 μs. EDEP-SIM supports multiple input options, including the RooTracker format of the Generates Events for Neutrino Interaction Experiments (GENIE) generator and custom particles gun exploiting the Geant4 General Particle Source class. The simulation output is instead provided as simple ROOT files, where information on propagated particle such as the position, momentum, undergoing physics process and corresponding energy losses are stored. Custom configurations options can be provided to tune the output.
The output rootfile has two keys, a TGeomanager (*EDepSimGeometry*) storing the info about the input geometry and a TTree object storing all information about the evolution of all the tracks produced in the events (*EDepSimGeometry*). Both keys are described in more detail in the following. All of the values in the output file are given in CLHEP units, a common system used in HEP application. Table 4.2 shows the list of few basic units as well as some derived ones.

EDEP-SIM Geometry: All the information concerning the geometry used to simulate the particle propagation are stored in a TGeoManager. It contains details of the hierarchical structure of all the volumes composing the geometry, with the upper level volumes being the Near Detector hall and the rock around it. For each one, it also store information about its material, its local transformation (such as

Physical Quantity	CLHEP Unit Name
length	mm
Angle	rad
Time	ns
Energy	MeV
Mass	$6.24 \times 10^{24}\ MeV\ ns^2\ mm^{-2}$
Density	$6.24 \times 10^{24}\ MeV\ ns^2\ mm^{-5}$

Table 4.2: EDEP-SIM units.

position and rotation) and possible overlaps with other volumes.
EDEP-SIM Events: All the information of the propagated particles are stored in this tree exploiting custom I/O classes. The tree contains a single branch, event, which represents a single simulated event. Depending on the generation settings, an event could represent a single particle, an interaction vertex or a complete spill. Independently from the event definition, the data is organized in a hierarchical structure. The data of the event is represented by the main data class **TG4Event** and corresponds to a single entry of the event branch, it contains fields to uniquely identify the event and containers storing the information of each vertex, trajectory and energy deposit in the event. A list of the most important class variables is provided in the following:

- EventId (int), the number of the event;
- RunId (int), the number of the run;
- Primaries, a branch containing the information about the primary particles of the neutrino vertex;
- Trejectories, a branch holding the trajectories of all particles simulated in the event. The class that identifies these objects is the **TG4Trajectory** class with several variables identify the detail of the trajectory object such as:
  - TrackId and ParentId (int), to identify the id of the particle and the id of its parent;
  - PDGCode, to identify the type of particle producing the track;
  - InitialMomentum (TLorentzVector) a vector that identifies the initial position and energy of the particle;
  - TrajectoryPoints, the set of points produced along the track, containing all information about time position and energy deposited;

- SegmentDetectors, a branch containing a map between the hits occurred in the event and the sensitive detector sections in which they are recorded.

4.4 Detector responses

The detector response, i.e. the digital signals that would be obtained by the DAQ system, is simulated by the digitization algorithms which convert the particles energy deposition (edepsim hits) in the detectror sensible volumes into digital information.

4.4.1 GRAIN response simulation

As introduced in sec. 4.3, particle propagation does not include the propagation of optical photons. Thus for GRAIN a dedicated Geant4 simulation is implemented to correctly simulate the emission and propagation of the liquid argon scintillation light. The steps for the GRAIN simulation are described in the following:
Scintillation light simulation: The emission of scintillation light follows the particle propagation step, using EDEP-SIM energy deposits with a light yield of $4 \cdot 10^4$ photons/MeV and a scintillation decay time fixed at 7 ns.
Photon Generation: The total number of photons emitted is computed taking into account both the nominal light yield of liquid argon in absence of electrial fields and the secondary energy deposition obtained from EDEP-SIM. For each energy deposit the number of photons is extracted from a gaussian distribution with mean N equal to the deposited energy times the argon light yield and standard deviation $\sigma \propto \sqrt{N}$. The position and time are extracted randomly between the start and the end point of the deposit. The wavelength is extracted randomly from a probability distribution parametraized from the measurement reported in [61] of the emitted photons obtained from the simulation.
Photon Propagation: The emitted light is then propagated through the argon volume taking in account the different physical phenomenon that could affect propagation such as impurities and Rayleigh scattering. On top of these effects optical photons can be absorbed by the surfaces inside the inner vessel, this phenomenon is taken into account thanks to Geant4 models that simulates this behaviour such as the *glisur* model with the *dielectric_dielectric* type. **Photon Collection** The sensor volumes of the GRAIN geometry collect the propagating photons, storing information of each optical photons that are also the output of the simulation. The most crucial information collected by the sensors are:

- detection position on the sensor: the xy local coordinate of the photon interaction point, used to compute on which pixel the photon was collected;

- detection time: The time of arrival of the photon on the sensor with respect to the neutrino interaction vertex time.

4.4.2 Tracker response simulation

The tracker readout is simulated with an algorithm that converts each energy deposition occurring in the tracker's gas, into an ADC/TDC signal. For each energy deposition (EDEP-SIM hit) the closest wire to the segment is found and its TDC value calculated as:

$$t = T_{hit} + T_{drift} + T_{wire} \tag{4.1}$$

in which T_{hit} represents the time at which the particles generated the hit, T_{drift} is the drift time calculated assuming a drift velocity of 0.05 mm/ns, and T_{wire} is the signal propagation time in the wire assuming a velocity of 200 mm/ns. The measured TDC for a given wire is the shortest among the times in 4.1. The process is illustrated in Fig. 4.2

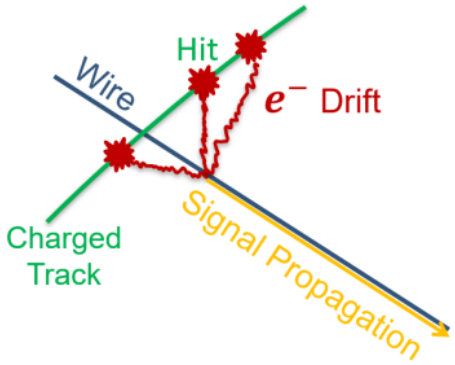

Figure 4.2: Illustration of crossing charged particle that produce ionization around the wire. Electrons drift toward the wire and produce a signal recorded as a TDC.

4.4.3 ECAL digitization

The ECAL simulation chain starts from the simulation of the digitized signals acquired by the photo-detectors. The digitization step consists of a C++ code integrated in the SAND reconstruction framework [62] which takes as input the EDEP-SIM ROOT TTree output, see Sec. 4.3, converting it into digitized signals, stored in a ROOT TTree structure that will be used for subsequent event reconstruction. The ECAL digitization reproduces the calorimeter segmentation, the light production, the signal formation on the photo-sensors and its digitization. In order to reproduce the ECAL readout configuration, each of the 24 barrel

modules is segmented in depth in 5 layers, each divided in 12 cells; the 32 modules of each endcap are segmented in depth in 5 layers; they are subdivided in 6 cells for module 1-2 and 17-18, 3 cells for module #3-12 and #19-28 and 2 cells for module #13-16 and #29-32. Each barrel cell is uniquely distinguished by an identifier characterized by

- **detector_id** $\times 10^7$: fixed value = 2, selects the ECAL barrel.
- **module_key** $\times 10^3$: allowed values 0–23, identifies one of the 24 trapezoidal modules.
- **layer_id** $\times 10^2$: allowed values 0–4, corresponds to the sampling layers.
- **cell_local_id** $\times 10$: allowed values 0–11, scintillator bar column inside the layer.

A Schematic representation of the barrel module segmentation is reported in Fig. 4.3

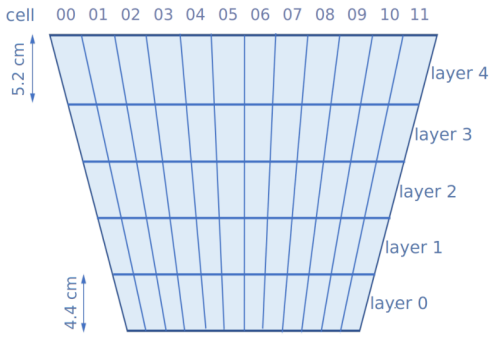

Figure 4.3: Schematic representation of one barrel module segmentation in the yz plane view.

For the endcaps the cell encoding is different and is defined as follows:

- **detector_id** $\times 10^7$: allowed values 0 (-X) / 1 (+X), selects the endcap side.
- **module_key** $\times 10^3$: "C" shaped module key:
  - **module_id** $\times 10^2$ **of key**: allowed values 0–15, physical module.
  - **replica_id** $\times 10^1$ **of key**: allowed values 0 / 1, where 0 = right half and 1 = left half.
- **layer_id** $\times 10^2$: allowed values 0–4, corresponds to the sampling layers (inner to outer).

- **cell_local_id** $\times 10^0$: allowed values 0–5 / 0–2 / 0–1, number of columns (depending on module geometry).

The encoding and decoding of cell identifiers is performed by the `SANDGeoManager` [62] tool, provided as part of the SAND reconstruction framework. This tool encapsulates the complete detector geometry and centralizes all geometry-related functionalities, from encoding/decoding cell IDs to checking hit containment within cells and more, thereby supporting both the detector response simulation and the reconstruction algorithms.

The light produced in the fibers of each cell is read out on both module sides by PMTs. In order to simulate the number of photo-electrons produced on the photo-detectors by each EDEP-SIM hit, the digitization algorithm analyzes the information about the hits produced in the ECAL active layers in the simulation. The deposited energy dE of the hit is retrieved and associated with the corresponding cell position of the crossing particle. The number of photo-electrons N_{pe} is then extracted from A Poisson distribution with mean value μ_{pe} given by:

$$\mu_{pe} = dEAE_{pe} \tag{4.2}$$

in which A is the light attenuation factor in the fiber and E_{pe} is the conversion factor of energy into the number of photo-electrons (pe) equal to 18.5 to have an average number of 40 pe for minimum ionizing particle (MIP) crossing in the middle of the barrel module [56].
The attenuation factor is defined as:

$$A_{1,2} = p_1 e^{-\frac{d_{1,2}}{L_1}} + (1 - p_1) e^{-\frac{d_{1,2}}{L_2}} \tag{4.3}$$

in which -from previous studies at KLOE- $p_1 = 0.35$, L_1 is 50 cm and L_2 depends on the layer number l, and is 430 cm for $l = 0, 1$, 380 cm for $l = 2$ and 330 cm for $l = 3, 4$. In Eq. 4.3 $d_{1,2}$ are the distances from the hit to the two PMT photocathodes. The path lengths are evaluated by `SANDGeoManager`, differentiating between barrel and endcap modules.

For the **barrel**, the hit position (h_x, h_y, h_z) is transformed into local coordinates of the layer in order to evaluate the distances from the PMTs d_1 and d_2.

For the **endcaps**, the hit is checked to belong to the chosen module and transformed to the local coordinates. Different geometrical regions of are treated separately:

- **Vertical section (`vert`)** - The distance is calculated along the vertical axis

and corrected for the curvature at a given depth.

- **Horizontal sections (`hor`)** - The distance is measured from the module center toward each side.
- **Curved section (`curv`)** - The path is computed along the local arc defined by the module curvature.

In each case, the total distance along the scintillator cell is obtained by combining the local geometrical contribution with the nominal cell length.

The number of ADC counts of the digitized signal $S^{1,2}$ of the two sides of the modules is given by the following equation:

$$S^{1,2} = N_{pe} ADC_{pe} \tag{4.4}$$

in which the factor $ADC_{pe} = 4$ is the conversion factor between the number of photon electrons N_{pe} and the adc counts.
The arrival time of the photon at the photosensor is simulated according the following equation:

$$t_{pe} = t_{cross} + t_{decay} + \frac{d_{1,2}}{v_{vlfb}} + Gauss(1 \text{ ns}) \tag{4.5}$$

in which t_{cross} is the time associated to the particle crossing the cell, t_{decay} is the scintillation decay time, $d_{1,2}/v_{vlfb}$ is the time of the signal propagation through the scintillating fibers of the cell (with $v_{lfb} = 17$ cm/ns), and $Gauss(1 \text{ ns})$ is a Gaussian smearing to simulate the PMT response time uncertainty, including its transit time spread. The value of t_{decay} is obtained with an acceptance–rejection algorithm that reproduces the scintillation time profile. A candidate time t' is first sampled from an exponential distribution with decay constant $\tau_d = 3$ ns,

$$t' = -\tau_d \ln(1 - U_1), \qquad U_1 \sim \mathcal{U}(0, 1),$$

and is then accepted with probability $1 - e^{-t'/\tau_r}$, where $\tau_r = 0.7$ ns is the scintillation rise time. The analytical function for the probability density function is as follows:

$$f(t) \;=\; \frac{\tau_d + \tau_r}{\tau_d^2} \left(e^{-t/\tau_d} - e^{-t\left(\frac{1}{\tau_d} + \frac{1}{\tau_r}\right)} \right), \qquad t \geq 0, \tag{4.6}$$

In Fig.4.4 the photon emission time distribution is presented with a small Monte Carlo sample, normalized, and Eq. 4.6 superimposed. This procedure guarantees a time distribution as expected.
Finally, the TDC value is set to the simulated photo-electron time, provided it falls

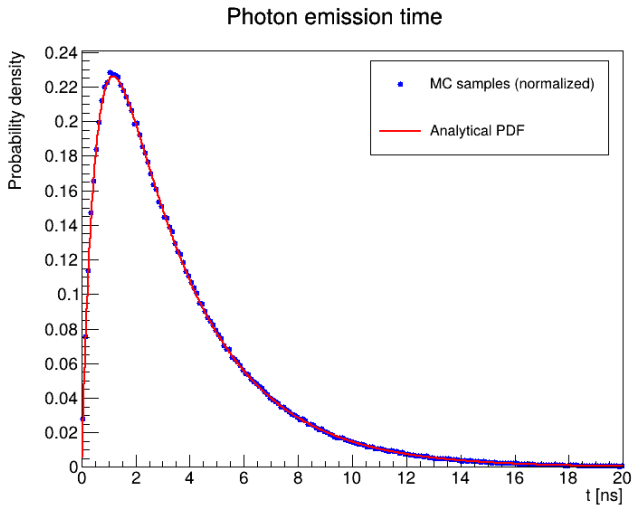

Figure 4.4: Photon emission time distribution in the simulation, with Eq.4.6 superimposed.

within the PMT integration window of 50 ns, which corresponds to the constant-fraction threshold at 15% of the total photo-electrons forming the signal [63].
The output of the ECAL digitization, representing the digitized signal, consists of a digitized cell object, organized in a `TTree` ROOT structure. For each digitized cell, the following quantities are defined:

- the cell identifier;
- the position coordinates of the cell center;
- the length of the cell;
- the distinct labels of the module, layer and cell;
- the two sets of signal, $ps1$ and $ps2$, recorded by the two photo-sensors on both sides.

The signals are characterized by:

- the side in which the signal is produced;
- the ADC value;
- the TDC value;
- the collection of the pe, defined by their arrival time and index of the EDEPSIM hit.

4.5 Reconstruction

The reconstruction algorithms process the digitized detector signals in order to identify and characterize the physical observables of an event. Their goal is to transform low-level information such as ADC and TDC counts into higher-level objects, including clusters, tracks, and vertices. These reconstructed quantities provide the essential link between the simulated detector response and the underlying particle kinematics, forming the basis for physics analyses. In this section, the reconstruction algorithms in the SAND software framework [62] are presented, with particular emphasis on the ECAL reconstruction.

4.5.1 GRAIN Reconstruction

The output of GRAIN consists of a set of two-dimensional images acquired by its optical cameras.

General strategy. The reconstruction algorithm is designed to combine the information from all cameras under the assumption that each event corresponds to a single neutrino interaction. It proceeds in two main steps:

1. **2D analysis:** identification and fitting of track projections in each image.
2. **3D reconstruction:** back-projection of the fitted clusters into 3D space using a camera model, and combination of the views to obtain vertices and track trajectories.

Two-dimensional reconstruction. Each image is analyzed independently to detect tracks and possible vertex candidates. The workflow is:

- **Image preselection:** discard empty or saturated views (less than 3% or more than 60% active pixels).
- **Line detection:** apply the Hough transform to map track candidates into a parameter space.
- **Feature extraction:** locate line parameters by searching for local maxima in Hough space. Multi-Otsu thresholding is used to separate pixel classes by intensity.
- **Clustering:** surviving pixels above threshold are grouped using a density-based algorithm.

The output of this step is a set of 2D clusters with best-fit lines, as well as possible intersection points that serve as candidate vertices.

Three-dimensional reconstruction. The 3D step aims to recover the vertex and track directions in liquid argon by combining multiple views. Two methods are currently implemented:

- **Voxelization method:** The GRAIN volume is divided into voxels (1 cm^3 in the current implementation). Each voxel is projected onto the camera images; if its projection falls within a 2D cluster, its counter is incremented. After looping over all voxels, only those consistent with projections in a sufficient number of cameras (threshold chosen by the multi-Otsu method) are retained. The surviving voxels form a 3D cloud representing each track. Fitting these volumes yields the track directions.
- **Multiple-View Geometry:** Based on projective geometry, this method triangulates 3D points from their image correspondences across multiple calibrated cameras. The system is described by projection matrices $P_i = K_i[R_i|t_i]$, where K_i encodes intrinsic parameters and R_i, t_i define orientation and position. This approach requires precise camera calibration and is still under development.

The GRAIN reconstruction algorithms are still preliminary and require further optimization and validation. Nonetheless, the combination of central projection encoding, 2D clustering with Hough-based line finding, and multi-view 3D reconstruction demonstrates the feasibility of extracting interaction vertices and track directions from the optical readout.

4.5.2 Tracker Reconstruction

Charged-particle tracks in the SAND tracker are reconstructed using a two-step approach. A fast helix fit provides an initial estimate of the track parameters, which is then refined through an Extended Kalman Filter (EKF) that accounts for magnetic bending, energy loss and multiple scattering.

Helix fast fit. The tracker is immersed in a uniform magnetic field of $B \simeq 0.6$ T directed along the x-axis, resulting in helical trajectories in the y-z plane. A schematic y-z projection of the trajectory is shown in Fig. 4.5.

Each fired wire provides a time measurement

$$t_{\text{measured}} = t_0 + t_{\text{tof}} + t_{\text{drift}} + t_{\text{signal}}, \tag{4.7}$$

where t_0 is a trigger offset, t_{tof} is the particle time-of-flight, t_{drift} the drift time of the ionization electrons ($v_{\text{drift}} \simeq 0.05$ mm/ns), and t_{signal} the signal propagation time along the wire ($v_{\text{signal}} \simeq 200$ mm/ns). From these inputs, the drift

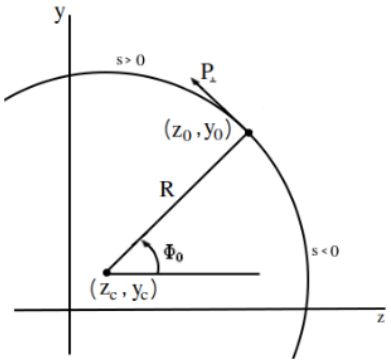

Figure 4.5: Schematic view of a charged-particle trajectory in the y–z projection for a uniform magnetic field parallel to the x axis (example shown for $h = +1$).

distance r_{obs} is reconstructed. The helix parameters are obtained by minimizing the likelihood function

$$\chi^2 = \sum_i \frac{\left(r_i^{\text{obs}} - r_i^{\text{est}}\right)^2}{\sigma^2}, \tag{4.8}$$

where r_i^{est} is the distance of closest approach between the helix model and the i-th wire, and $\sigma \simeq 200$ μm is the detector spatial resolution. This fast fit provides a robust first guess for the track parameters.

Extended Kalman Filter. The helix parameters from the fast fit are refined through an EKF, which propagates the track state vector step-by-step between measurement planes. The state vector is defined as

$$a_k = \left(x, \quad y, \quad 1/\tilde{R}, \quad \tan\lambda, \quad \phi\right), \tag{4.9}$$

where $\tilde{R}$ is the signed helix radius, λ is the dip angle, and ϕ the azimuthal coordinate used as running parameter to avoid ambiguities for looping tracks. The propagation accounts for deterministic energy loss, evaluated with the Bethe–Bloch formula, by updating the curvature term $1/\tilde{R}$ at each step. Stochastic effects from Multiple Coulomb Scattering (MCS) are included via a process noise covariance matrix, with the scattering angle variance

$$\theta_{\text{MS}} = \frac{13.6 \text{ MeV}}{\beta pc}\sqrt{\frac{\ell}{X_0}}\left[1 + 0.038 \ln\left(\frac{\ell}{X_0}\right)\right], \tag{4.10}$$

where ℓ is the thickness of traversed material and X_0 its radiation length.

The measurement model relates the state vector to the hit coordinates and in-

cidence angles at each wire layer, with measurement uncertainties described by a covariance matrix V_k that reflects the tracker resolutions ($\sigma_x \simeq 200$ μm, $\sigma_\theta \simeq 0.2$ rad). Through the recursive EKF update, track parameters are refined by optimally combining the helix propagation with the measured hits.

This strategy ensures accurate reconstruction of charged particle trajectories in the SAND tracker, where both magnetic bending and material effects play a significant role. The method provides the necessary precision for downstream event reconstruction and physics analyses.

4.5.3 ECAL Reconstruction

Particle reconstruction in the ECAL consists of a clustering algorithm developed in C++ and integrated in the ECAL reconstruction framework. Clustering takes as input the ROOT file provided by the digitization step (Sec.4.4.3), composed of a TTree structure of the digitized cells. The first step of the clustering algorithm is to classify digitized cells into *complete* and *incomplete* according to whether a signal is found at both sides of the cell in a finite time interval. For a given cell of geometric length L , we define a matching time window

$$\Delta t_{\max} \;=\; L/v_{\text{lfb}}, \tag{4.11}$$

Two signals with TDC $t_1 \in$ `ps1` and $t_2 \in$ `ps2` (defined in section 4.4.3) are considered together *match* if

$$\left| t_1 - t_2 \right| < \Delta t_{\max} \tag{4.12}$$

For each digitized cell in the event:

1. Loop over signals ps_1 on one side of the cell and search for a signal ps_2 on the opposide side that satisfies Eq. (4.12). To prevent double assignment in multi-hit situations, each hit can be used at most once.

2. If a ps_1 photo signal has no partner in the opposide side, create an *incomplete* cell carrying only that single-ended signal.

3. After processing all ps_1 signals, similarly a scan on all ps_2 signals and other possible incomplete cells are identified.

The step returns two containers:

- **Complete cells**: each contains exactly one time-coincident pair (ps_1, ps_2) matched within $\Delta t_{\max}$.

- **Incomplete cells**: each contains exactly one single-ended signal (ps_1 *or* ps_2) that could not be paired within the allowed time window.

The windows $\Delta t_{\max}$ scales with the cell length and the effective light velocity in the fibers, to take into account the end-to-end propagation differences among cells.

After signal pairing, *complete* ECAL cells are grouped into *pre-clusters* based on geometric adjacency criterion. A pre-cluster is defined as a set of complete cells that are connected through a nearest-neighbour relation, separately barrel and endcap regions.
For cells in the **endcap**, adjacency is tested in the (x, z) plane; for the **barrel**, in the (y, z) plane. Two cells c and c' are neighbours if the Euclidean distance in the corresponding plane is below a region-specific threshold:

$$\text{endcap:} \quad d_{\text{endcap}}(c, c') = \sqrt{(x - x')^2 + (z - z')^2} < d^{\max}_{\text{endcap}}\,, \tag{4.13}$$

$$\text{barrel:} \quad d_{\text{barrel}}(c, c') = \sqrt{(y - y')^2 + (z - z')^2} < d^{\max}_{\text{barrel}}\,, \tag{4.14}$$

with numerical values

$$d^{\max}_{\text{endcap}} = 65.70 \text{ mm}, \qquad d^{\max}_{\text{barrel}} = 72.36 \text{ mm},$$

These thresholds correspond to the maximum centre-to-centre spacing of adjacent cells, including inter-layer diagonals (e.g. layers 4–5).

For each pre-cluster the next step is to instantiate a `cluster` object that aggregates (i) the list of reconstructed cell objects and (ii) the cluster observables (position, time, energy and spatial spreads). At this step only *complete* cells contribute to the cluster. For each *complete* cell in the pre-cluster, the distance between the particle hit and the two PMTs, d_1 and d_2 can be inferred from the TDC time difference between the two readout ends as follows:

$$d_1 = \frac{1}{2}\left(L + (t_1 - t_2)v_{\text{lfb}}\right),\; d_2 = \frac{1}{2}\left(L - (t_1 - t_2)v_{\text{lfb}}\right). \tag{4.15}$$

Then the cell energy and time can be reconstructed from the values of the ADCs and TDCs. For each PMT end (A, B) of cell i, the reconstructed energy is

$$E_i^{A,B}\,[\text{MeV}] = \frac{(Q_i^{A,B} - P_i^{A,B})\,[\text{counts}]}{C_i^{A,B}\,[\text{counts/MiP}]}\; K\; f_{\text{MiP}\to\text{MeV}}\,[\text{MeV/MiP}]\,. \tag{4.16}$$

Here $Q_i^{A,B}$ are the integrated charges (ADC counts), $P_i^{A,B}$ the pedestals (counts), $C_i^{A,B}$ the MiP calibration constants (counts/MiP), K the global energy scale fac-

tor, and $f_{\mathrm{MiP}\to\mathrm{MeV}}$ the MiP-to-MeV factor (MeV/MiP).

The cell energy is then

$$E_{\mathrm{cell}} = \frac{1}{2}\left(\frac{E_i^A}{A_1} + \frac{E_i^B}{A_2}\right). \tag{4.17}$$

in which $A_{1,2}$ are defined as in 4.3.

For the simulation (no pedestals, equal end gains and light yield) we set $P_i^{A,B} = 0$ and identify $\mathrm{adc}_{1,2} \equiv Q_i^{A,B}$. Using

$$\frac{K\, f_{\mathrm{MiP}\to\mathrm{MeV}}}{C_i^{A,B}} \;=\; \frac{1}{\texttt{attpassratio}\,\texttt{pe2ADC}^{A,B}\,\texttt{e2pe}}\,,$$

where `attpassratio` is the dimensionless visible-to-deposited energy ratio $E_{\mathrm{vis}}/E_{\mathrm{dep,tot}}$ (19% for E.M. showers, 16% for MIPs in this work) , $\texttt{pe2ADC}^{A,B} = 18.5$ are the end gains (counts/p.e.) corresponding to a mean number of 40 p.e. for a minimum ionizing particle crossing in the middle of the barrel module, and `e2pe = 1/0.25` is the light yield (p.e./MeV), and taking $\texttt{pe2ADC}^{A} = \texttt{pe2ADC}^{B} \equiv \texttt{pe2ADC}$, the equivalent working expression is

$$E_{\mathrm{cell}} = \frac{\dfrac{\mathrm{adc}_1}{A_1} + \dfrac{\mathrm{adc}_2}{A_2}}{2\,\texttt{attpassratio}\,\texttt{pe2ADC}\,\texttt{e2pe}}\,. \tag{4.18}$$

Here $\mathrm{adc}_{1,2}$ are the measured amplitudes (counts) at the two ends in simulation.

The corresponding time is

$$T_{\mathrm{cell}} = \tfrac{1}{2}\left(\mathrm{tdc}_A + \mathrm{tdc}_B - \frac{L}{v_{\mathrm{lfb}}}\right), \tag{4.19}$$

In which the calibration offset of the two PMTs are set to 0.

Finally for each cell of the pre-cluster the reconstructed position are calculated. For cells that are in the barrel modules, the reconstructed position in the yz plane is given by the center position of the cell in the geometry, meanwhile the longitudinal position of the hit along the scintillator bar is obtained from the two-ended time measurement. From the difference between the arrival times at the two readout ends, the corresponding propagation distance from one end, d_1 from Eq. 4.15, is computed. Starting from the nominal barycentre of the cell in the detector global coordinates, the point is first mapped into the barrel's local reference frame, in which the bar axis coincides with the local y direction. The hit position is then shifted along this axis by the distance d_1, corresponding to the measured propagation path of the scintillation light. The modified local coordinates are

finally transformed back to the global frame, providing the reconstructed spatial position of the energy deposit.

For the endcap modules, the reconstruction follows the same principle but must account for their curved geometry. Each endcap cell follows a predefined reference path composed of one or two horizontal sections (depending on the module), two curved arcs, and a vertical section connecting them. The total length of this path defines the effective cell length. Using the distance d_1 derived from the time difference, the algorithm determines where along this path the hit is located by comparing d_1 with the cumulative lengths of the individual sections. Within straight regions, the position is computed by translating the hit along the section axis by the corresponding distance. Within curved regions, the position is evaluated along the arc using the appropriate angular displacement defined by the local radius of curvature. This method provides a continuous and geometrically consistent description of the hit location along the full cell, including the transition between straight and curved parts. The resulting local coordinates are finally converted back to the global reference frame using the module's transformation matrix.

The reconstructed variable from each digitized cell is used to create a *reconstructed cell* object that contains the information from the digitized cell and the reconstructed variables in energy, time and position.

From the reconstructed variables of the cells we evaluate the cluster observable quantities as follows: let the reconstructed cells be indexed by i, with energies E_i, times T_i and positions (x_i, y_i, z_i). Define the total and quadratic energy sums

$$E_{\text{tot}} = \sum_i E_i, \qquad E_{\text{tot}}^{(2)} = \sum_i E_i^2,$$

and the energy-weighted centroids

$$\bar{x} = \frac{1}{E_{\text{tot}}} \sum_i E_i x_i, \quad \bar{y} = \frac{1}{E_{\text{tot}}} \sum_i E_i y_i, \quad \bar{z} = \frac{1}{E_{\text{tot}}} \sum_i E_i z_i, \quad \bar{T} = \frac{1}{E_{\text{tot}}} \sum_i E_i T_i. \tag{4.20}$$

To characterise the intra-cluster cluster size, we compute energy-weighted second moments and derive unbiased RMS estimates using the *effective* number of measurements

$$n_{\text{eff}} = \frac{E_{\text{tot}}^2}{E_{\text{tot}}^{(2)}}, \qquad c = \begin{cases} \dfrac{n_{\text{eff}}}{n_{\text{eff}} - 1}, & n_{\text{eff}} > 1, \\ 1, & \text{otherwise}, \end{cases}$$

$$\sigma_x = \sqrt{c\left(\frac{1}{E_{\text{tot}}}\sum_i E_i x_i^2 - \bar{x}^2\right)}, \quad \sigma_y = \sqrt{c\left(\frac{1}{E_{\text{tot}}}\sum_i E_i y_i^2 - \bar{y}^2\right)}, \tag{4.21}$$

$$\sigma_z = \sqrt{c\left(\frac{1}{E_{\text{tot}}}\sum_i E_i z_i^2 - \bar{z}^2\right)}. \tag{4.22}$$

To remove accidental overlaps grouped during pre-clustering, each pre-cluster is tested for internal time spread and, if needed, split. For the two readout ends (A, B) we define the energy-weighted mean time and RMS:

$$E_{\text{tot}}^{A,B} = \sum_{i=1}^{N} E_i^{A,B}, \qquad \bar{t}^{A,B} = \frac{1}{E_{\text{tot}}^{A,B}}\sum_{i=1}^{N} E_i^{A,B}\, t_i, \tag{4.23}$$

$$\sigma_t^{A,B} = \sqrt{\frac{1}{E_{\text{tot}}^{A,B}}\sum_{i=1}^{N} E_i^{A,B}\, t_i^2 - \left(\bar{t}^{A,B}\right)^2}. \tag{4.24}$$

If the pre-cluster satisfies the splitting condition

$$\sqrt{(\sigma_t^A)^2 + (\sigma_t^B)^2} \;>\; 5 \text{ ns}, \tag{4.25}$$

it is partitioned into up to four sub-groups (new clusters) according to the signs of the cell times at both ends $\left(t^A,\, t^B\right)$ with respect to the cluster time:
$(+,+),\ (+,-),\ (-,+),\ (-,-)$. After each split, the pre-cluster observables are recomputed on the resulting groups and the test in Eq. (4.25) is repeated until no group qualifies for further splitting.

To reunite clusters that are not strictly adjacent, a merging step is applied. Two clusters are merged if their energy-weighted centroids are within $d_{\text{space}} < 25$ cm and their energy-weighted mean times differ by less than $|\Delta\bar{t}| < 2.5$ ns. When a merge occurs, the cluster parameters (energy sums, centroids, time moments, lists of cells) are updated for the union.

For the final clusters, a straight-line axis and an apex are estimated. For each module layer ℓ crossed by the cluster, the energy-weighted position is computed as

$$\boldsymbol{r}_\ell \;=\; \frac{\sum_{i\in\ell} E_i\, \boldsymbol{r}_i}{\sum_{i\in\ell} E_i}, \tag{4.26}$$

and a linear regression over the set $\{\boldsymbol{r}_\ell\}$ yields the cluster direction $\hat{\boldsymbol{u}}$ and apex $\boldsymbol{r}_0$ (e.g. the best-fit line $\boldsymbol{r}(s) = \boldsymbol{r}_0 + s\,\hat{\boldsymbol{u}}$).

To improve the energy estimate and completeness of clusters, a recovery pass is

applied to *incomplete* cells (single-ended signals). An incomplete cell is first assigned to a cluster if it has at least one geometric neighbour inside that cluster. If no neighbour is found, the cell is matched by angular proximity to the nearest cluster centroid, using the global detector frame of reference. The angular matching criteria used to attach incomplete cells are defined in the SAND reference frame shown in Fig. 4.6: for barrel cells the comparison is performed in the (y, z) plane using $\phi = \text{atan2}(z, y)$, while for endcaps it is performed in the (x, y) plane using $\theta = \text{atan2}(y, x)$.

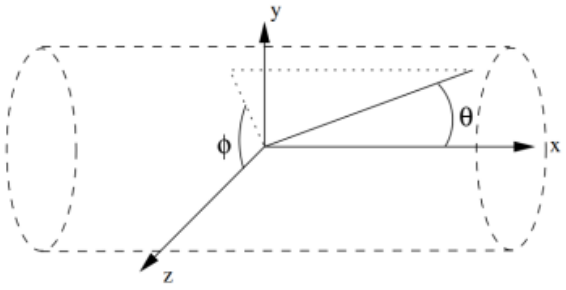

Figure 4.6: SAND reference frame (origin at detector center) and definition of the angular coordinates used in the recovery step: ϕ is evaluated in the (y, z) plane (barrel) and θ in the (x, y) plane (endcaps).

Barrel (selection in the z–y plane). Let $\boldsymbol{r}_u = (x_u, y_u, z_u)$ be the incomplete cell position and $\boldsymbol{r}_c = (x_c, y_c, z_c)$ the energy-weighted centroid of a candidate cluster. Define the barrel angles

$$\phi_u \;=\; \text{atan2}(z_u,\, y_u), \qquad \phi_c \;=\; \text{atan2}(z_c,\, y_c), \tag{4.27}$$

and the minimal wrapped difference

$$\Delta\phi \;=\; \text{atan2}\big(\sin(\phi_u - \phi_c),\, \cos(\phi_u - \phi_c)\big). \tag{4.28}$$

The cell is attached to the cluster if $|\Delta\phi| < \tau$ with $\tau = 3^\circ$ ($\simeq \pi/60$).

Endcaps (selection in the x–y plane). With the same notation, define

$$\theta_u \;=\; \text{atan2}(y_u,\, x_u), \qquad \theta_c \;=\; \text{atan2}(y_c,\, x_c), \tag{4.29}$$

and

$$\Delta\theta \;=\; \text{atan2}\big(\sin(\theta_u - \theta_c),\, \cos(\theta_u - \theta_c)\big). \tag{4.30}$$

The cell is attached to the cluster if $|\Delta\theta| < \tau$ with $\tau = 3°$. If multiple clusters satisfy the angular criterion, the one with the smallest $|\Delta\phi|$ (barrel) or $|\Delta\theta|$ (endcap) is chosen. Upon assignment, the cluster observables (energy sum, energy-weighted centroid, time, and spreads) are recomputed to include the recovered cell.

As output, the algorithm writes its results to a ROOT file as a `TTree` (hereafter `tCluster`). Each tree entry corresponds to a single event and stores a `vector<cluster>` containing all reconstructed objects. For every cluster, the tree records the high-level observables (total energy, energy-weighted time, centroid coordinates, and spatial spreads) together with the list of constituent `reco_cells`, which retain per-cell quantities (energy, time, reconstructed position, and paired signals). This layout enables event-wise iteration while providing direct access to both cluster-level summaries and underlying cell-level detail. A visual representation of the clustering output is presented in Fig. 4.7

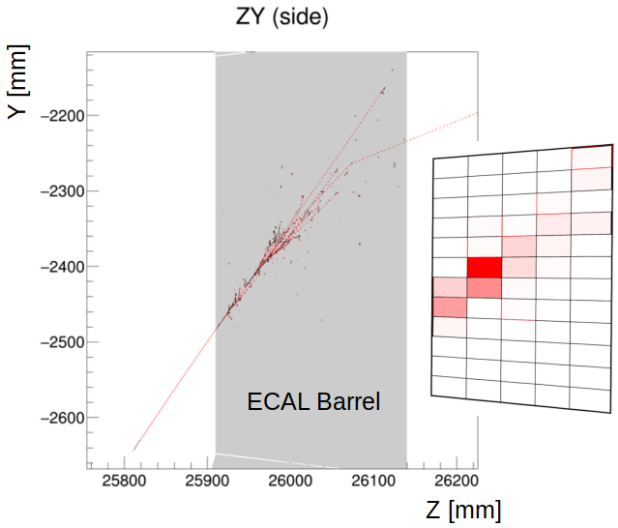

Figure 4.7: Visual representation of a cluster. On the left, the Monte Carlo event display shows an ECAL barrel module (in gray) with Monte Carlo tracks from a simulated electron. On the right, a schematic view of the barrel cell division is shown, where the colored cells correspond to those fired in the cluster. The red gradient indicates the deposited energy in each cell.

4.6 ECAL Truth matching and Reconstruction Validation

Validation of the ECAL reconstruction is performed by comparing cluster observables with Monte Carlo (MC) truth defined at the level of the *generator(s)* of the cluster. A generator is an ancestor particle that initiates energy deposition in the cluster (e.g. the primary electron that starts an electromagnetic shower), as opposed to its secondaries that directly deposit energy. In general, a cluster can have more than one generator (for instance, overlapping showers), so the matching returns a *list* of generators contributing to the cluster.

The truth-matching algorithm [64] traverses the MC trajectory graph and builds a candidate set $\mathcal{G} = \{g_k\}$ for each reconstructed cluster. For every candidate g it defines the family $F(g)$ as the particle and all its descendants, and computes the truth energy attributed to the cluster avoiding double counting across parent/child chains. If two candidates are in a parent-child relation, the parent is retained and the child is discarded, with the parent's E_{true} including the child's contribution. The surviving generators are ranked by E_{true} and stored as an ordered list (with identifiers and truth sums) associated to the cluster.

From the selected generator list we derive the truth quantities used for validation: either per-generator (e.g. using the top-ranked generator) or aggregated over the returned set, enabling one-to-one comparisons with the reconstructed cluster energy, position, and timing. This section details the matching strategy and presents the resulting validation performance.

4.6.1 Truth Matching algorithm

The truth-matching algorithm, developed in $C++$ takes as input the ROOT outputs produced by the EDepSim simulation (Sec. 4.3) and by the ECAL reconstruction algorithm (Sec. 4.5.3). In both files, one `TTree` entry corresponds to one event. Events between the two files are paired *event-by-event* by entry-index alignment.

For each matched event, the algorithm reads the MC truth and, through an external software tool (a dedicated EDepSim wrapper [65]), creates a tree structure with parent-child relationships among all trajectories in the event, storing information on their hits (energy deposits) and the trajectory points that form the particle path in the simulation. Exploiting the hit identifier stored in the photoelectron (pe) objects within the signals of the reconstructed cells, each pe can be traced back to the MC trajectory that produced it. For a given reconstructed cluster,

the set of *generator candidates* is therefore built as the union of all trajectories referenced by the pe observed in its cells.

Generator identification from trajectory-point crossings. Building on the candidate set defined above, a candidate track is promoted to *generator* if its Monte Carlo trajectory *enters* the cluster, i.e. to cross from outside to inside one of the cluster's reconstructed ECAL cells. For a candidate with ordered trajectory points $\{\mathbf{r}_k\}_{k=0}^{n}$ (sorted by increasing time) and for the cluster cell set $\mathcal{C}$, let cell($\mathbf{r}$) return the ECAL cell containing $\mathbf{r}$ (or $\varnothing$ if none), and define $\chi_{\mathcal{C}}(\mathbf{r}) = 1$ if cell($\mathbf{r}$) $\in \mathcal{C}$, else 0. The entering condition is

$$\exists\, k \in [0, n-1] \;:\quad \chi_{\mathcal{C}}(\mathbf{r}_k) = 0 \quad \text{and} \quad \chi_{\mathcal{C}}(\mathbf{r}_{k+1}) = 1.$$

When this occurs, the candidate's identifier is recorded in the generator list and its *entry point* is taken as $\mathbf{r}_{k+1}$ (stored for later truth-reco comparisons).

If the *first* trajectory point lies inside the cluster $\big(\chi_{\mathcal{C}}(\mathbf{r}_0) = 1\big)$, the algorithm checks the parent track and repeats the test recursively, ensuring that the selected generator is the ancestor that actually *enters* the cluster before any in-cluster descendants are produced[1].

After this procedure over all candidates, the resulting generator list and entry-point map provide the truth anchors used in the subsequent validation. Because the "entering test" relies on MC trajectory points rather than deposited energy, it naturally identifies neutral particles (e.g. photons) as cluster generators: a photon can cross into the ECAL and convert only afterward, so its daughters deposit the energy while the photon itself leaves no ionization signal. The outside→inside crossing of the photon trajectory of the cluster is nonetheless detected, and the photon is recorded as the generator. A scheme of the generator candidates selection is shown in Fig 4.8.

After the entering test has identified the generator track IDs associated with a cluster, the program constructs per-generator records and a truth summary for the cluster.

Once the list of generators has been identified through the entering test, each candidate is characterised and its contribution to the cluster is quantified. For every generator, the program records its particle identity, as its PDG Code, and its Parent identity, the entry point in the ECAL inferred from the trajectory

[1] In rare cases a candidate has no trajectory point that maps to a valid ECAL cell in $\mathcal{C}$ (e.g. particle propagation gaps), but a child along the recursion chain does. In that situation the child is taken as generator and its earliest trajectory point in ECAL is stored as the entry point.

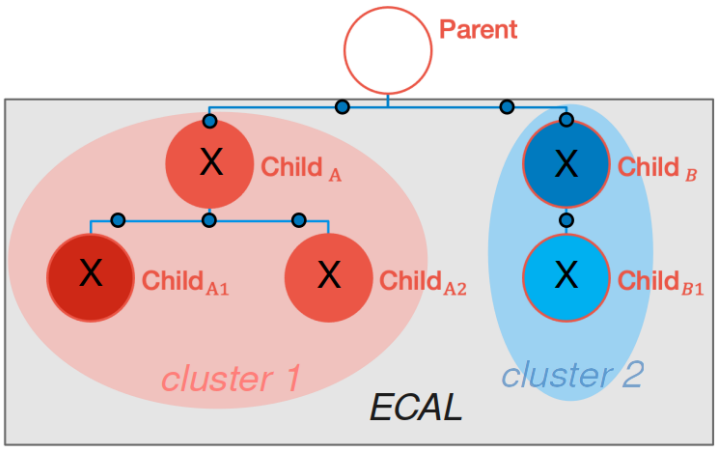

Figure 4.8: Scheme of the generator candidates selection. For $cluster_1$ the contributing particles are $Child_A$, $Child_{A1}$ and $Child_{A2}$ while for $cluster_2$ the contributing particles are $Child_B$ and $Child_{B1}$. Out of all the particles only $Child_A$ and $Child_B$ are entering the cluster and thus are taken as generator for $cluster_1$ and $cluster_2$ respectively

points, and the initial kinematics at that point. The generator's contribution to the cluster is then evaluated by accumulating the true deposited energy associated with the generator and its descendants within the cells belonging to the cluster. The sum over all generators defines the cluster's true energy, while the generator with the largest contribution is flagged as the *leading generator*.

For further analyses, several cluster topologycal information are stored in the truth record, and to characterise the longitudinal development, the energy collected in each ECAL layer is used to compute an asymmetry,

$$\mathrm{A_{cl}} = \frac{E_\ell^{Max} - E_\ell^{Min}}{E_\ell^{Max} + E_\ell^{Min}}, \tag{4.31}$$

where $E_\ell^{Max/Min}$ is the maximum/minumum reconstructed energy in the layers of the clusters. The initial momentum of the leading generator is also evaluated from Monte Carlo, allowing the calculation the calorimetric ratio

$$E/p = \frac{E_{\mathrm{reco}}}{|\vec{p}_{\mathrm{init}}|},$$

for further analyses. Finally, a truth summary object is filled for the cluster and written to the output, including per-layer counters and the ordered list of generators. The members of the truth summary objects are listed below:

Generator record (per contributing ancestor).

- Particle identity and parent identity (PDG codes).
- Track identifiers for the generator and its parent.
- True energy attributed to the cluster for this generator (sum over the generator's family within the cluster cells).
- Initial energy and initial momentum magnitude at ECAL entry.
- Entry point in ECAL: three-dimensional position at the first trajectory point inside the detector.

Truth summary per cluster.

- Identifier of the leading generator (reported by particle type).
- Reference space-time point associated to the cluster (position and time).
- Total true energy assigned to the cluster and corresponding visible-energy proxy.
- Number of Monte Carlo trajectories linked to the cluster and cluster size indicators.
- Total number of cells and per-layer cell counts.
- True energy per layer and indicators of the layer(s) with maximal contribution.
- Longitudinal asymmetry (A_{cl}) as defined in Eq. 4.31.
- Calorimetric ratio E/p using the reconstructed cluster energy over the leading generator's initial momentum.
- Indicator for the presence of multiple generators and the ordered list of generator records.

4.6.2 Reconstruction validation

Using the algorithm presented in Sec. 4.6.1 the reconstruction algorithm has been validated by comparing reconstructed cluster observables with the corresponding particle generator Monte Carlo variables. For this purpose Monte Carlo samples of different particle beam have been produced using the full simulation chain and true and reconstructed variables have been plotted togheter to check their consistency.

Muons. A sample of 10^3 negative muons with vartex at $(0, -2.38, 23.91)m$, corresponding to the SAND detector center, with energy uniformely distributed between 1 MeV and 6 GeV and uniform angular distribution were generated. In Fig. (4.11) a Display of the MonteCarlo Tracks and Energy Deposit of a muon event, on a schematic representation of SAND, is shown.

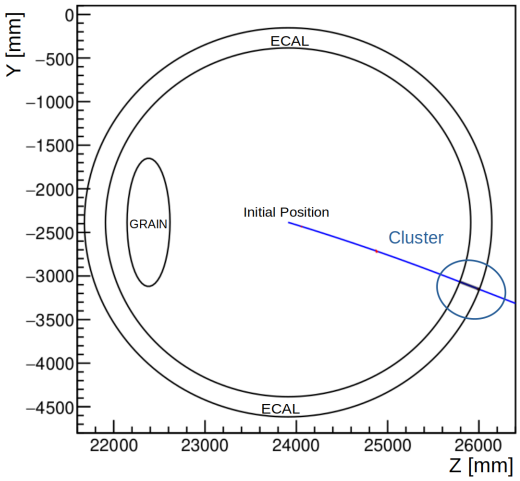

Figure 4.9: Muon Monte Carlo Display in the SAND YZ view, the blue full lines represent the muon track and the **black** dots represent the energy deposits.

The reconstructed cluster variables of energy and position were compared to their true values in correlation plots to assess the detector response. The reconstructed and true energy correspond to the visible energy deposited by the particle, while the true position is defined as the first trajectory point of the chosen generator particle within the cluster cells. This is then compared with the reconstructed cluster apex. The results show good linearity for both energy and position. The results are showed in 4.10

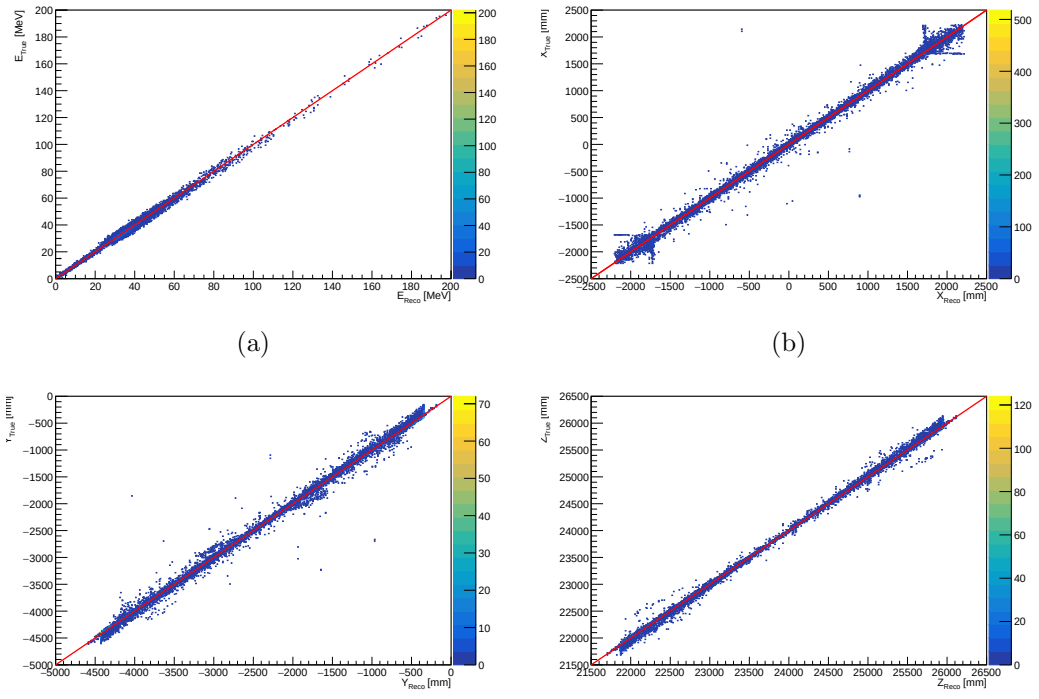

(a) (b) (c) (d)

Figure 4.10: True versus reconstructed energy and coordinates (E (a), X (b), Y (c), Z (d)) for muon events. The red line represents the bisector.

Electrons. A sample of 10^4 electrons with vertex at $(0, -2.38, 23.91)m$, corresponding to the SAND detector center, with energy uniformely distributed between 100 MeV and 6 GeV (electrons at lower energies do not reach the ECAL) with uniform angular distribution were generated. In Fig. (4.11) a Display of the MonteCarlo Tracks and Energy Deposit of an electron event, on a schematic representation of SAND, is shown.

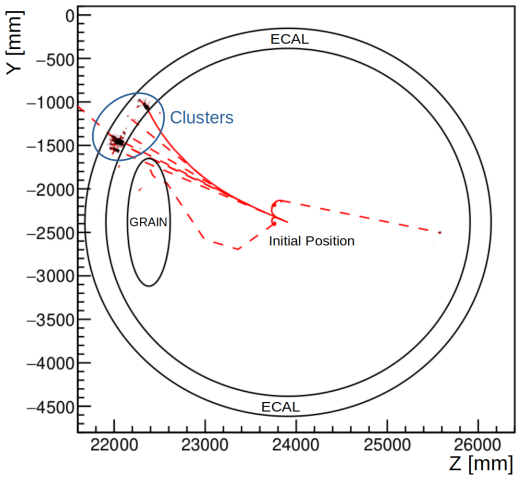

Figure 4.11: Electron Monte Carlo Display in the SAND YZ, the red full lines represent electron and positron, dashed red lines represent γ, the **black** dots represent the energy deposits.

The reconsturcted variables were compared with the truth variables in correlation plots and the results show good linearity. The position resolution appears worse than in the muon case, but this is expected given the chosen definition of the true position and the different cluster topologies: electromagnetic showers in the ECAL modules for electrons versus track-like clusters for muons. results are shown in Fig. 4.12.

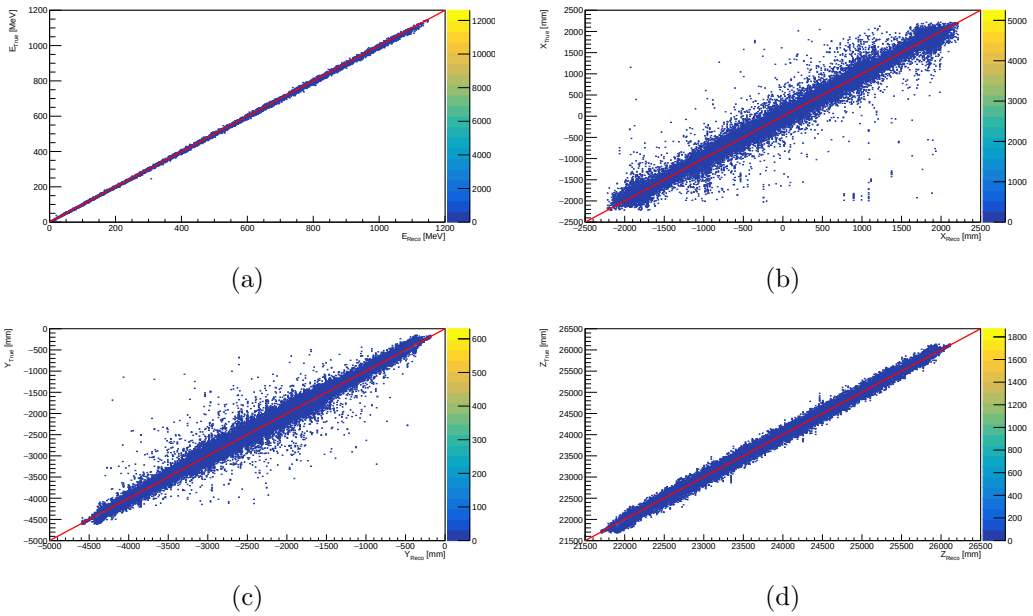

Figure 4.12: True versus Reconstructed energy and coordinates (E (a), X (b), Y (c), Z (d)) for electron events. The red line represents the bisector.

Energy Resolution

To evaluate the energy resolution, a sample of 150×10^3 e^- particle events was generated, with the interaction vertex fixed at $(0.0, -2.38, 25.81)$ m, i.e. at the end of the tracker, for several fixed input energies.

For each sample, the distribution of $E_{\text{reco}} - E_{\text{true}}$ (an example is shown in Fig. 4.13) was fitted with a Gaussian function, and the corresponding width σ was extracted. The true energy for each sample (defined as the particle energy at the first trajectory point within the cluster) is not fixed but can vary depending on the interactions of the generated particle before reaching the calorimeter, thus it was evaluated from the distribution of E_{true} at the cluster level: the mean value of this distribution was taken as E_{true}, while the associated uncertainty was estimated from the standard deviation of the distribution.

The results are summarized in Fig. 4.14, which shows the dependence of σ/E_{true} on E_{true}. The distribution is fitted with the standard calorimetric resolution function reduced to a single stochastic term:

$$\frac{\sigma_{\text{gaus}}}{E_{\text{true}}} = \frac{a}{\sqrt{E_{\text{true}}[\text{GeV}]}}, . \tag{4.32}$$

The fit yields:

$$\frac{(5.02 \pm 0.15)\%}{\sqrt{E_{\text{true}}[\text{GeV}]}},, \tag{4.33}$$

with a goodness of fit of $\chi^2/\text{ndf} = 3.53/9$, To be compared with the KLOE result of $5.7\%/\sqrt{E[\text{GeV}]}$ based on real data. In the explored energy range (up to 1 GeV), the constant term is negligible. This improved resolution is expected, since the calorimeter configuration adopted in the MC has a larger effective sampling than the original KLOE detector.

These results, together with the demonstrated linearity of the reconstructed quantities, fully validate the performance of the ECAL reconstruction algorithms.

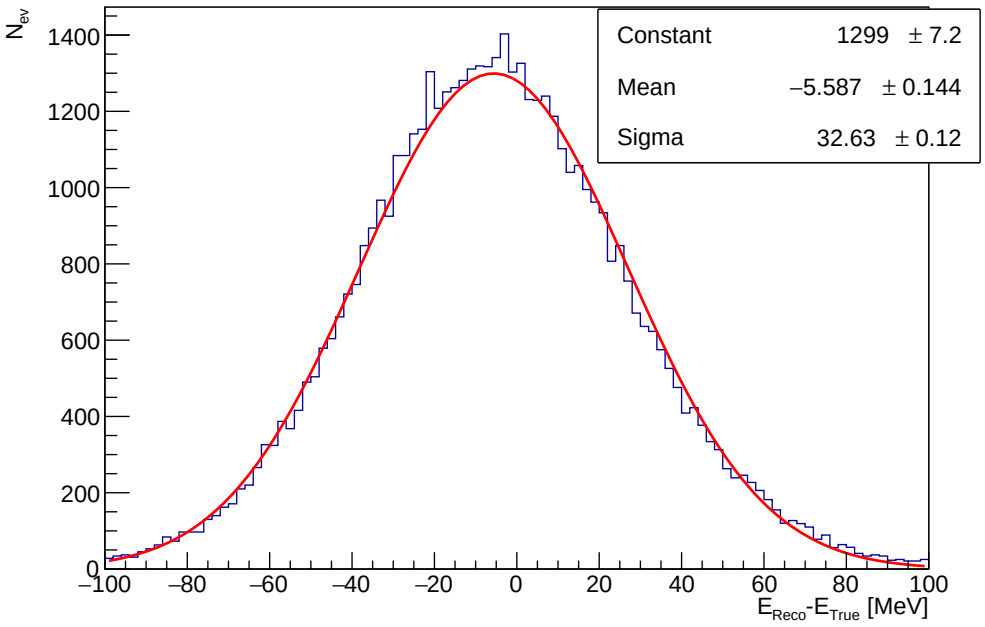

Figure 4.13: Distribution of $(E_{\text{reco}} - E_{\text{true}})$ for electron events at 400 MeV, with Gaussian fit.

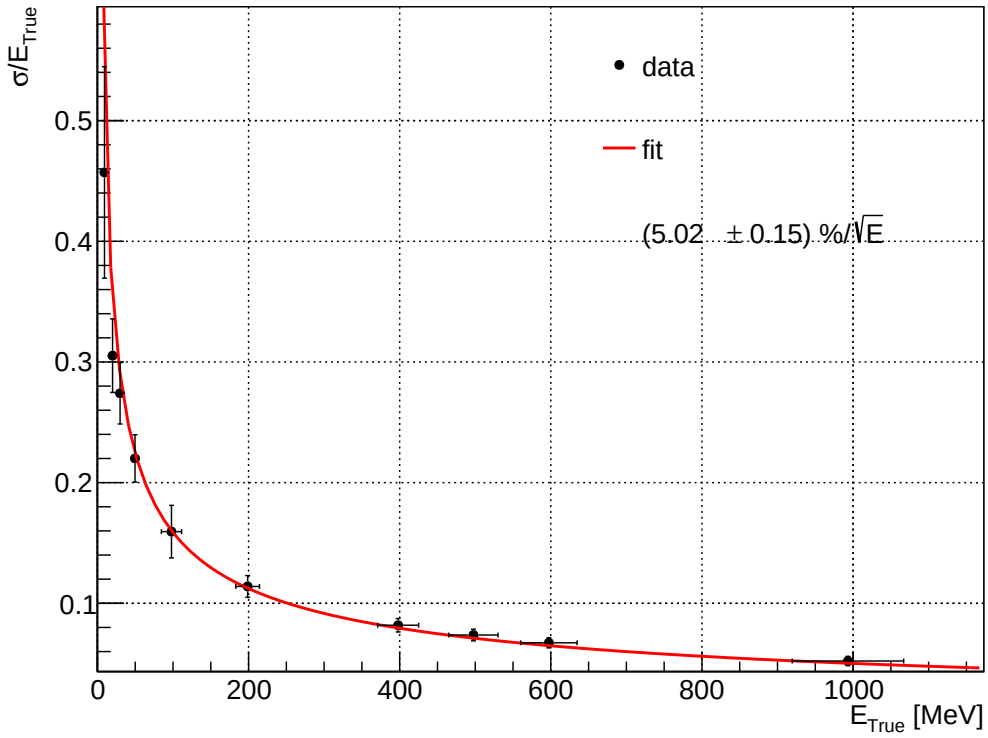

Figure 4.14: Energy resolution σ/E_{true} vs. E_{true} for electron events; fit overlaid ($\chi^2/\text{ndf} = 3.5/9$).

Chapter 5

ECAL Calibration Strategies in SAND

The calibration procedures and strategies of a detector are of fundamental importance for its operation and performance.
The goal of this chapter is to define and evaluate a practical calibration programme for the SAND ECAL in the conditions of the DUNE Near Detector hall. While the ECAL calibration in the KLOE experiment at DAΦNE was thoroughly defined and validated, the operational context for SAND at the DUNE Near Detector differs substantially. Operating underground, SAND will not benefit from an abundant cosmic-ray flux, and interactions will not originate from a fixed, well-known vertex within the calorimeter. These constraints preclude several standard surface-based calibration techniques and motivate alternative in-situ strategies that rely on other calibration particle sources.

The calibration programme aims at determining the fundamental ECAL constants with precision, namely: the *absolute energy scale* (conversion from measured charge/ADC counts to deposited energy); the *inter-channel response equalisation* (removal of relative gain non-uniformities across modules and readout ends); the *per-end timing calibration*, comprising fixed offsets and effective signal-propagation delays along the scintillator fibers and light guides, and a *global* t_0 providing a common timing reference for synchronisation within SAND and across the Near Detector subsystems. In this chapter several strategies for different calibration constant have been evaluated to be carried out in situ at the Near Detector site. The feasibility and expected precision of every method are quantified with simulations: the truth-matching framework developed in chapter 4 is exploited to access the Monte Carlo truth for the particles generating each cluster and to build unbiased the calibration procedures.

This chapter is structured as follows. First, the calibration strategies adopted in KLOE at DAΦNE are summarised, with emphasis on elements transferable to SAND and on limitations specific to the Near Detector environment. Next, an in-situ approach based on muons produced by neutrino interactions in the surrounding rock and in the SAND detector is presented and used to develop both the energy and the time calibration of the ECAL. A preliminary method for

determining the global t_0 required for inter-subdetector synchronisation is then proposed. Finally, future steps to refine these procedures and to validate the overall calibration methods with detailed simulations and forthcoming data are outlined.
In parallel, a dedicated cosmic-ray stand built at LNF for the characterisation of individual ECAL modules is described, together with its first performance results, providing a complementary validation of the simulation.

5.1 ECAL Calibration at DAΦNE

The KLOE programme at DAΦNE established a complete ECAL calibration chain, covering the energy scale and equalisation, the intra-module time tuning taking into account offsets and effective light-propagation in the fibers, and the global time reference. The procedure combined minimum-ionising particles (MiPs) from cosmic rays and beam control samples, together with kinematic benchmarks from e^+e^- collisions

5.1.1 Energy response and MiP equalisation

For each readout end (A, B) of cell i, pedestal-subtracted charges $Q_i^{A,B} - P_i^{A,B}$ (in ADC counts) are converted to deposited energy through the MiP reference of Eq. (4.16). The per-channel constant $C_i^{A,B}$ is obtained from the MiP peak fits (see Fig. 5.1). The distribution for each cell is obtained by selecting a "Golden MiP"

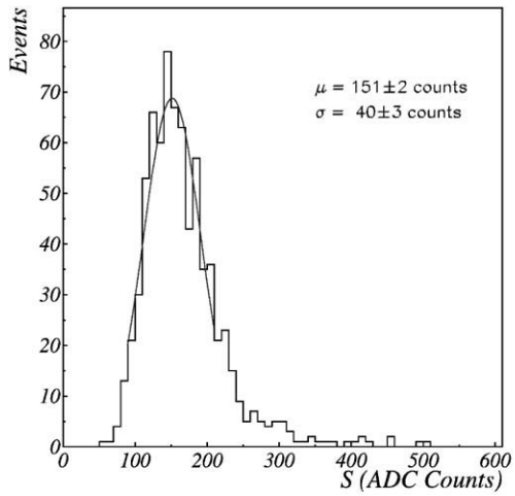

Figure 5.1: Energy signal spectrum for minimum ionizing particles in KLOE. Only a limited region around the peak is fitted. [56]

sample, defined as clusters formed by cells in the same column of the module, ensuring that the particle crosses the all the layers of the module.

5.1.2 Absolute energy scale

The absolute energy scale is fixed with kinematically constrained beam samples. Large-angle $e^+e^- \to \gamma\gamma$ events provide two back-to-back photons with energy equal to the beam energy ($E_{\rm ref} \simeq 510$ MeV) up to small radiative effects; Bhabha events in the central barrel offer an independent charged-lepton with track-cluster matching and known kinematics. A global scale factor K is obtained by requiring that the average reconstructed cluster energy for the reference sample equals the known beam energy. Figure 5.2 shows $E_{\rm cal}$ versus the azimuth angle for Bhabha events before and after the calibration procedure.

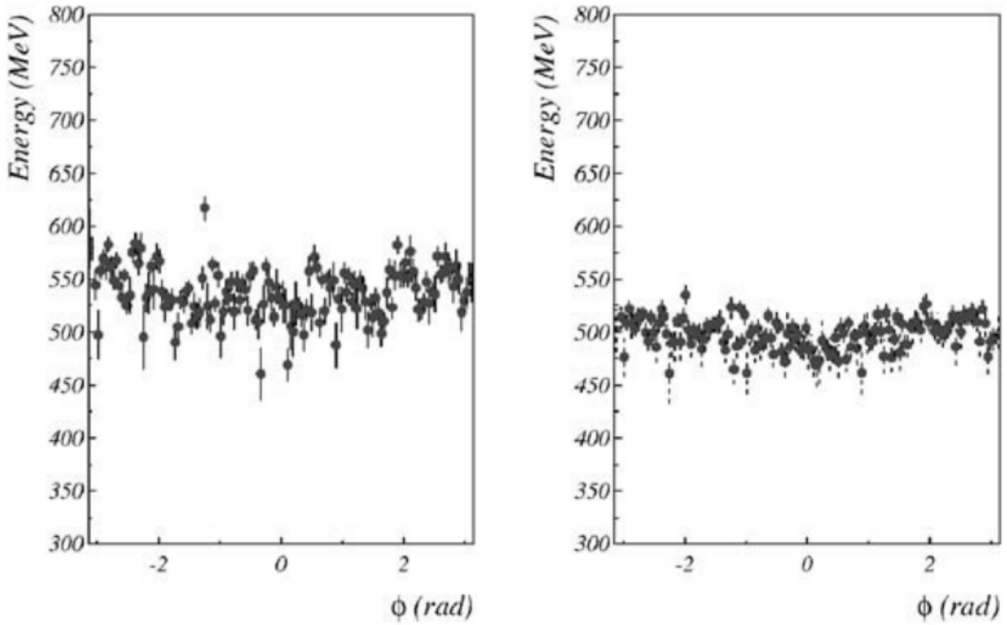

Figure 5.2: Distribution of E_{cl} vs. ϕ for Bhabha events in the barrel. Before the calibration procedure (left). After (right). [56]

5.1.3 Intra-module time calibration

Hit position along a cell, see Fig. (5.3), and time at the cell center are reconstructed from the two TDC measurements (t_A, t_B) at the two ends:

$$x = \frac{1}{2} v_{lfb}(t_A - t_B) + \frac{1}{2} L - \frac{1}{2} v_{lfb} \Delta t_0 \tag{5.1}$$

$$t = \frac{1}{2}(t_A + t_B) - \frac{L}{2v_{lfb}} - t_0 - t_G^0 \tag{5.2}$$

in which L is the length of the module, v_{lfb} is the light velocity in the fibers, t_G^0 is the global time offset of the primary interaction vertex of the event, and:

$$t_0 = \frac{1}{2}(t_A^0 + t_B^0) \tag{5.3}$$

$$\Delta t_0 = t_A^0 - t_B^0 \tag{5.4}$$

are per-cell time constants. Both time constants are determined from cosmic-ray tracks. The sum-offset t_0 is obtained from the mean of the time-residual distribution built with a track-based time-of-flight prediction (see Sec. 5.2.3), followed by an iterative per-cell adjustment that minimises the residuals, as illustrated in Fig. 5.4. The differential quantity is extracted from the distribution of $(t_A - t_B)$: its central value fixes the Δt_0 offset , while v_{lfb} can be evaluated from its width (Fig. 5.5).

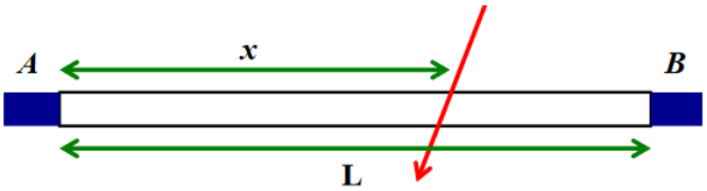

Figure 5.3: Schematic representation of the reconstructed position along the barrel module.

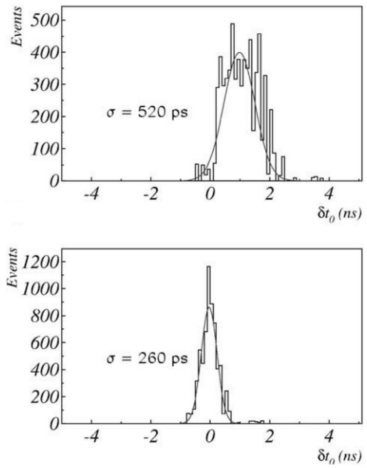

Figure 5.4: Residual distributions before and after t_0 corrections using cosmic ray particles in KLOE [56].

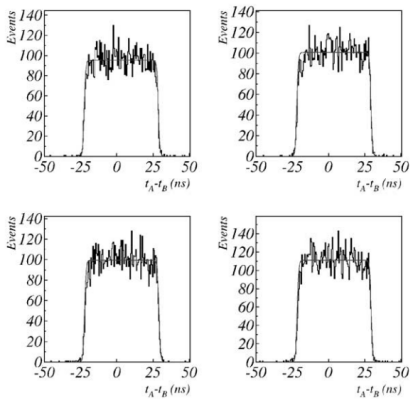

Figure 5.5: $t^A - t^B$ spectra in KLOE. The center of the distributions gives $t_0^A - t_0^B$. The light velocity v_{vlfb} is obtained from the width [56].

5.1.4 Global t_0^G from collider timing

The global reference t_G^0 is obtained from two-photon final states, using the cluster time corrected for time of flight: the distribution of $(t_{cl} - r_{cl}/c)$ exhibits peaks separated by the RF period T_{RF} (Fig. 5.6). Aligning the peak corresponding to the nominal bunch crossing yields t_G^0, ensuring a common time origin across the detector.

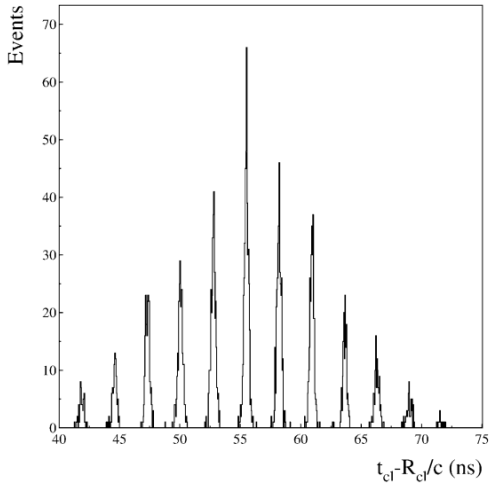

Figure 5.6: $t_{cl} - r_{cl}/c$ distribution for 2γ events. Peaks are separated by T_{RF} [56].

5.2 Calibration in SAND with Muons from ν-interactions

One of the main differences between the SAND and KLOE environments is that the Near Detector will be underground, providing shielding against one of the primary sources of MIPs used for calibration, as described in 5.1. At the surface, the cosmic-ray muon flux is $\sim 0.02\ \mu/\left(s\ \mathrm{cm}^2\right)$, which translates to $\sim 10^4\ \mu/\mathrm{s}$ over the ECAL and corresponds to about 100 Hz of "Golden MIPs" in KLOE. Underground, the flux is expected to be reduced by a factor of ~ 100, yielding $\sim 100\ \mu/\mathrm{s}$ on the ECAL without selections and, rescaling the KLOE numbers, roughly ~ 10 "Golden MIPs" events per cell over a 24-hour period.
With the reduced flux underground, we cannot rely on cosmic rays alone to calibrate the calorimeter modules. However, it is possible to exploit charged particles produced by neutrino interactions in the surrounding rock, within the Near Detector Hall, in other ND sub-detectors, and in the SAND magnet, yoke, and upstream ECAL modules. To assess the feasibility of this approach, this thesis studies ν interactions in rock and in the ND and presents a dedicated selection procedure, together with ECAL cell occupancy maps from these events.

5.2.1 Event Production

A preliminary sample of 10^5 ν_μ has been generated in the simulation with the nominal DUNE beam direction, energy spectrum, and source position. In this production, neutrinos are allowed to interact in any volume of the ND geometry as well as in the surrounding rock. For the optimization study, we impose a transverse interaction window in detector coordinates (origin at the upstream edge of the ND Hall) defined as

$$\mathcal{W}_{\text{NEAR-ROCK}} = \Big\{ x \in [-15.0,\, 10.0]\ \mathrm{m},\ y \in [-11.6,\, 22.0]\ \mathrm{m} \Big\}, \tag{5.5}$$

which corresponds to a region of size 25.0 m $\times$ 33.6 m in (x, y) at the beam production point. Along the beam direction we select $z \in [-20,\, 30]$ m.

This sample is used study the selection of usable neutrino interactions (i.e., those producing charged tracks that enter SAND and cross the ECAL). A plot in the (x, y) plane with the resulting ν interaction vertexes is presented in Fig. 5.7.
Not all interactions are suitable for calibration. As a minimal preselection, we require events to contain at least one reconstructed ECAL cluster. The vertex distribution for events passing this criterion is shown in Fig. 5.8.

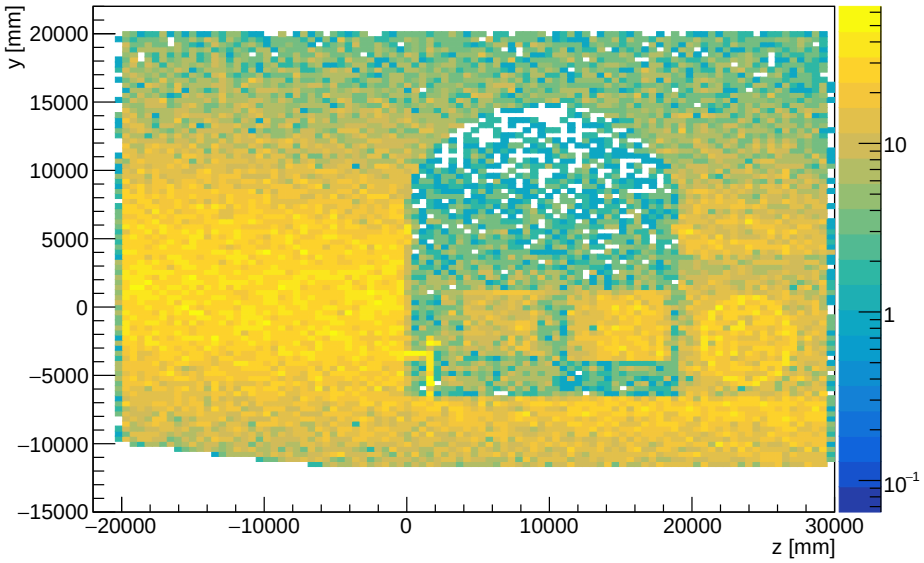

Figure 5.7: ν_μ vertex distribution with fiducial window 5.5 .

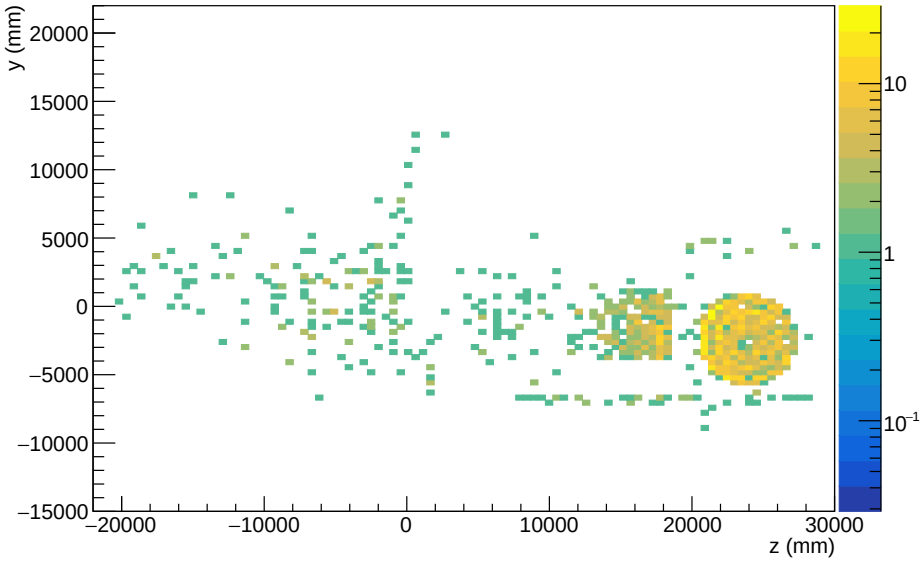

Figure 5.8: ν_μ vertex distribution of events with at least one cluster in ECAL.

Figures 5.9,5.10 and 5.11 show the vertex distributions along the x, y, and z axes, respectively, for both the total sample and the subset of selected events

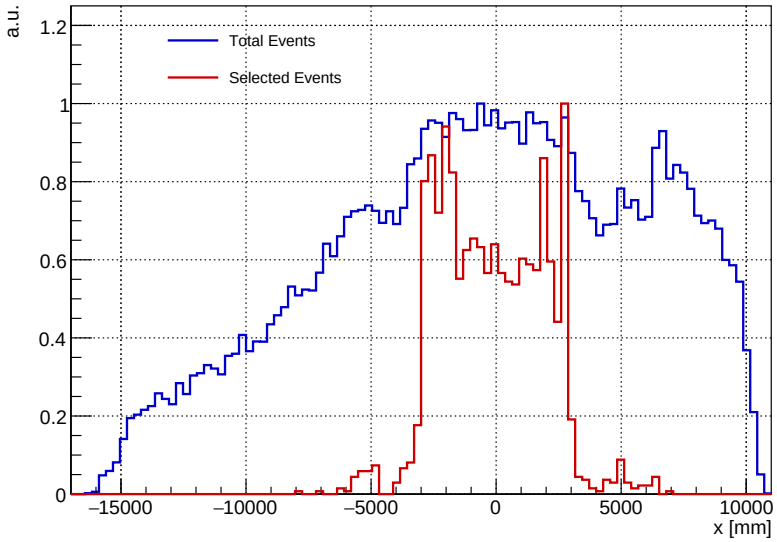

Figure 5.9: ν_μ vertex distributions, total and selected, normalized in the x coordinate.

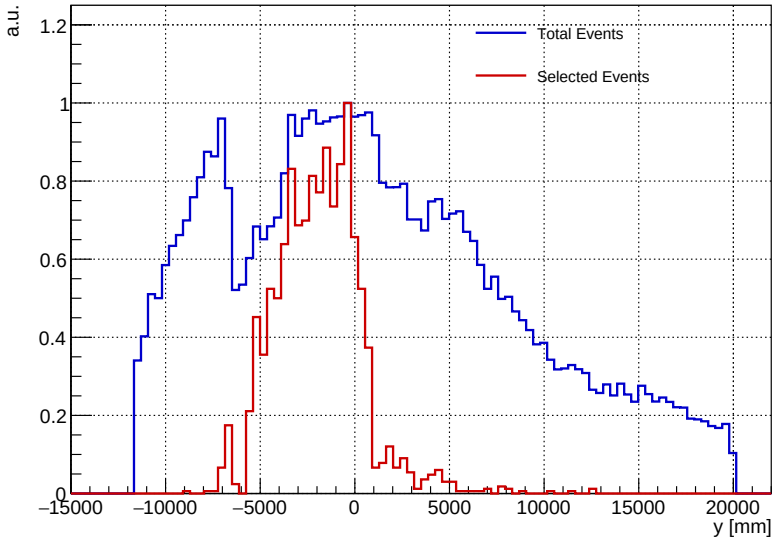

Figure 5.10: ν_μ vertex distributions, total and selected, normalized in the y coordinate

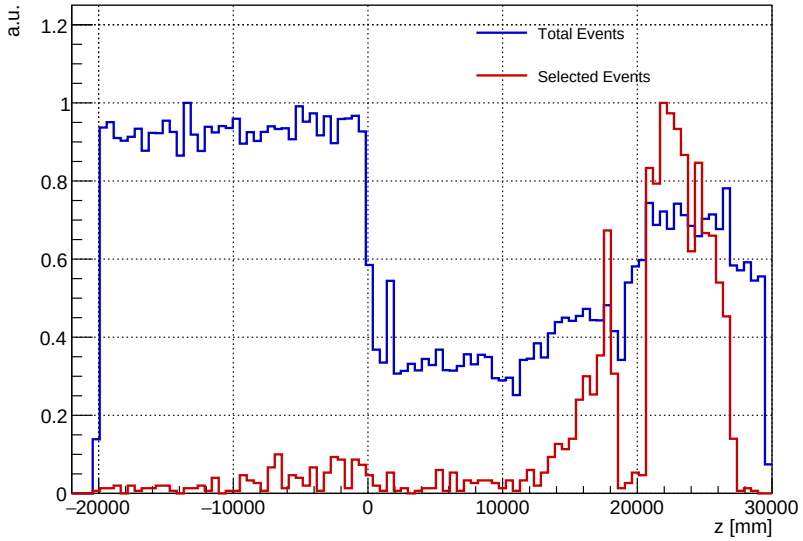

Figure 5.11: ν_μ vertex distributions, total and selected, normalized in the z coordinate.

Based on the distributions discussed above, the transverse fiducial window defined at the beam production point that optimises the yield of selected events is

$$\mathcal{W}_{\text{NEAR-FID1}} = \Big\{ x \in [-3.20,\, 3.20] \text{ m},\ y \in [-3.55,\, 3.05] \text{ m} \Big\}, \tag{5.6}$$

which corresponds to a region of size 6.40 m $\times$ 6.60 m in (x, y). Along the beam direction we select $z \in [-10,\, 30]$ m. This window is adopted for the massive production used in this calibration study.

Movable ND sub-detectors such as TMS and ND-LAr, which add significant interaction material, are *not* included in the baseline geometry for two reasons: (i) they will not always be on-axis (they operate within the ND off-axis program), and (ii) they are not planned to be installed during the first months of DUNE data-taking. Excluding them provides a conservative, time-stable configuration that reflects early-data conditions and avoids dependence on the movable-detector setup.

A sample of 10^6 ν_μ was generated within the fiducial window (5.6), split into 4×10^3 files, each corresponding to $\sim 7 - 8 \times 10^{13}$ POT (approximately one spill), for a total equivalent of $\sim$ 1.3 hours of data taking. The (x, y) distribution of interaction vertices for a representative subsample of this production is shown in Fig. 5.12.

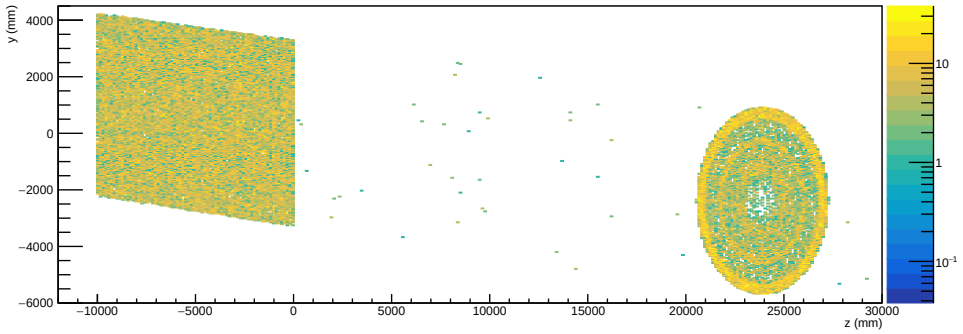

Figure 5.12: ν_μ vertex distribution with optimised window. The apparent compression of the SAND dectector is a plotting/aspect-ratio artifact.

This selection yields a pure muon sample, providing optimal conditions for the present work, which represents a first attempt at developing and validating ECAL calibration procedures within the SAND framework. Future studies will build upon this approach by selecting muon candidates combining information from the various SAND subdetectors, including the tracker. Under the truth-match selection, 94,255 muon events are retained. Their production vertices populate the ND volumes and the surrounding rock as summarized in Table 5.1. The largest contributions come from the ECAL volumes and the magnet yoke, with a substantial fraction from the surrounding rock, consistent with the optimization objective of the chosen window for calibration statistics.

Region / volume	Events	Fraction [%]
ECAL volumes	35,536	37.70
Yoke	32,152	34.11
Rock	20,054	21.28
Tracker	3,945	4.19
Solenoid	1,893	2.01
GRAIN	632	0.67
Detector enclosure	43	0.05
Total selected	**94,255**	**100.00**

Table 5.1: Distribution of the 94 255 selected events (requirement: $\geq$1 ECAL muon cluster) with $\mathcal{W}_{\text{NEAR-FID1}}$. Percentages are relative to the total selected sample.

5.2.2 Energy Calibration

In order to reproduce the MIP-peak calibration distributions described in 5.1 and to assess the feasibility of the rock-muon-based method, the sample defined in 5.2.1 was used and it was first applied the "Golden MIP" topology cut to ECAL muon clusters. In this selection, each cluster is required to comprise hits from cells lying within a single column. The resulting single-cell energy spectrum, shown in Fig. 5.13, is obtained by aggregating all cells; this is acceptable in Monte Carlo, where all cells have the same response by definition (equal calibration constants), although per-cell spectra will be produced in a subsequent step. The distribution is fitted with the following model:

$$\begin{aligned}\mathcal{M}(x) = f_{\mathrm{s}} \left[\mathrm{Landau} \otimes \mathrm{Gauss}\right](x;\, m_L,\, \sigma_L,\, \mu_G,\, \sigma_G) \\ + \left(1 - f_{\mathrm{s}}\right) \mathrm{CrystalBall}(x;\, \mu_{CB},\, \sigma_{CB},\, \alpha,\, n)\,^{1}\end{aligned} \tag{5.7}$$

in which:

- $f_{\mathrm{s}} \in [0, 1]$ - signal fraction in the mixture (the PDFs are individually normalized).
- m_L - Landau most-probable value (MPV), equal to the the MIP peak.
- σ_L - Landau scale parameter.
- $\mu_G = 0$ (fixed) - mean of the Gaussian smearing; fixing it to zero keeps the convolution centered on the Landau location (any global bias is absorbed by m_L).
- $\sigma_G > 0$ - Gaussian resolution.
- μ_{CB} - CrystalBall Gaussian-core mean (background peak position).
- $\sigma_{CB} > 0$ - CrystalBall Gaussian-core width.
- α - transition point (in units of σ_{CB}); $\alpha > 0$ gives a low-side tail, $\alpha < 0$ a high-side tail.
- $n > 1$ - power-law exponent controlling the tail slope.

The Crystal Ball term is included as an empirical model for the residual non-MIP component; its role becomes clear in the following when looser topology selections are considered, where this contribution appears as a peaked distribution with an asymmetric tail. However, with the "Golden MIP" topology selection cut, the

[1] Crystal Ball (CB) function: $\mathrm{CB}(x; \mu, \sigma, \alpha, n) = \begin{cases} e^{\left(-\frac{1}{2}t^2\right)}, & t > -\alpha, \\ A\,(B - t)^{-n}, & t \le -\alpha, \end{cases}$ with $t = \frac{x-\mu}{\sigma}$, $A = \left(\frac{n}{|\alpha|}\right)^n e^{-\alpha^2/2}$, $B = \frac{n}{|\alpha|} - |\alpha|$.

background from tracks that do not cross the full cell length is expected to be negligible, as confirmed by the data.

The number of events per cell for the "Golden MIP" selection in both barrel and endcap regions is shown in Fig. 5.14. As expected, the most populated modules are those aligned with the beam direction (i.e., barrel modules 6-7 and 17-18), while the endcaps register almost no events under this strict topology.

To improve coverage, a relaxed topology requirement is applied in which clusters must contain at least three cells belonging to the same column. The resulting cell energy distribution is shown in Fig. 5.15, with the fit model of Eq. 5.7 overlaid. In this case, a background component becomes visible -consistently captured by the chosen model- while the MIP peak remains clearly distinguished. The corresponding occupancy map for the relaxed selection, displayed in Fig. 5.16, demonstrates enhanced population in the endcaps and in barrel modules lying in the plane perpendicular to the beam direction.

Due to the ability of the model to distinguish the background peak from the signal peak, in Fig.5.17 the cell energy distribution from muon clusters without cut on their topology is presented. The background peak and the signal peak are still distinguished by the model, and the results for the three cuts (Golden MIP, relaxed 3-in-column, and no-topology) are consistent among them. Without topology cuts applied the occupancy map, showed in 5.18, presents an almost uniform distribution for both cells and endcap modules.

The MIP-peak calibration constant was extracted cell-by-cell in the ECAL for the three topology selections. Each spectrum was fitted with the chosen model, and the outputs were saved in a ROOT file with the following directory structure:

```
<root-file>
|-- detX/                      # X = 0,1 for endcaps; X = 2 for barrel
|   `-- moduleYY/              # YY = module ID.
|       `--energy/
|          |-- fitResults/        # Per-cell fit objects
|          |   `-- fitResult_h_cell<Sel>_<cellID>
|          |-- canvases/          # Rendered canvases of fits/plots
|          |   `-- c_cell<Sel>_<cellID>
|          |-- histograms/        # Input histograms used in the fits
|          |   `-- h_cell<Sel>_<cellID>
|          `-- summary/           # Module-level overviews
|              `-- h_summary_<Sel>_moduleYY
```

In which:

- `<Sel>` encodes the selection: `NoCut`, `3Col`, or `SingleCol` (Golden MIP).
- `<cellID>` is the unique Cell ID following the notation in Sec. 4.4.3.

Example histograms for barrel module 17, layer 1, column 5 are shown in Fig. 5.19 for the three topology selections. Figure 5.20 displays the MIP-peak values for barrel module 17 without topology cuts; the increase observed in the outermost layer is consistent with its greater thickness.

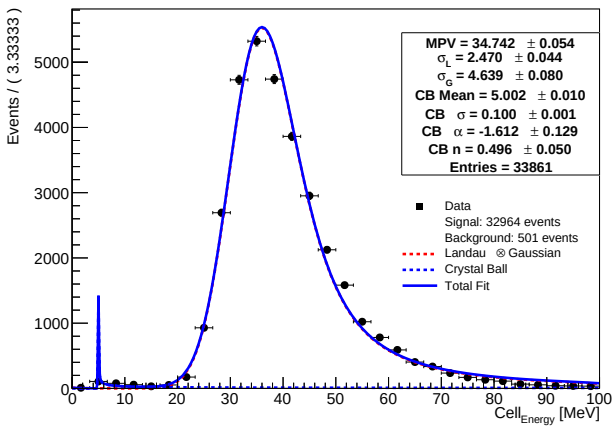

Figure 5.13: Cell energy distribution of μ clusters for "Golden MIP" in SAND.

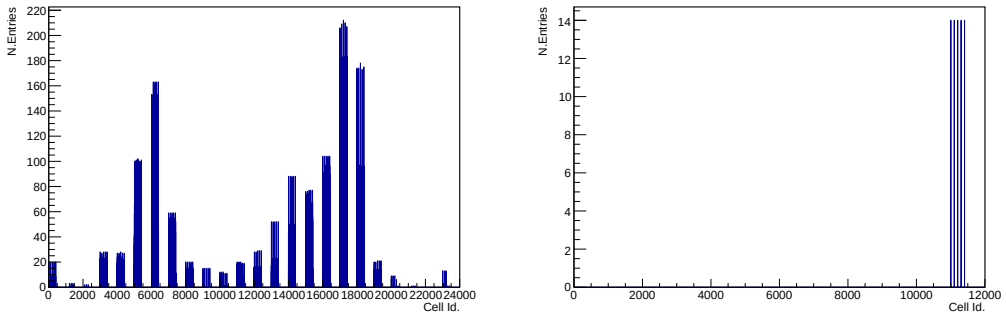

(a) Barrel (b) Endcap ($x < 0$)

Figure 5.14: ECAL cell occupancy maps for "Golden MIP" μ clusters: (a) barrel and (b) endcap ($x < 0$). The x-axis uses the Cell ID notation of 4.4.3 minus the det Id.

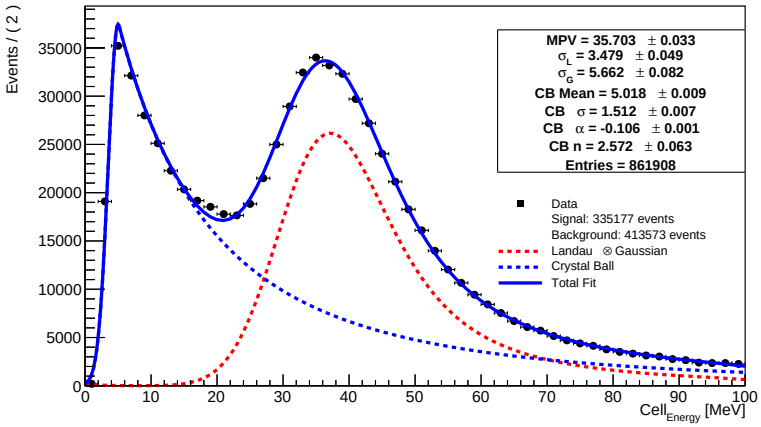

Figure 5.15: Cell energy distribution of μ clusters for a sample with relaxed cut condition, requiring at least 3 cells in a single column.

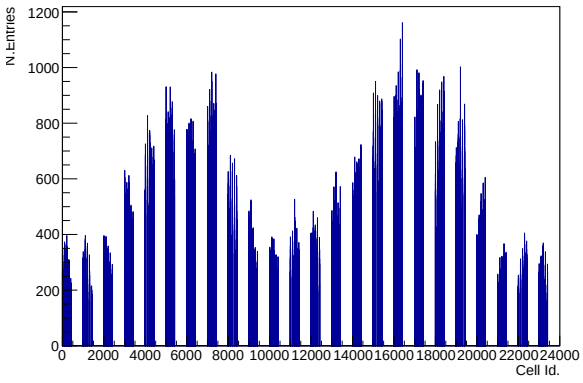

(a) Barrel

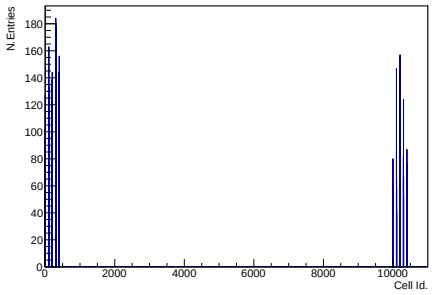

(b) Endcap ($x > 0$)

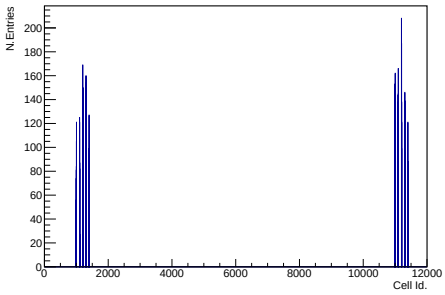

(c) Endcap ($x < 0$)

Figure 5.16: ECAL cell occupancy maps for μ clusters with the relaxed topology cut (3-in-column). Panels: (a) barrel, (b) endcap $x > 0$, (c) endcap $x < 0$. The x-axis uses the Cell ID notation of 4.4.3 minus the det id.

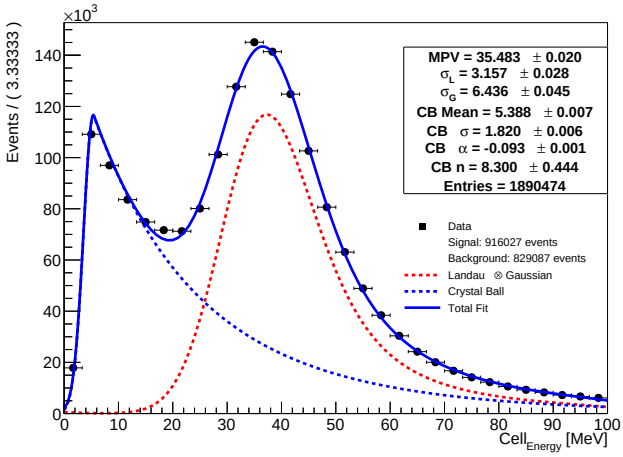

Figure 5.17: Cell energy distribution of μ clusters with no cuts applied.

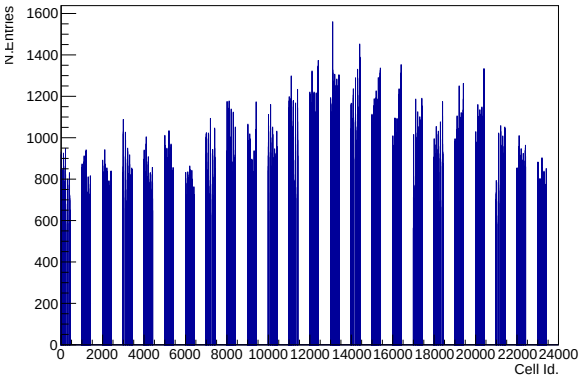

(a) Barrel

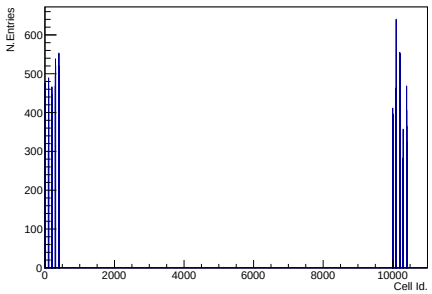

(b) Endcap ($x > 0$)

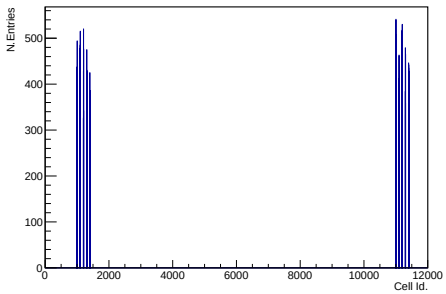

(c) Endcap ($x < 0$)

Figure 5.18: ECAL cell occupancy maps for μ clusters without topology cuts. Panels: (a) barrel, (b) endcap $x > 0$, (c) endcap $x < 0$. The x-axis uses the Cell ID notation of 4.4.3 minus the det id.

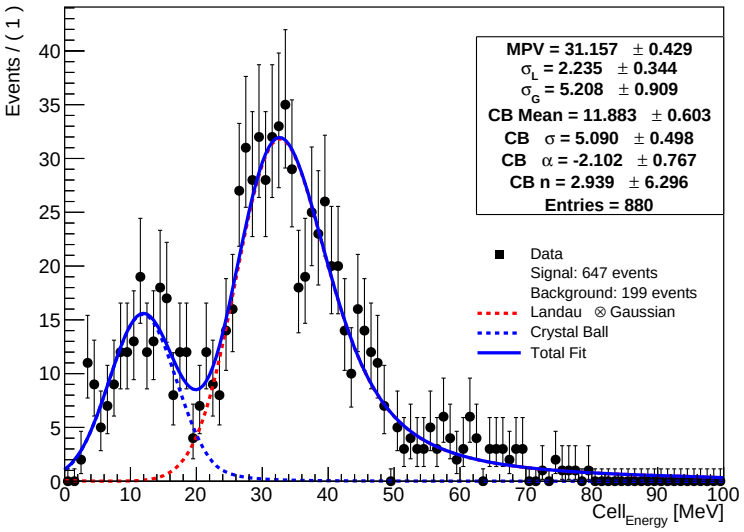

(a) No cuts

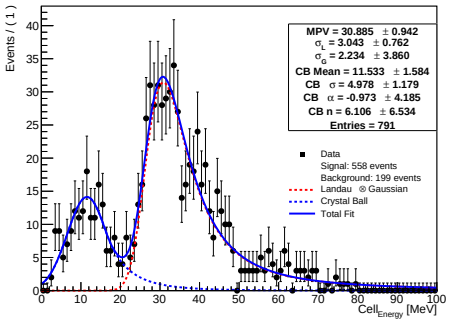

(b) Relaxed cut

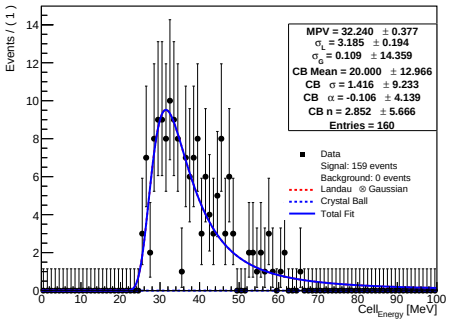

(c) "Golden MIPs"

Figure 5.19: Cell energy distributions for μ clusters in Barrel Module 17, Layer 1, Cell 5. Panels: (a) no cuts, (b) "Golden MIPs", (c) relaxed cut.

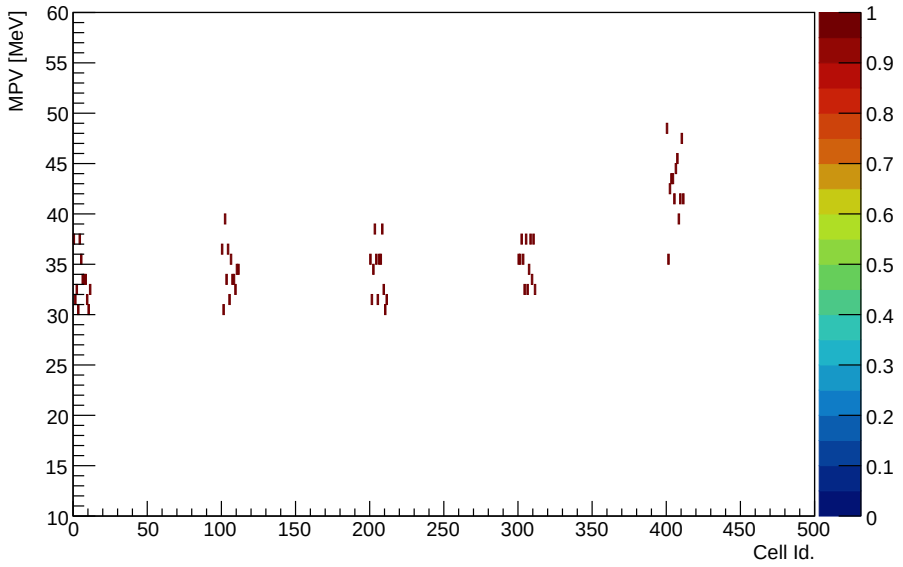

Figure 5.20: MPV vs Cell Id in Module 17 for μ clusters with no Cuts applied. The x-axis uses the Cell ID notation of 4.4.3 minus the detector and module Id.

5.2.3 Time Calibration

To reproduce the intra-module time calibration distributions described in 5.1 and to assess the feasibility of the rock-muon method via the occupancy map, a dedicated event selection is applied to the sample defined in 5.2.1.

For the Δt_0 constant in (5.4), derived from $t_A - t_B$, no additional selection is required: the per-cell distributions are obtained directly from μ clusters, and the corresponding occupancy map coincides with Fig. 5.18.

In contrast, the determination of t_0 in (5.3) demands a stricter selection to ensure a valid track-based procedure. Events are required to contain two clusters associated with the same muon, and the muon trajectory must be straight and traverse both ends of the calorimeter. Using the truth-matching information described in 4.6, the Monte Carlo trajectory of the μ that generated the clusters is retrieved.

A simple momentum cut (e.g., initial $p_\mu > 6$ GeV) can enhance the straight-track purity; however, given the long path length of rock-induced muons and possible multiple scattering in tracker volumes, a more robust criterion is adopted by explicitly testing linearity of the Monte Carlo trajectory points within the ECAL region. A linear fit is performed in x, y, and z, and a trajectory is classified as straight if the maximum absolute fit residual does not exceed a maximum

threshold. A selected event's trajectory points in the ECAL region is presented in Fig. 5.21 with the corresponding cluster's cells position. After the preliminary

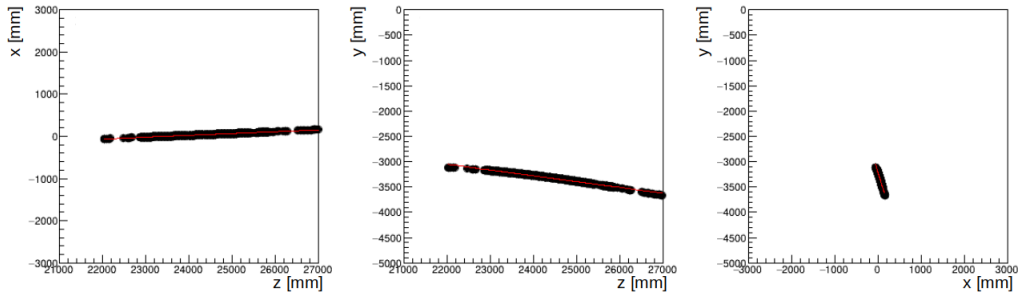

(a) Monte Carlo trajectory.

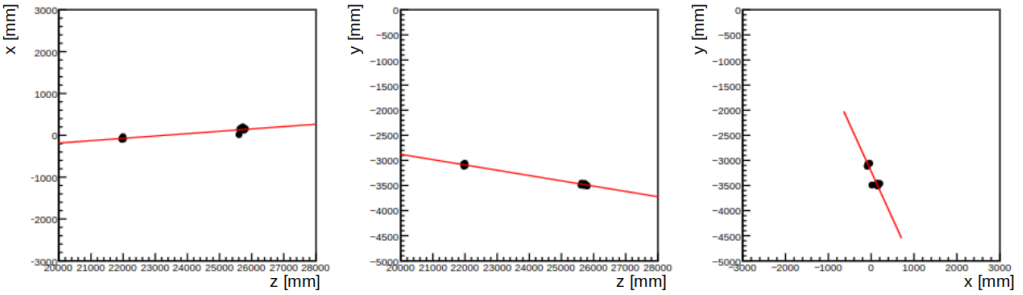

(b) Cluster cell positions.

Figure 5.21: Straight-track selection views: (a) Monte Carlo trajectory points and (b) reconstructed cluster cell positions, each shown with linear fits in the x-z, y-z, and y-x projections.

selection, events are discarded if the combination of the two muon clusters contains fewer than 10 cells, ensuring a sufficient number of points for the subsequent fits.

For each selected event, the cell positions in the y-z plane are fitted with a straight line to determine the track angle with respect to the z axis. Let

$$y(z) = a_{yz} + m_{yz}\, z\,.$$

Denote by θ the angle between the track and the z axis; the geometric fit provides an estimate of $\cos\theta$, later held fixed in the time-fit step (see Fig. 5.22). Both the geometric and time fits are performed with weights proportional to the cell energy.

A linear fit is then performed for the cell times as a function of z, with the slope

constrained to the time-of-flight gradient along the track:

$$t(z) = t_\star + \frac{z}{\beta c \cos\theta},$$

where $\beta \simeq 1$ for MIP muons and c is the speed of light. In the fit, the slope is fixed to $1/(c\cos\theta)$ and only the intercept can vary (Fig. 5.23).

For each event, fit residuals $r_i = t_i - \hat{t}(z_i)$ are computed and, for every cell, the residual values are accumulated into a histogram. After all selection cuts, the resulting occupancy map is shown in Fig. 5.24: the distribution is nearly uniform across barrel modules, with the expected depletion for modules lying in the plane perpendicular to the beam direction, as well as in the endcaps.

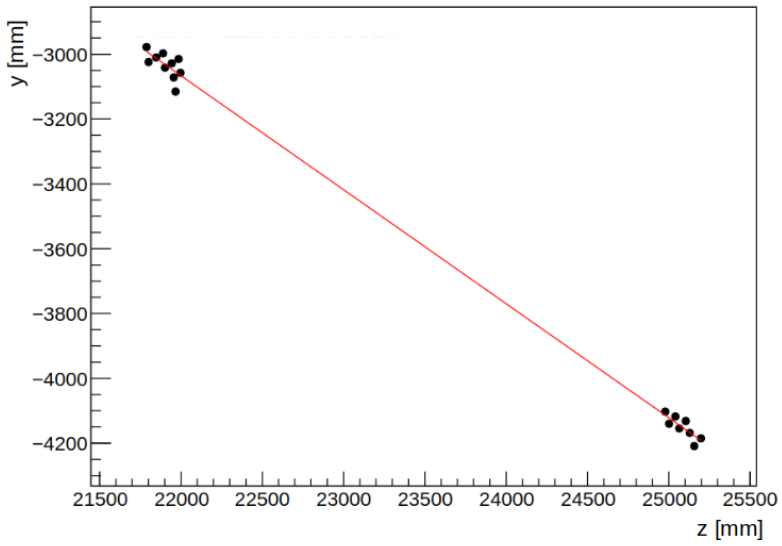

Figure 5.22: Cluster cells y vs z position with linear fit overlayed.

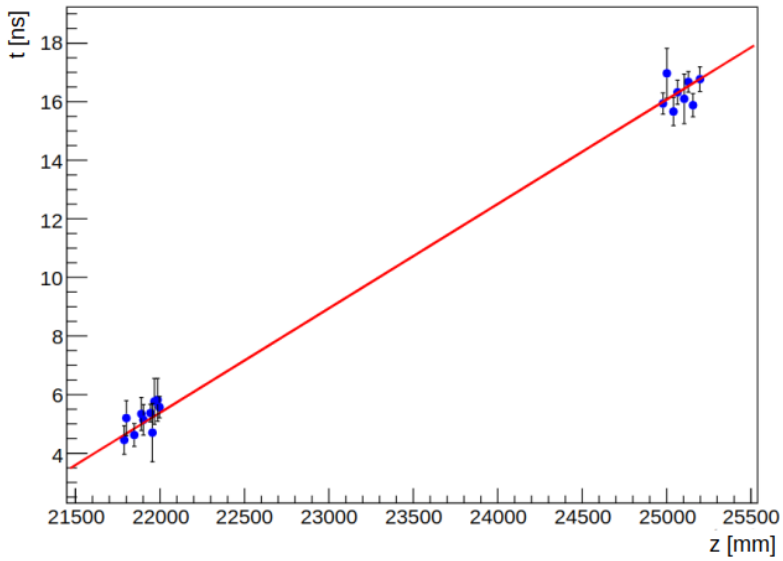

Figure 5.23: Cluster cells t vs. z with linear fit overlaid.

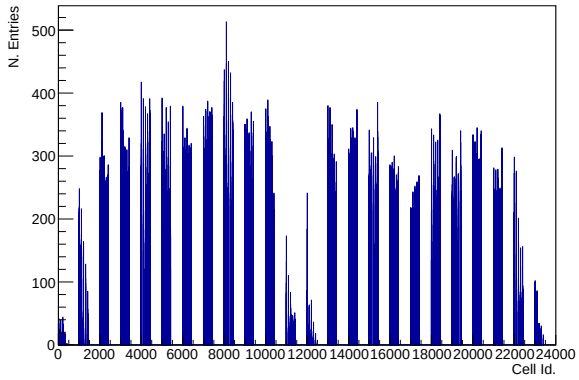

(a) Barrel

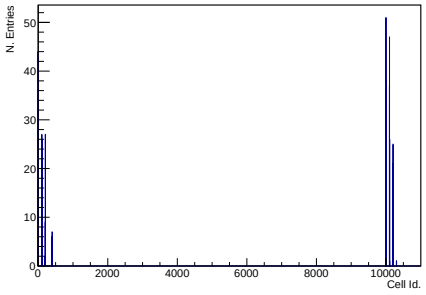

(b) Endcap ($x > 0$)

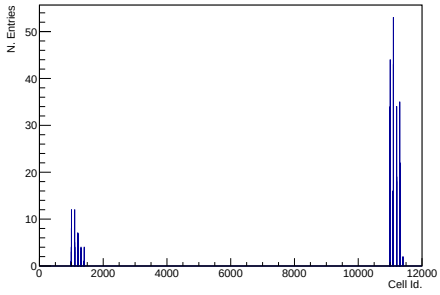

(c) Endcap ($x < 0$)

Figure 5.24: ECAL cell occupancy maps for μ clusters selected by time-calibration cuts. Panels: (a) barrel, (b) endcap $x > 0$, (c) endcap $x < 0$. The x-axis uses the Cell ID notation of 4.4.3 minus the detector ID.

A dedicated C++ procedure analyses the calibration histograms for both t_0 and Δt_0. For t_0, the per-cell residual distributions are fitted with the sum of two Gaussians: a narrow signal component and a broader component accounting for backgrounds (e.g. cells fired by secondaries not aligned with the straight track). The mean of the signal Gaussian is taken as the estimator of t_0. An example for Cell 10, Layer 1 of Barrel Module 18 is shown in Fig. 5.25.

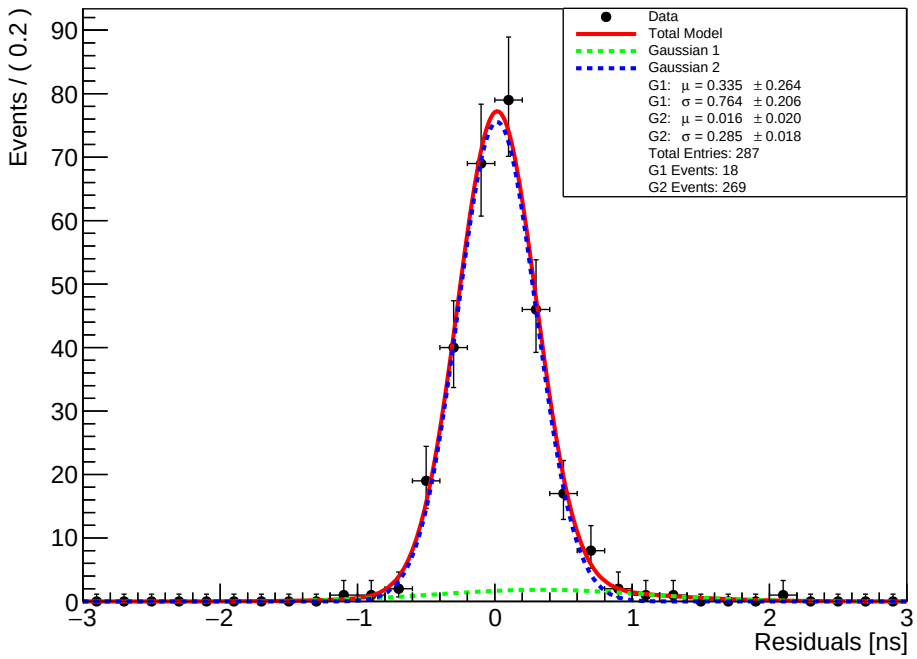

Figure 5.25: Residual distribution for Cell 10, layer 1, in barrel Module 18 with fit overlayed.

For Δt_0, the distribution of $(t_A - t_B)$ in each cell is fitted with a double Fermi-Dirac model implemented in RooFit. The observable is

$$\Delta\texttt{tdc} \equiv t_A - t_B \ \ [\text{ns}],$$

and the probability density is defined as

$$\mathcal{P}(\Delta\texttt{tdc} \,|\, \Delta t_0, L, v_{\text{lfb}}, \tau) = \frac{1}{\left[1+\exp\left(\frac{-\Delta\texttt{tdc}+\Delta t_0-\frac{L}{v_{\text{lfb}}}}{\tau}\right)\right]\left[1+\exp\left(\frac{\Delta\texttt{tdc}-\Delta t_0-\frac{L}{v_{\text{lfb}}}}{\tau}\right)\right]}. \tag{5.8}$$

which corresponds to a uniform window of half-width L/v_{lfb} centered at t_0, with the edge sharpness controlled by τ. In the fit, the module length L is fixed, while t_0 (the center, yielding Δt_0 for the cell) and v_{lfb} (the effective light-propagation speed in the calorimeter) are free parameters; τ is held fixed (here $\tau = 0.5$ ns) to stabilize the fits. The fitted v_{lfb} provides a consistency check against the expected optical propagation speed; parameter estimates and uncertainties are recorded together with the model overlay. An example for Cell 3, Layer 4 in barrel Module 18 is shown in Fig. 5.26.

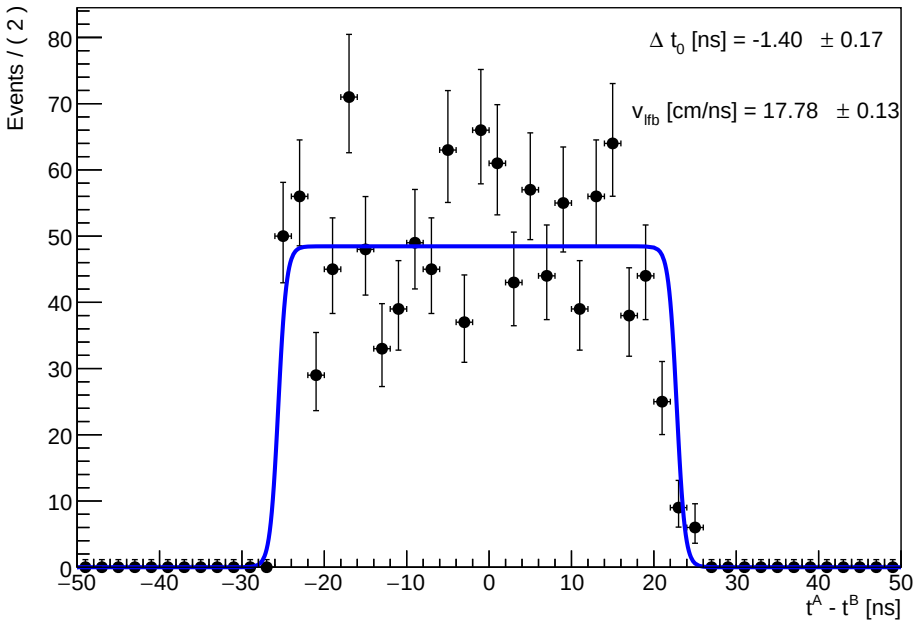

Figure 5.26: TDC difference distribution for Cell 3, Layer 4, in barrel Module 18 with fit overlayed.

Outputs of both timing analyses (fit results, canvases and histograms) are written to the ROOT file in 5.2.2, under a `time/` subdirectory inside each module directory as follows:

```
<root-file>
|-- detX/                        # X = 0,1 for endcaps; X = 2 for barrel
|   `-- moduleYY/                # YY = module ID.
|       `--energy/
|       `--time/
|          `--residual/
|              |-- fitResults/        # Per-cell fit objects
```

```
|             |   `-- fitResult_res_cell_<cellID>
|             |-- canvases/          # Rendered canvases of fits/plots
|             |   `-- res_cell_<cellID>
|             |-- histograms/        # Input histograms used in the fits
|             |   `-- hist_res_cell_<cellID>
|          `--tdcdiff/
|             |-- fitResults/        # Per-cell fit objects
|             |   `-- fitResult_tdcDiff_cell_<cellID>
|             |-- canvases/          # Rendered canvases of fits/plots
|             |   `-- tdcDiff_cell_<cellID>
|             |-- histograms/        # Input histograms used in the fits
|             |   `-- hist_tdcDiff_cell_<cellID>
```

5.3 Global t_0^G

In KLOE, the global time reference is anchored to the DAΦNE radio frequency (RF). The method described in Sec. 5.1.4 selects neutral clusters unassociated with tracks and aligns cluster times to the machine RF after subtracting the time of flight (TOF) from the interaction point defined by the collider interaction region. In SAND, the ν interaction vertex is not fixed; therefore, the evaluation of t_0^G to synchronise the detectors with the spill time information provided by the facility at the production point is not straightforward. Reconstructing the vertex position would allow the evaluation of t_0^G and its alignment to the spill-timing information. This study presents a preliminary procedure to reconstruct the vertex position using only calorimetric information provided by the ECAL, together with its results and associated uncertainties.

The method back-propagates particle flight paths from the cluster apex in the calorimeter by locating the intersection of spheres centered at the cluster apex. It assumes a straight trajectory between the ν interaction vertex and each cluster, with negligible bending in the magnetic field and negligible multiple scattering. As a first attempt, the selection of suitable clusters is based on the truth-matching information described in Sec. 4.6. A sample of 5×10^5 ν_μ interactions in the SAND tracker was produced and processed with the reconstruction chain of Sec. 4.5. For each event, clusters are required (via truth matching) to originate either from photons in $\pi^0 \to \gamma\gamma$ decays at the interaction point or from muons produced at the vertex. Events with at least three such clusters are retained, which is the minimum to define a unique intersection in three dimensions.

As a first geometric seed, the intersection point is estimated in the y-z projection

by minimizing the sum of squared perpendicular distances to the set of cluster-direction lines. Each selected cluster i provides a line in the y-z plane,

$$\ell_i : \; (y, z) \;=\; (y_i^0, z_i^0) \;+\; \lambda\,(d_{y,i}, d_{z,i})\,,$$

where (y_i^0, z_i^0) is the reconstructed apex and $(d_{y,i}, d_{z,i})$ the reconstructed unit direction (projected to y-z). For a trial point (y, z), the perpendicular distance to ℓ_i is

$$d_i(y, z) \;=\; \frac{\left|\,(y - y_i^0)\,d_{z,i} - (z - z_i^0)\,d_{y,i}\,\right|}{\sqrt{d_{y,i}^2 + d_{z,i}^2}}\,.$$

The seed $(\widehat{y}_0, \widehat{z}_0)$ is obtained with least-squares algorithm

$$(\widehat{y}_0, \widehat{z}_0) \;=\; \arg\min_{(y,z)} \sum_i d_i(y, z)^2 \;+\; \lambda\,(y^2 + z^2)\,,$$

with a small Tikhonov term λ to regularise poorly constrained configurations. The optimisation is performed with ROOT's `Fitter` using $(y, z) = (0, 0)$ as the initial guess. The x coordinate is fixed to a reference value x_0 while the y-z seed (y_0, z_0) provides the starting point for the subsequent time-of-flight constrained fit. An illustration of the seed determination in the y–z projection is shown in Fig. 5.27.

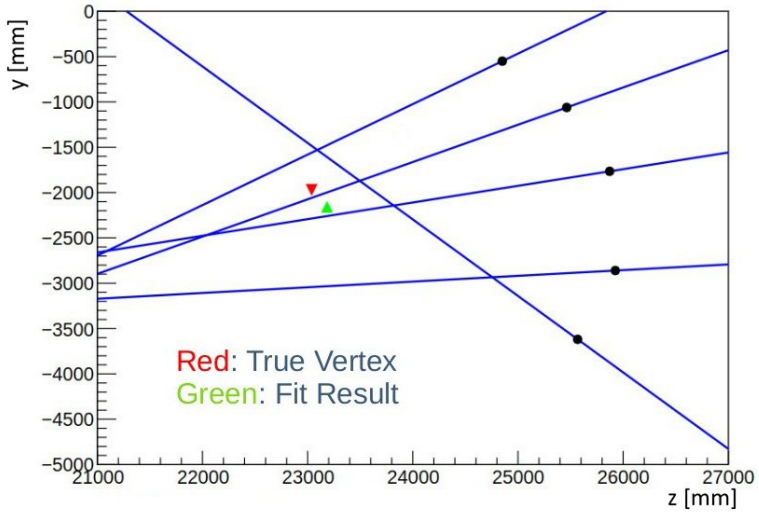

Figure 5.27: Example of the seed determination in the y–z projection. Each selected cluster (black dots) defines a line ℓ_i (blue). The seed $(\widehat{y}_0, \widehat{z}_0)$ is obtained by a least-squares minimization of the sum of squared distances to the set of lines (green marker). The true vertex is shown in red for reference.

The three-dimensional intersection is refined by fitting the vertex as the common origin of considered spheres. The vertex fit proceeds in two stages. Let $\vec{r}_i$ and t_i denote the cluster apex and time for cluster i. The initial guess uses (y_0, z_0) from the 2D line-intersection seed and x equal to the average of the selected apex x coordinates.

Stage 1 (radius alignment to timing): with the intersection fixed at the seed $\vec{r}_0^{\,\text{seed}} = (x_0, y_0, z_0)$, the sphere radii $\{R_i\}$ are adjusted to satisfy the time-difference relation $\Delta R = c\,\Delta t$, minimizing

$$\min_{\{R_i\}} \sum_{i<j} \Big[(R_i - R_j) - c\,(t_i - t_j) \Big]^2,$$

with initial values $R_i^{(0)} = \|\vec{r}_i - \vec{r}_0^{\,\text{seed}}\|$.This quantity does not depend on the global t_0^G and the vertex position, so this stage depends only on measured inter-cluster time differences; the radii are therefore determined up to a single additive constant that will be fixed by the geometric constraint in Stage 2. This yields a set of radii $\{\widehat{R}_i\}$ mutually consistent with the timing differences.

Stage 2 (geometric constraint): keeping the radii fixed to $\{\widehat{R}_i\}$, the intersection point is refined by minimizing the sphere residuals with respect to the free vertex $\vec{r}_0 = (x, y, z)$,

$$\widehat{\vec{r}}_0 \;=\; \arg\min_{\vec{r}_0} \sum_i \Big[\|\vec{r}_i - \vec{r}_0\| - \widehat{R}_i \Big]^2.$$

Both stages are implemented with ROOT's `Fitter`: Stage 1 varies only the radii while holding (x, y, z) fixed at the seed; Stage 2 fixes the radii to the Stage 1 solution and varies (x, y, z). At least three spheres are required; additional clusters improve the solution stability. A result of the sphere intersection fit is presented in Fig. 5.28.

For each reconstructed vertex, the coordinate residuals with respect to the true vertex were evaluated as $r_x = x_{\text{reco}} - x_{\text{true}}$, $r_y = y_{\text{reco}} - y_{\text{true}}$, and $r_z = z_{\text{reco}} - z_{\text{true}}$.The three-dimensional distance $\Delta r = \|\vec{r}_{\text{reco}} - \vec{r}_{\text{true}}\|$ is well described by a Landau function with a broad Gaussian contribution to account for the high-residual tail; the distributions are shown in Fig. 5.29.

The most-probable value of the 3D residual is (275 ± 14) mm.with the reation $\Delta t = \Delta r / c$ to a time uncertainty of $\Delta t \simeq 0.92$ ns, compared to the minimum spill substructure (see Fig. 5.30) time difference of two consecutive bunches $\Delta t \sim 19$ ns. This value provides a first-order estimate for the global spill-synchronization t_0^G error to coarsely synchronise subdetectors, and can be iteratively refined as more precise tracker information becomes aviable.

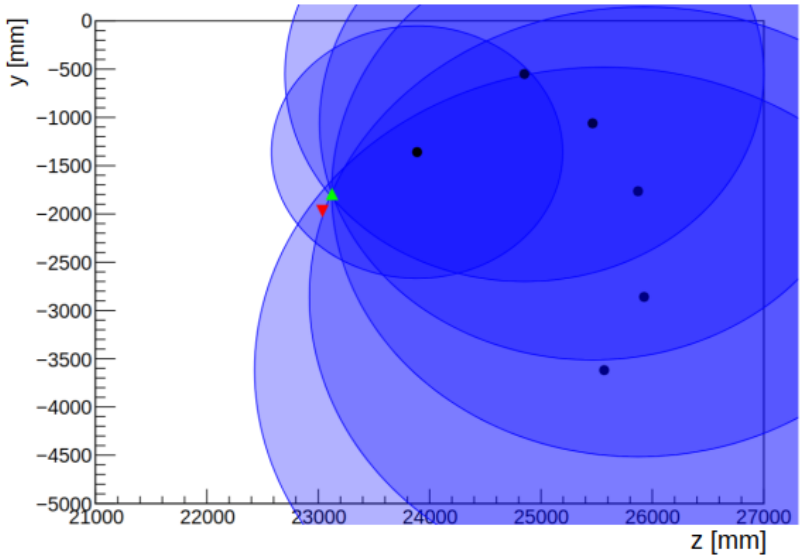

Figure 5.28: Sphere fit result, in red is displayed the true vertex while in green is displayed the sphere fit intersection. The **black points** are the clusters apex used as center of the spheres, in blue are overlayed the spheres.

The same procedure was repeated by selecting clusters generated by any particle except neutrons, in order to assess the degradation when including particles that may bend in the magnetic field or undergo significant scattering. Neutrons were excluded because their interactions often produce irregular topologies -multiple entries and exits from the calorimeter due to scattering- and low-energy, single-cell clusters that violate grossly the straight-line assumption underpinning the method. The resulting coordinate residuals are shown in Fig. 5.31. Compared with the baseline selection, the distributions exhibit heavier and larger tails and are well described by the sum of a Student's t component (to better describe the tail associated with bending or poorly constrained tracks) and a Gaussian core. The three-dimensional residual, fitted with a Landau function, yields a most-probable value of (495.3 ± 2.5) mm, which corresponds to a $\Delta t \approx 1.65$ ns. error on the t_0^G evaluation.

This level of precision for both results is suitable for a coarse initial synchronisation of subdetectors.

To assess the degradation of the method when including particles from ν interactions outside the ECAL, a sample of 3×10^4 ν_μ interactions generated throughout the full SAND volume was produced. The same cluster selections were applied as in the previous case with neutirnos interacting in the SAND tracker volume, namely (i) $\pi^0 \to \gamma\gamma$ and μ from the interaction point, and (ii) an inclusive selection

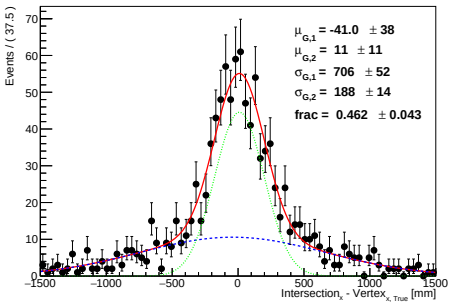

(a) Δx: true vs. sphere-fit vertex. Model: Gaussian 1 + Gaussian 2; total (red).

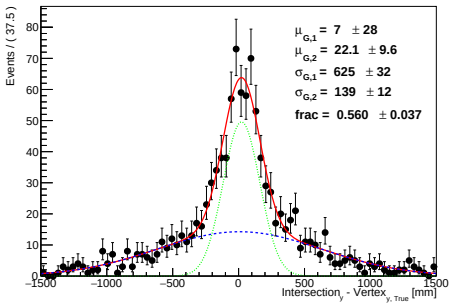

(b) Δy: true vs. sphere-fit vertex. Model: Gaussian 1 + Gaussian 2; total (red).

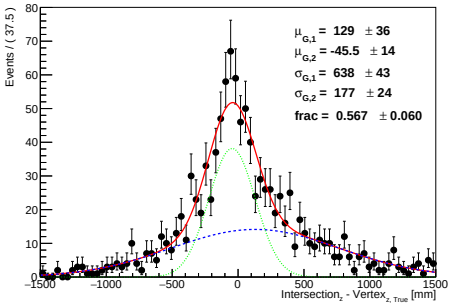

(c) Δz: true vs. sphere-fit vertex. Model: Gaussian 1 + Gaussian 2; total (red).

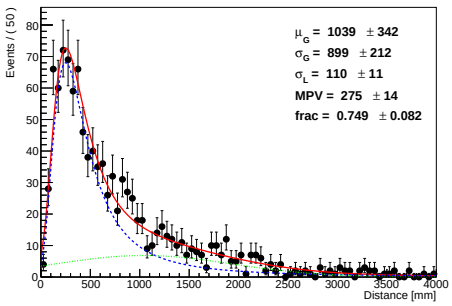

(d) r_{3D}: true-fit 3D distance. Model: Gaussian + Landau; total (red).

Figure 5.29: Residuals between the true interaction vertex and the vertex from the sphere fit for ν_μ interaction in the tracker, selecting only γ from π^0 decay and μ clusters: (a) Δx, (b) Δy, (c) Δz, and (d) 3D distance. The one-dimensional components are modeled as a sum of two Gaussians (green, blue) with total in red; the 3D distance is modeled as a Gaussian (green) plus a Landau (blue) with total in red.

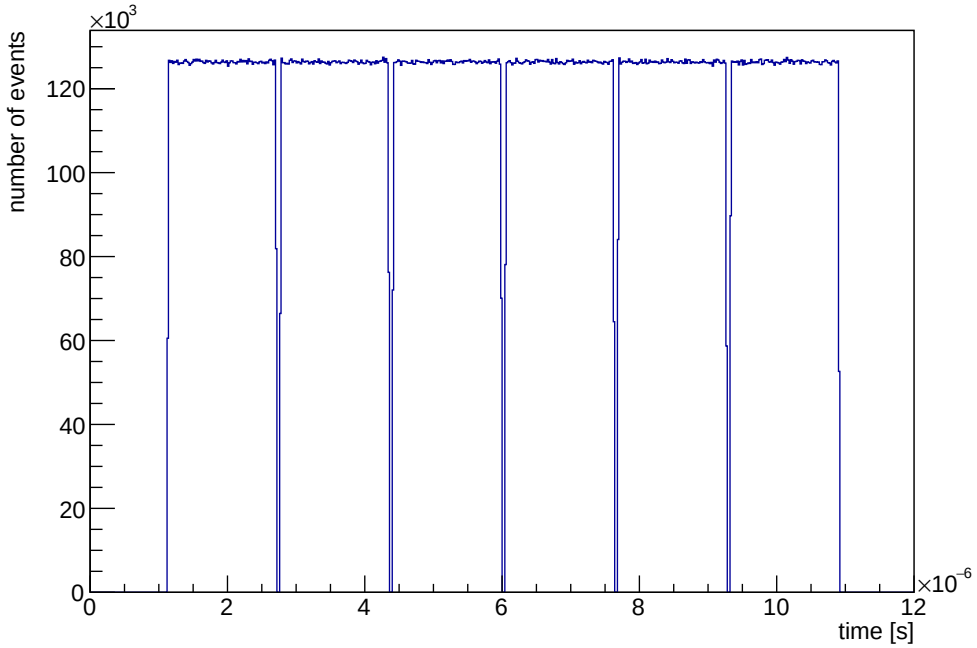

Figure 5.30: DUNE spill profile.

excluding only neutrons. The corresponding residual distributions are shown in Fig. 5.32 and Fig. 5.33, respectively.

As evident from geometric constraints, events with vertices inside the tracker yield better performance: particles traverse less upstream material, trajectories are closer to straight lines, and the selected clusters provide broader angular coverage, all of which stabilize the fit results. When extending to the full SAND volume, the three-dimensional distance residual develops a second component, consistent with a mixture of well-constrained topologies and topologies affected by bending, scattering, or indirect entry into the ECAL. Accordingly, the 3D residual is described by the sum of two Landau functions for both selections.

For the π^0/μ selection the two most-probable values (MPV) are (173 ± 16) mm and (856 ± 57) mm, corresponding to $\Delta t \sim 0.58$ ns and 2.86 ns. For the inclusive-except-neutrons selection the MPVs are (182 ± 15) mm and (780 ± 68) mm, corresponding to $\Delta t \sim 0.61$ ns and ~ 2.60 ns, respectively.

In summary, the ECAL-only vertexing method remains feasible across the studied topologies. Restricting to π^0 photons and through-going muons provides the most favorable conditioning and sub-nanosecond effective timing for the dominant component, while broader selections (still excluding neutrons) introduce a second,

more diffuse population at the few-nanosecond scale. For coarse synchronization a first-guess timing at the $\mathcal{O}$(1-3) ns level is achievable; tighter selections or additional constraints are expected to recover sub-nanosecond performance more uniformly across events.

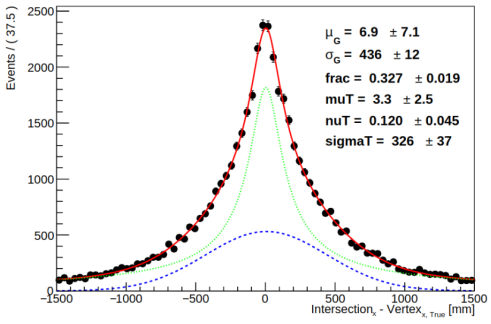

(a) Δx: true vs. sphere-fit vertex. Model: T Student + Gaussian; total (red).

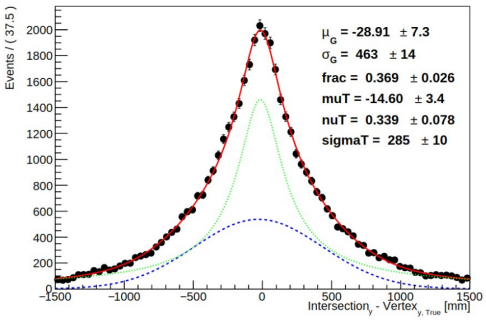

(b) Δy: true vs. sphere-fit vertex. Model: T Student + Gaussian; total (red).

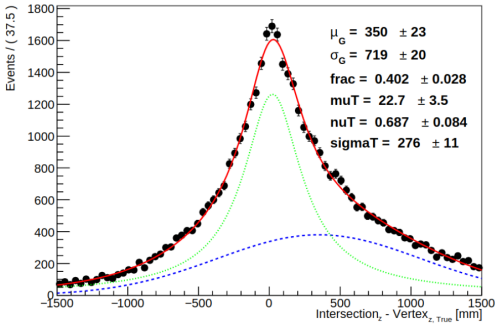

(c) Δz: true vs. sphere-fit vertex. Model: T Student + Gaussian; total (red).

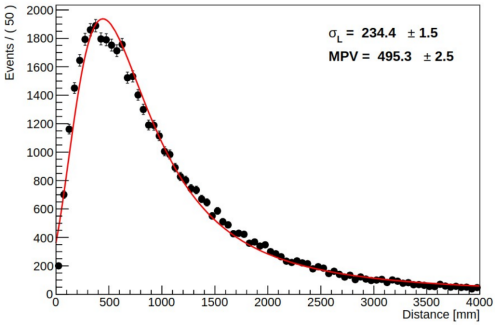

(d) r_{3D}: true-fit 3D distance. Model: Landau.

Figure 5.31: Residuals between the true interaction vertex and the vertex from the sphere fit for ν_μ interaction in the tracker, selecting all but neutron clusters: (a) Δx, (b) Δy, (c) Δz, and (d) 3D distance. The one-dimensional components are modeled as a sum of a T Student and a Gaussian (green, blue) with total in red; the 3D distance is modeled as a Landau.

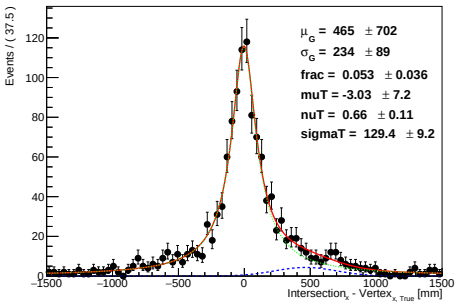

(a) Δx: true vs. sphere-fit vertex. Model: T Student + Gaussian; total (red).

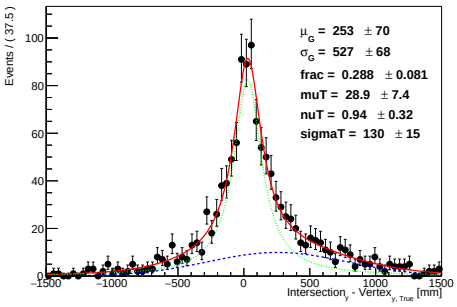

(b) Δy: true vs. sphere-fit vertex. Model: T Student + Gaussian; total (red).

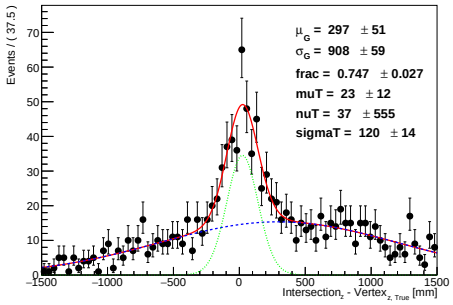

(c) Δz: true vs. sphere-fit vertex. Model: T Student + Gaussian; total (red).

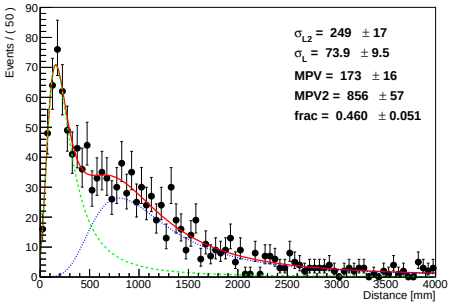

(d) r_{3D}: true-fit 3D distance. Model: Gaussian + Landau; total (red).

Figure 5.32: Residuals between the true interaction vertex and the vertex from the sphere fit for ν_μ interaction in SAND, selecting only γ from π^0 decay and μ clusters: (a) Δx, (b) Δy, (c) Δz, and (d) 3D distance. The one-dimensional components are modeled as a sum of a T Student and a Gaussian (green, blue) with total in red; the 3D distance is modeled as a Landau.

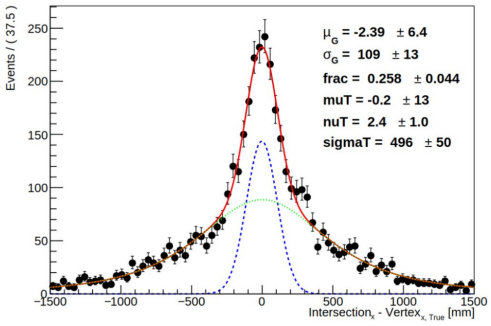

(a) Δx: true vs. sphere-fit vertex. Model: T Student + Gaussian; total (red).

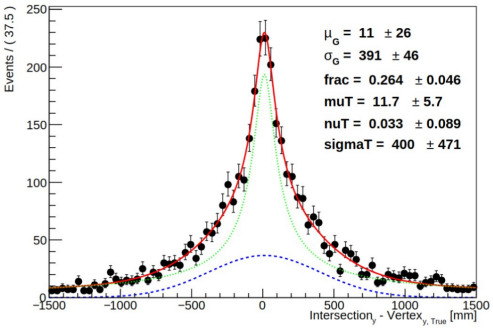

(b) Δy: true vs. sphere-fit vertex. Model: T Student + Gaussian; total (red).

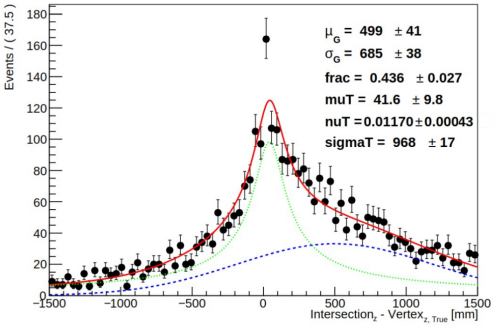

(c) Δz: true vs. sphere-fit vertex. Model: T Student + Gaussian; total (red).

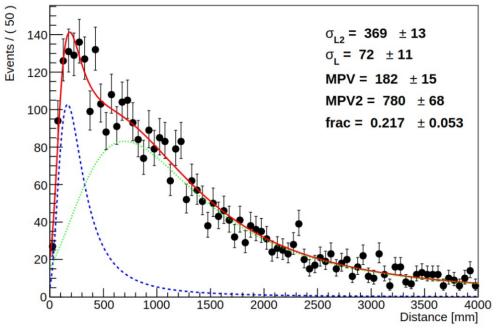

(d) r_{3D}: true-fit 3D distance. Model: Gaussian + Landau; total (red).

Figure 5.33: Residuals between the true interaction vertex and the vertex from the sphere fit for ν_μ interaction in SAND, selecting all but neutron clusters: (a) Δx, (b) Δy, (c) Δz, and (d) 3D distance. The one-dimensional components are modeled as a sum of a T Student and a Gaussian (green, blue) with total in red; the 3D distance is modeled as a Landau.

5.4 Ongoing analyses and future plans

The methodologies presented in this chapter provide a solid foundation for calibration strategies; however, further optimisations are required.

5.4.1 Cosmic-Ray Analysis

The methods discussed in Sec. 5.2, especially the time calibration, suffer from limited statistics in the modules lying in the horizontal plane. These drawbacks could be mitigated by incorporating cosmic muons. Although the underground cosmic-ray flux is significantly lower than at the surface it may still be sufficient to compensate for the low population in the aforementioned modules. A dedicated cosmic-ray simulation within the DUNE production framework is not currently aviable; a comprehensive study of the underground cosmic-ray flux is therefore needed to assess whether it can be integrated effectively with the rock-muon methodology.

5.4.2 Global t_0^G

The method of Sec. 5.3, as formulated, is most challenged by events whose vertex lies outside the ECAL. To identify such topologies, a subset of the 3×10^4 ν_μ interactions used in Sec. 5.3 was selected by requiring clusters with at least one cell in each ECAL layer. For events with vertices inside the ECAL volume (i.e. in the Tracker or in GRAIN), clusters are expected to exhibit a time evolution from the innermost to the outermost layer. Accordingly, the distribution of $\Delta t \equiv t_{\text{outer}} - t_{\text{inner}}$ was studied for the selected clusters in each vertex region, as shown in Fig. 5.34.

Events with vertices in GRAIN or in the Tracker display a Δt distribution peaked at approximately $+0.8$ ns. In contrast, events with vertices outside the ECAL volume exhibit a bimodal structure, with peaks near -0.7 ns and 0.8 ns. This behaviour is consistent with particles traversing both sides of the calorimeter and producing clusters with time topologies characteristic of both "inside" and "outside" interactions.

To suppress outside-ECAL topologies, a conservative cut was applied on the cluster-level variable, discarding events that contain at least one cluster with $\Delta t < -0.5$ ns. This threshold accounts for resolution and smearing effects while removing the majority of outside-ECAL events; the resulting impact per region is reported in Table 5.2. The efficiency loss for genuine Tracker and GRAIN vertices is approximately 10%.

Further and more precise studies are required to refine the global t_0^G, including the integration of tracker information and improved rejection of events originating outside the ECAL.

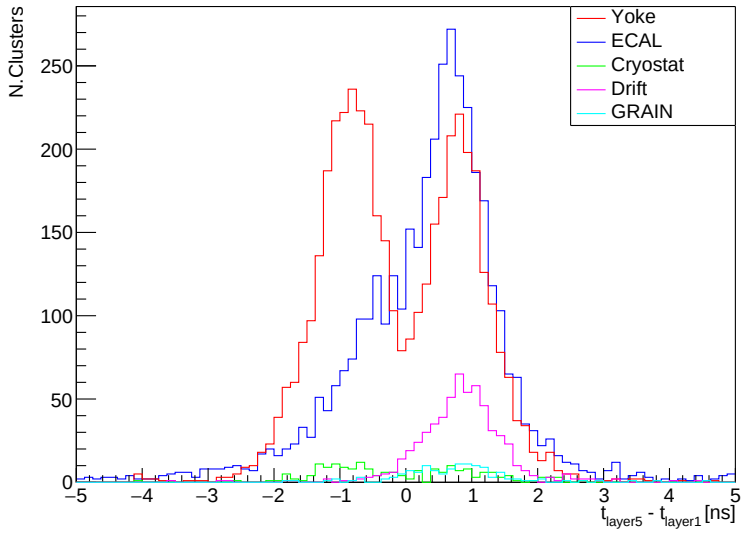

Figure 5.34: Δt distribution between layer 4 and 0 for events selected in different regions of SAND.

Region	Selected	After $\Delta t < -0.5$ cut	Kept [%]
Yoke	2609	471	18.1
ECAL	2686	1535	57.2
Cryostat	99	13	13.1
GRAIN	80	69	86.3
Tracker	408	364	89.2

Table 5.2: Number of event selected with at with at least 1 cell in each layer, an event is discarded if it has at least 1 cluster with $\Delta t < -0.5$ ns .

5.4.3 Spill simulation

The validation sample employed thus far consists of ν_μ interactions generated without a beam-spill simulation; consequently, inter-spill pile-up is absent and all clusters within an event originate from a single neutrino interaction.

At the time of this analysis, an official spill simulation is not aviable in the DUNE ND simulation. To emulate the spill structure in a preliminary manner, a dedicated ν sample was produced in which, for each event, a common time offset

was assigned to all clusters by random sampling from the spill-time distribution (Fig. 5.30). The resulting one-dimensional distribution of cluster times exhibits event-wise peaks (Fig. 5.35a); nonetheless, partial overlaps between temporally adjacent events can occur.

To mitigate such overlaps, the joint time-position pattern of particles in the ECAL can be exploited. In the two-dimensional distribution of cluster time versus cluster z (Fig. 5.35b), clusters from a single interaction align in bands approximately perpendicular to the time axis, offering a discriminant for separating contemporaneous events. A quantitative assessment of this method requires a realistic spill simulation within the full simulation chain and an optimization of the band-selection parameters, which are deferred to future work alongside the integration of the spill model into the global-t_0 estimator.

5.4.4 Absolute energy scale

Lastly, a strategy to determine the absolute energy scale remains to be developed. As discussed in Sec. 5.1, this requires a calibration sample with known energy. A plausible option in SAND is the $\pi^0 \to \gamma\gamma$ decay produced at neutrino interaction vertices. A dedicated feasibility study is therefore required to evaluate this approach, including the expected occurrence rate, selection purity, reconstruction biases, and systematic uncertainties. Alternative calibration channels suitable for this purpose, such as $K_S \to 2\pi^0$ should also be surveyed and compared in terms of statistical reach and control of systematics.

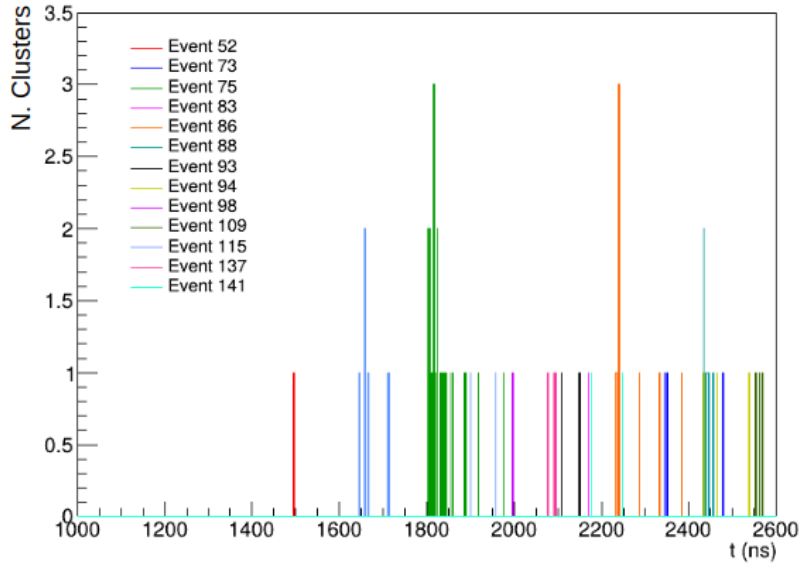

(a) Clusters time gated distribution.

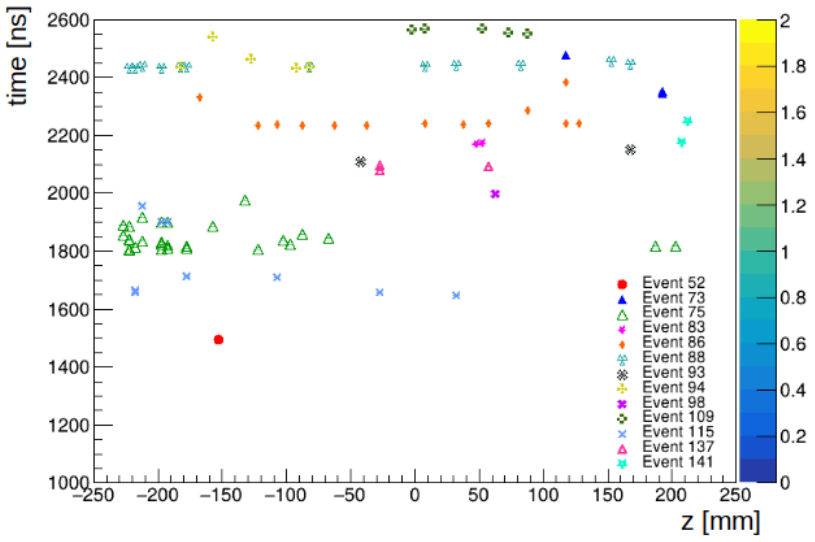

(b) Clusters time gated distribution vs z.

Figure 5.35: Cluster time gated distributions: (a) One dimentional distribution of cluster events, bins of the same color belong to the same event. (b) Cluster time gated vs z, the value of z has been translated to the center of SAND. Points of same symbol and color belong to the same event. Both plots are restricted for the first 10^3 ns of the spill profile

5.5 Cosmic-Ray Stand for ECAL Module Performance Studies at LNF

As a complementary activity to the calibration studies performed within the SAND framework, a dedicated cosmic-ray stand has been developed at the Laboratori Nazionali di Frascati (LNF) to assess the performance of individual ECAL modules prior to their installation in the detector. While the calibration procedures based on reconstructed rock-muon events evaluate the detector response under realistic operational conditions and reconstruction algorithms, the cosmic-ray stand provides direct measurements of the hardware response in a controlled environment, allowing a precise characterization of the intrinsic behaviour of the modules and their commissioning before ECAl installation at Fermilab.

The system enables the acquisition of signals produced by cosmic muons crossing the modules under test, allowing the measurement of their Analog-to-Digital Converter (ADC) and Time-to-Digital Converter (TDC) responses. This work constitutes a necessary step to verify the functionality and stability of the modules and associated readout chain before their integration in the final setup, and it also serves as an independent measurement of their expected performance. Even though the acquisition conditions differ from those in the SAND detector, the spectra obtained from cosmic muons are expected to exhibit the same characteristic shape as those produced by simulated rock-muon minimum-ionizing particles, both in the ADC and TDC distributions, allowing a direct comparison between experimental and simulated results.

This section presents an overview of the preliminary experimental setup and readout electronics, followed by a description of the acquisition software and the analysis of the resulting ADC and TDC spectra used to evaluate the module performance.

5.5.1 Experimental Setup and Readout Electronics

The cosmic-ray stand is equipped with a trigger system based on the coincidence of the four photomultiplier tubes (PMTs) coupled to two plastic scintillator paddles of dimensions ($69 \times 13 \times 3$ cm), one positioned above and one below the ECAL barrel module under test. The coincidence logic ensures the selection of cosmic muons crossing the module volume. A picture of the experimental setup is shown in Fig. 5.36.

The PMT signals of the paddles are processed through a chain of CAEN NIM modules that handle the signal discrimination, coincidence logic, and timing con-

Figure 5.36: Picture of the cosmic-ray stand at LNF used for ECAL module performance studies. The setup consists of two scintillator paddles operated in coincidence to provide the trigger for a single ECAL barrel module, which is read out through the dedicated front-end and acquisition electronics.

trol. The analog outputs from the four PMTs are first sent to a CAEN six-channel low-threshold discriminator (Mod. N224), which converts the analog pulses into standard NIM logic signals. These logic outputs are then fed to a CAEN dual programmable logic unit (Mod. 81A), which forms the coincidence trigger among the four discriminator channels corresponding to the top and bottom scintillators, shown in Fig. 5.37. The coincidence signal is subsequently sent to a CAEN dual timer (Mod. 2255B), which produces a continuous high-level signal delayed by approximately 100 ns to align the ECAL PMT signals and trigger timing before being transmitted to the VME system. The trigger formation logic and the corresponding timing alignment are illustrated in Fig. 5.38.

The delayed trigger is received by the CAEN VME bridge (Mod. V3718), shown in Fig. 5.39, which controls the digitization sequence of the ADC and TDC boards and interfaces the readout electronics with the laboratory control computer running the dedicated data acquisition (DAQ) software described in Sec. 5.5.2. The DAQ program reads the multi-event FIFO buffers of the ADC and TDC modules upon the arrival of each trigger and, once the readout is completed, signals the trigger dual timer to reset the high level, allowing the system to wait for the next coincidence event.

The ECAL barrel module under test is powered by low- and high-voltage power

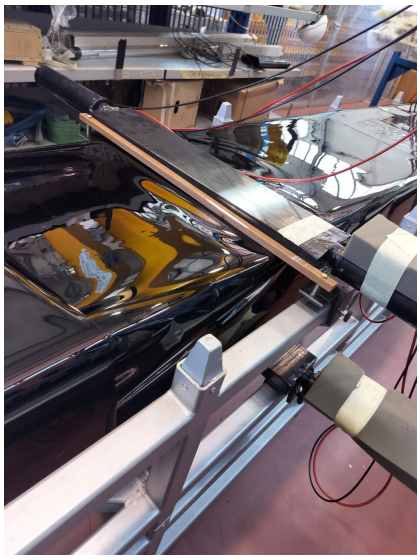

Figure 5.37: Picture of the scintillator paddles employed to form the top–bottom coincidence for the cosmic-ray trigger. Each paddle is read out by two PMTs, one on each side, providing four discriminator channels in total.

(a) Trigger logic.

(b) Trigger delay alignment (100 ns).

Figure 5.38: Trigger formation and timing alignment used in the cosmic-ray stand.

Figure 5.39: CAEN VME bridge (Mod. V3718) interfacing the trigger signals and digitizers to the laboratory control computer running the DAQ software.

supplies. The high voltage provided by a CAEN SY527 universal multichannel power system, shown in Fig. 5.40,providing an independent high voltage channel to each PMT.

The PMT signals are discriminated by using custom SDS boards [56] with constant fraction discriminators, and sent to the ADC and TDC boards implementing the KLOE readout architecture. Both ADC and TDC boards are based on 9U, 400 mm deep VME boards (CAEN Mod. VX559/VX569) [56], 30 channel each. Pictures of the ADC and TDC boards used in the setup are shown in Fig. 5.41. The TDCs work in common start mode. The stop signals are delayed by 220 ns with a mono-stable to accommodate the trigger formation time.

The trigger system produces two signals: T1, a prompt signal that initiates digitization after a fixed dead time of 2 μs, and T2, which controls the digital readout sequence, transferring data to the FIFO memory with possible ADC pedestal suppression. Each FIFO consists of a header FIFO, which stores the trigger number and number of active channels, and a data FIFO, which contains the digitized values, baseline and overflow flags, and encoded channel information. For the operation of a single ECAL barrel module, four ADC and four TDC boards are employed. Each board is identified by an hexadecimal address that can be manually set and changed in the board electronics configuration, as illustrated in Fig. 5.42. A schematic overview of the Cosmic Ray Stand is shown in Fig. 5.43.

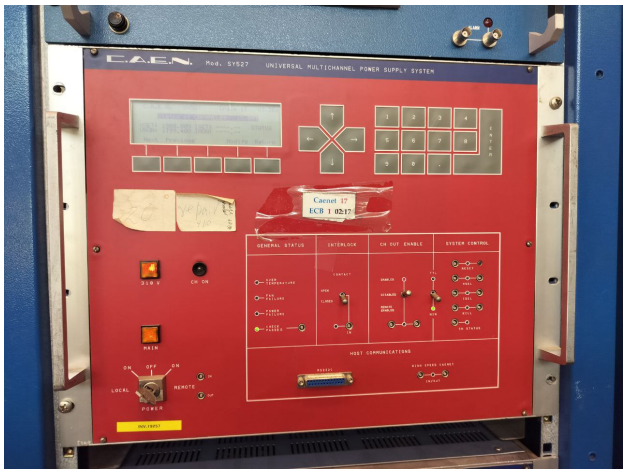

Figure 5.40: CAEN SY527 universal multichannel high-voltage power supply used to bias the PMTs of the ECAL module under test.

(a) ADC boards (VX559).

(b) TDC boards (VX569).

Figure 5.41: KLOE ADC and TDC VME boards used in the readout chain.

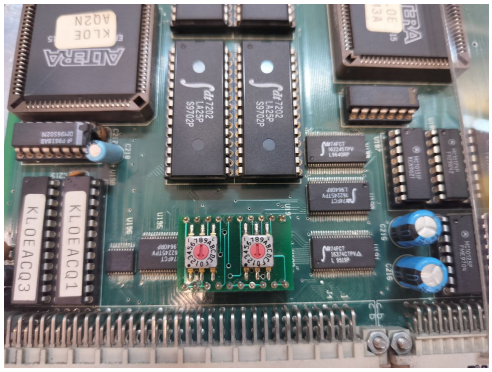

(a) Board address configuration.

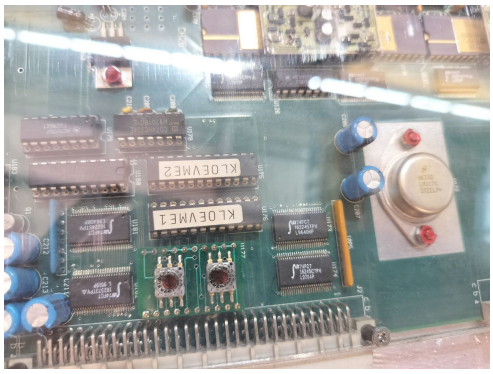

(b) Board address configuration.

Figure 5.42: Examples of hexadecimal address settings for the VME digitizer boards.

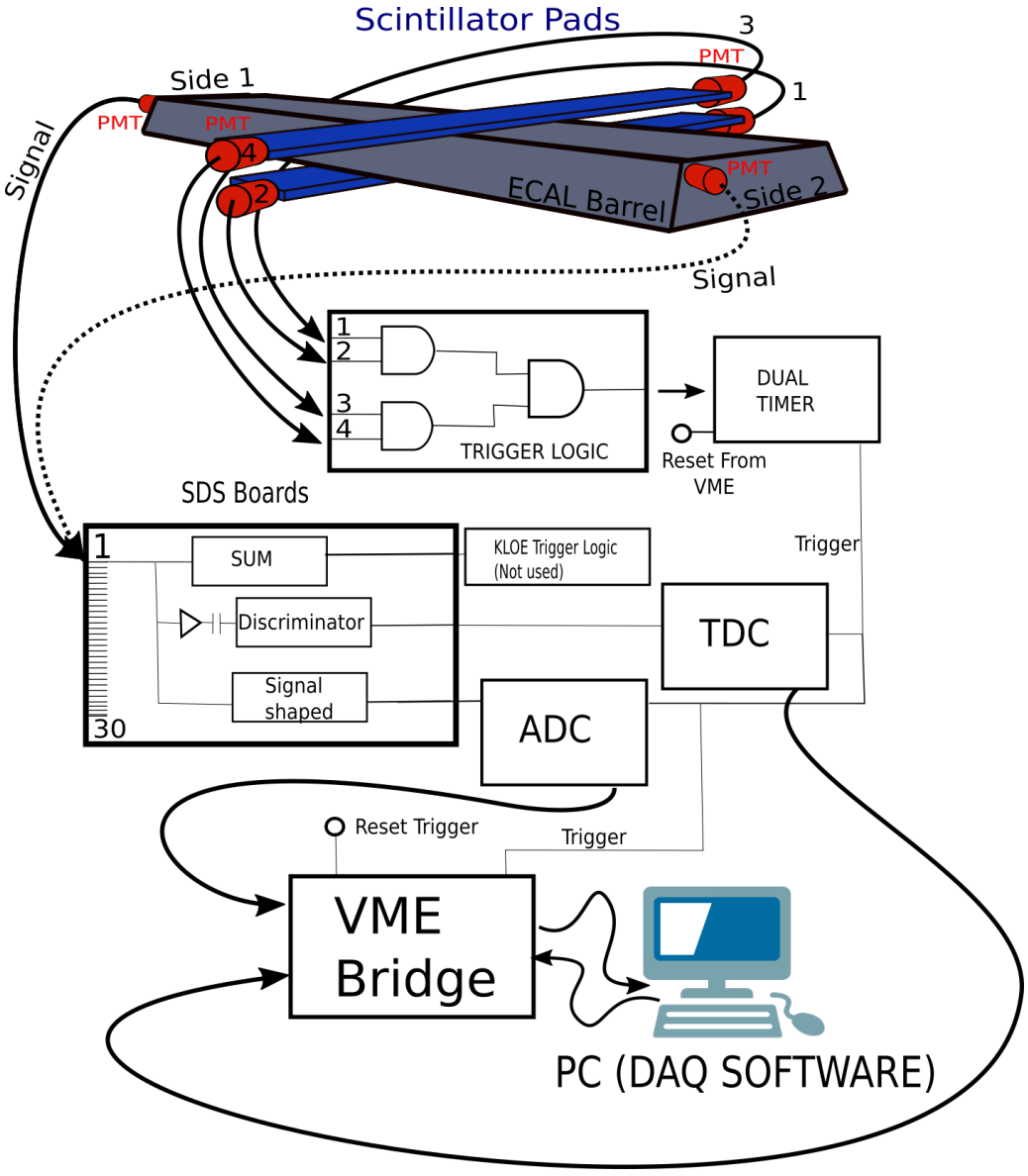

Figure 5.43: Scheme of the cosmic-ray stand.

5.5.2 Data Acquisition Software and Operation

The data acquisition (DAQ) software developed for the cosmic-ray stand setup is based on the CAENDemo framework designed for the CAEN VME bridge controllers and makes extensive use of the functions provided by the CAENVMELib library [66]. The program, written in `C`, provides complete control of the VME communication layer and manages the initialization, configuration, and readout of the ADC and TDC modules used in the setup. While the original CAENDemo environment is primarily intended for manual operation and debugging of the VME bus, it has been extended in this work through a dedicated interface library to perform fully automated data acquisition and storage.

The DAQ application is structured to allow flexible run configurations. At startup, the software initializes the connection with the VME bridge, verifies the presence of the digitizer boards, and loads the predefined addresses of the modules. The user can select the acquisition mode, specifying whether the run should be limited by time or by the number of recorded events, and whether the readout should involve a single board or the full set of connected ADC and TDC modules. The software then launches the acquisition process, which operates in a multithreaded architecture when several boards are active, assigning one thread to each module to enable parallel readout. The program checks the connection on the selected boards and proceeds with the acquisition step if no errors are detected.

During operation, the DAQ continuously monitors a digital input of the VME bridge (Mod. V3718) to detect the arrival of a trigger signal. When a trigger is registered, the software executes the readout sequence: the FIFO buffers of the active digitizers are accessed through the VME interface, and the raw data words are decoded to extract the relevant information. Each word contains the encoded channel number, the digitized value, and status flags such as overrange bits. The information are temporarily stored in memory, after which the buffers are cleared to prepare for the next event. Once all boards complete their readout, the event data are organized by board, channel, and event identifier and written to disk in a comma-separated value (CSV) format. Each trigger corresponds to a single recorded event. After data writing, a reset command is issued through the VME bridge to the timing module, re-arming the system for the next trigger, as described in Sec. 5.5.1.

A schematic representation of the acquisition workflow is shown in Fig. 5.44. The implemented framework provides a stable and modular tool for operating the cosmic-ray stand, ensuring reliable synchronization between trigger signals and digitizer readout, while maintaining full compatibility with the standard CAEN VME control interface.

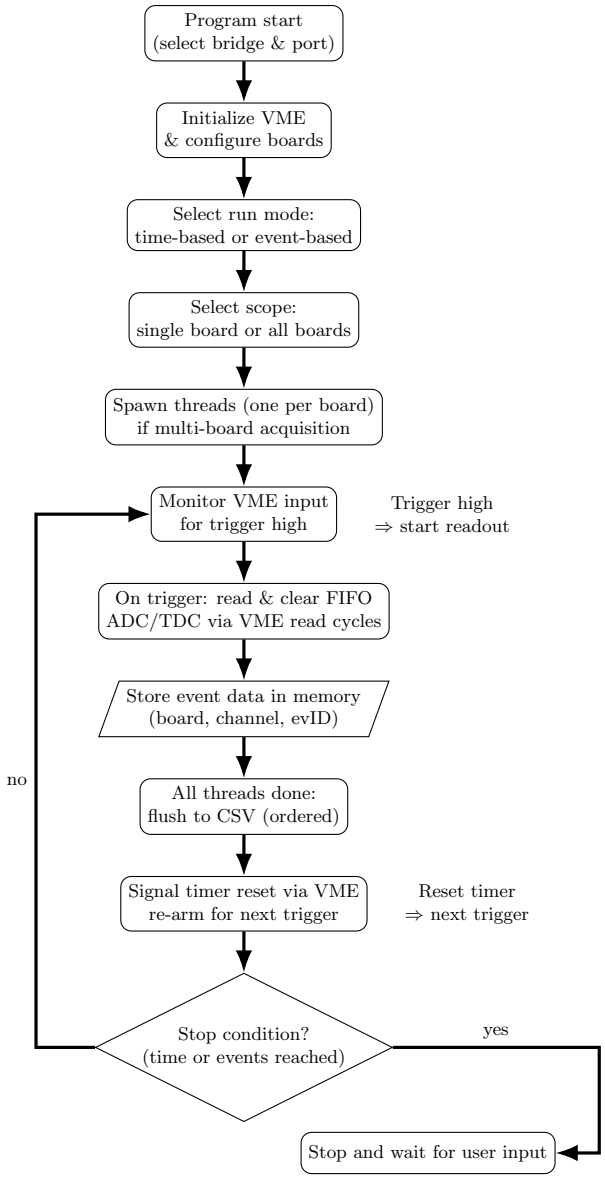

Figure 5.44: Data acquisition (DAQ) flow for the cosmic-ray stand. The software initializes the VME connection and board configuration, monitors the trigger line on the VME bridge, reads and clears the FIFO of each selected ADC/TDC board (in parallel threads if multi-board mode is enabled), stores event data in memory, flushes ordered data to CSV, and resets the timer to re-arm the trigger. The loop continues until the selected stop condition (time or event count) is reached.

5.5.3 Data Analysis and Preliminary Results

The data presented in this section were acquired testing barrel module 5 of the ECAL, corresponding to 120 photomultiplier tubes (PMTs) — 60 per side — read out through four ADC and four TDC boards operating in parallel, as described in Sec. 5.5.2. The acquisition was performed over a total duration of approximately 28 hours of continuous cosmic-ray data taking. Examples of the resulting ADC and TDC spectra obtained from the acquisition are presented in Figs. 5.45–5.51.

Although the FIFO digitizer boards include a hardware ADC pedestal subtraction feature, its use requires the prior determination of the pedestal level through a dedicated trigger configuration, which will be implemented in the future. Consequently, the ADC spectra are presented without the pedestal subtraction. A representative example of an ADC distribution for one PMT channel is shown in Fig. 5.45. The spectrum exhibits three distinct components: a Gaussian pedestal peak, a right-hand tail associated with low-energy background, and the Landau-like peak corresponding to minimum-ionizing particles (MIPs). The tail on the right of the pedestal reproduces the same background component observed in the simulated rock-muon sample discussed in Sec. 5.2.2, corresponding to particles that do not traverse the full length of the calorimeter cell, thereby providing a qualitative validation of the simulation.

To model these spectra, the expected composition would include a Gaussian function for the pedestal, a Crystal Ball function to describe the asymmetric tail, and a Landau distribution convoluted with a Gaussian to represent the MIP signal. However, since the pedestal and background components overlap significantly, a satisfactory description was obtained by fitting the distribution with a Landau-Gaussian function for the MIP signal and a double-sided Crystal Ball for the combined pedestal and tail. The resulting fit for a specific channel is shown in Fig. 5.45, where the dashed red line represents the pedestal and background component and the dashed blue line the MIP signal. The corresponding ADC correlation plots between the two sides (S1 and S2) of the cell is shown in Fig. 5.46.

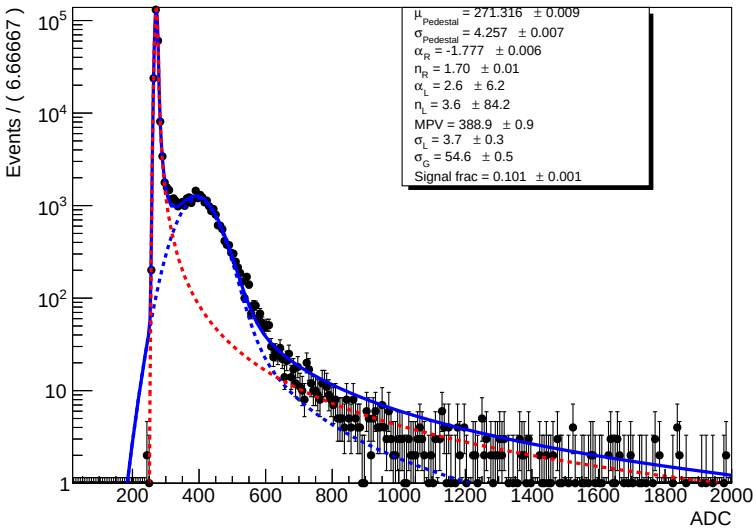

Figure 5.45: ADC spectrum (including pedestal) for side-1 PMT of barrel module 5, cell at column 8 and layer 4, with fitted components. The dashed red line represents the pedestal and background contribution, while the dashed blue line corresponds to the MIP signal.

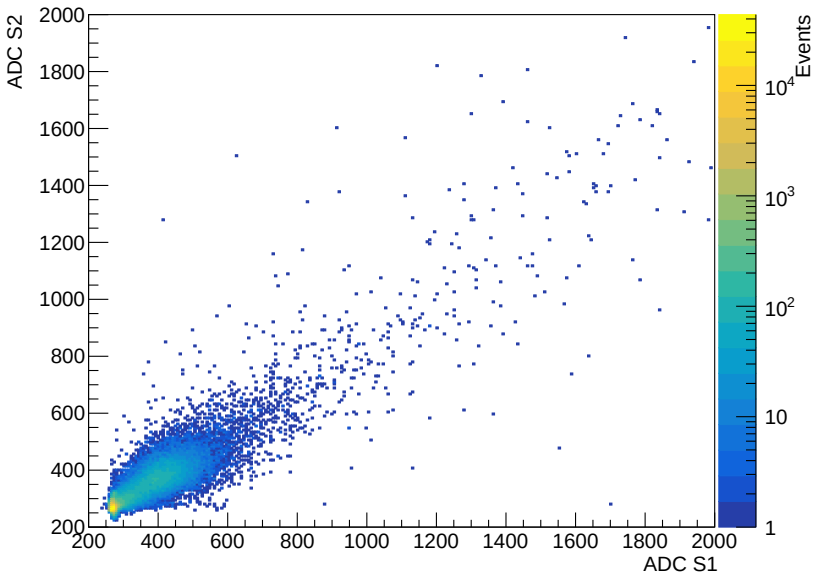

Figure 5.46: ADC correlation plot of cell at column 8 and layer 4 for barrel module 5.

After fitting all ADC spectra, the pedestal values were extracted individually for each channel, pedestal distribution is presented in Fig. 5.47. These values were subsequently used to identify events corresponding to crossing muons producing "Golden MIPs", which are used for the performance study and calibration of the module. For each event, if all cells in a given column recorded an ADC value exceeding five standard deviations above its fitted pedestal value, the event was tagged as a Golden MIP. The corresponding ADC distributions for these selected events were then accumulated and fitted, after pedestal subtraction, as shown in Fig. 5.48. The distribution of the MPV fit results for all the channels is shown in 5.49.

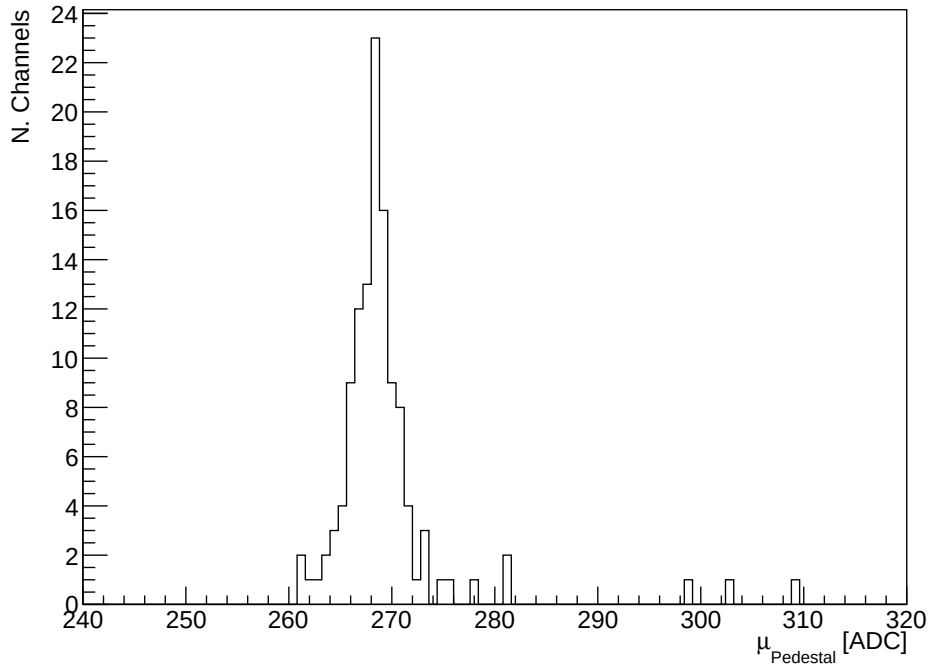

Figure 5.47: Pedestal distribution for the ADCs channels.

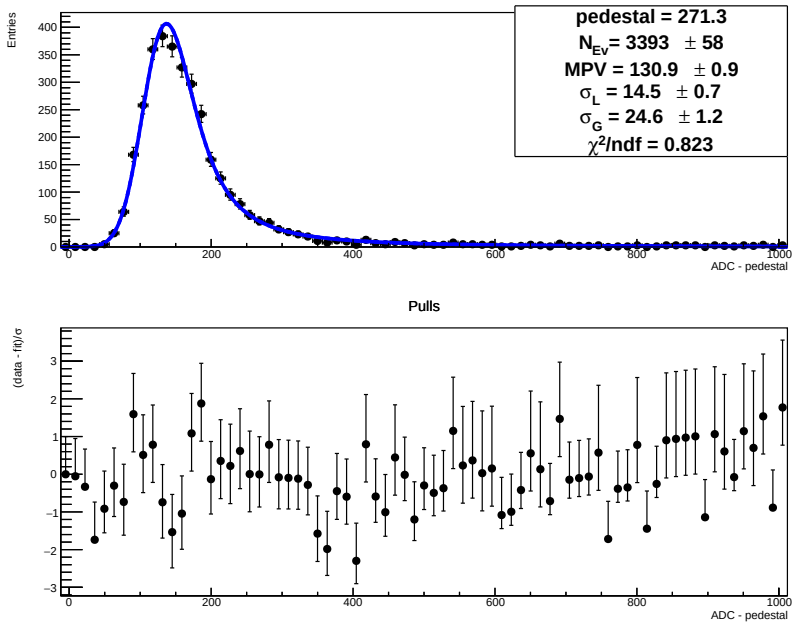

Figure 5.48: ADC spectrum (after pedestal subtraction) for Golden MIPs for side-1 PMT of barrel module 5, cell at column 8, layer 4, with fit overlay and pull distribution.

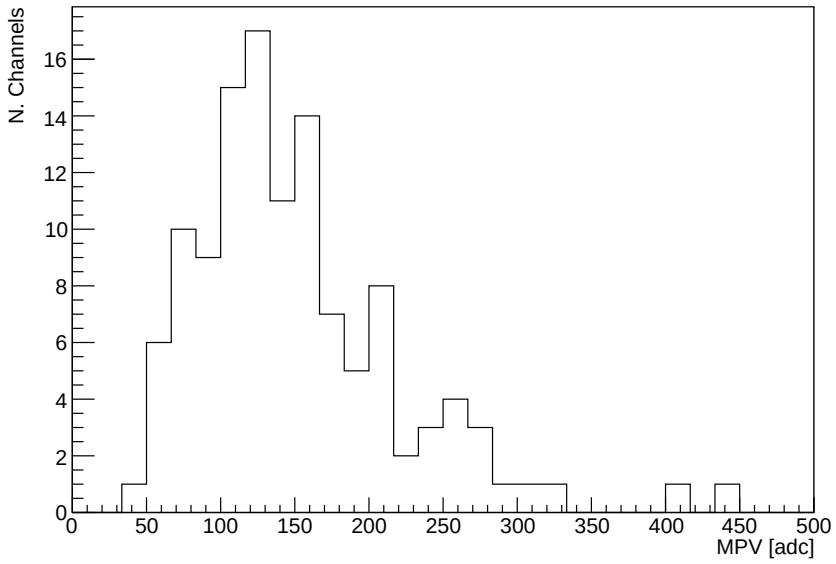

Figure 5.49: MPV distribution for the ADC Golden MIPS spectrum of all channels in barrel 5.

Alongside the ADC signals, TDCs were acquired as well. The TDC spectra presented in Fig. 5.50 correspond to the cell located at column 9 and layer 2 of barrel module 5. The two distributions show the timing information from the PMTs placed on opposite sides of the module. The relative timing between the trigger and signal has been optimised. The setting of the discriminator timing thresholds of the individual readout channels will be required as part of the full time calibration procedure.

The corresponding ΔTDC distribution, shown in Fig. 5.51, is peaked around -188 TDC counts, consistent with the offset observed in the individual TDC spectra. Given the intrinsic TDC sensitivity of 53 ps per count [56], this offset corresponds to a relative timing difference of approximately $\Delta t_0 \simeq 10$ ns.

Furthermore, the ΔTDC spectrum exhibits a single narrow peak rather than the rectangular profile expected when the trigger covers the full length of the module, as observed in the time-calibration study of Sec. 5.2.3. This difference arises because the current trigger configuration is corresponds to a small region delimitated by the scintillator paddles. A preliminary investigation of the module time response was performed by varying the trigger position along the longitudinal axis of the barrel. The trigger paddles were successively placed at 166 cm , 83 cm, 0 cm (center), -83 cm, and -166 cm from the midpoint of the module, negative distances corresponding to displacements toward side 1 and positive ones toward side 2.The resulting ΔTDC distributions for the different trigger positions are shown in Fig. 5.52, where each peak has been fitted with a Student-t model to determine the mean value. The fitted peak positions are summarized in Table 5.3. A clear linear dependence of the peak position on the trigger displacement is observed, consistent with the expected signal propagation along the module. By converting the fitted ΔTDC peak positions into time units and performing a linear fit of the measured time difference as a function of the trigger position (z) along the module, a preliminary estimate of the effective light propagation velocity in the fibers was obtained. The resulting fit is shown in Fig. 5.53. From the slope of the linear function, the effective light velocity v_{vlfb} is derived as

$$v_{\mathrm{lfb}} = \frac{2}{\mathrm{slope}} = \frac{2}{0.1192 \pm 0.00001} = (16.778 \pm 0.001)\ \mathrm{cm/ns}. \tag{5.9}$$

Trigger position [cm]	μ_{peak} **[TDC counts]**
166	183.54 ± 0.03
83	1.24 ± 0.05
0	-188 ± 1
-83	-373.61 ± 0.07
-166	-561.66 ± 0.03

Table 5.3: Fitted peak positions of the ΔTDC distributions for different trigger positions along the barrel module. Negative displacements correspond to shifts toward side 1.

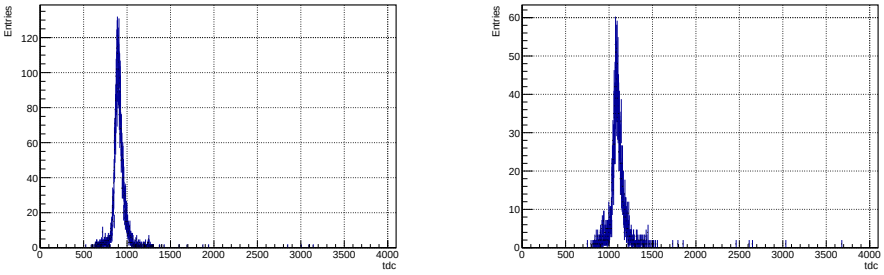

(a) Side-1 PMT.

(b) Side-2 PMT.

Figure 5.50: TDC spectra for the PMTs of barrel module 5, cell at column 9 and layer 2, with trigger positioned at the center of the module.

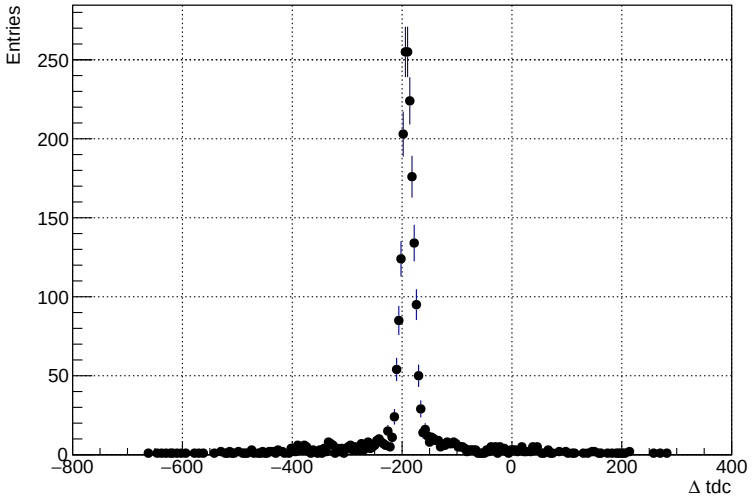

Figure 5.51: ΔTDC distribution for barrel module 5, cell at column 9 and layer 2 with trigger at the canter of the module.

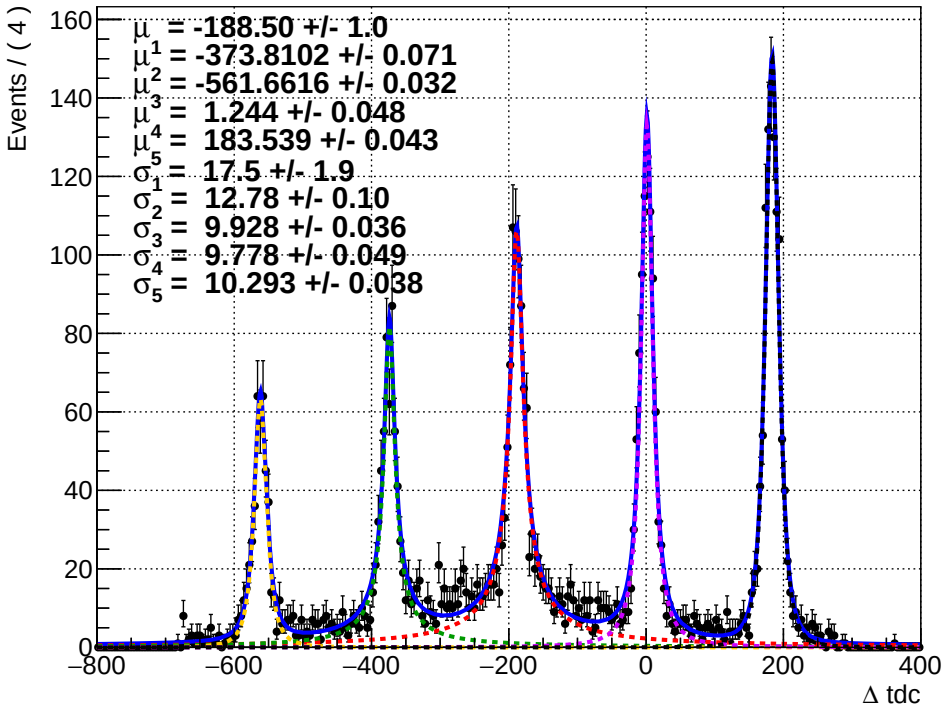

Figure 5.52: ΔTDC distribution for barrel module 5, cell at column 9 and layer 2 for different trigger positions.

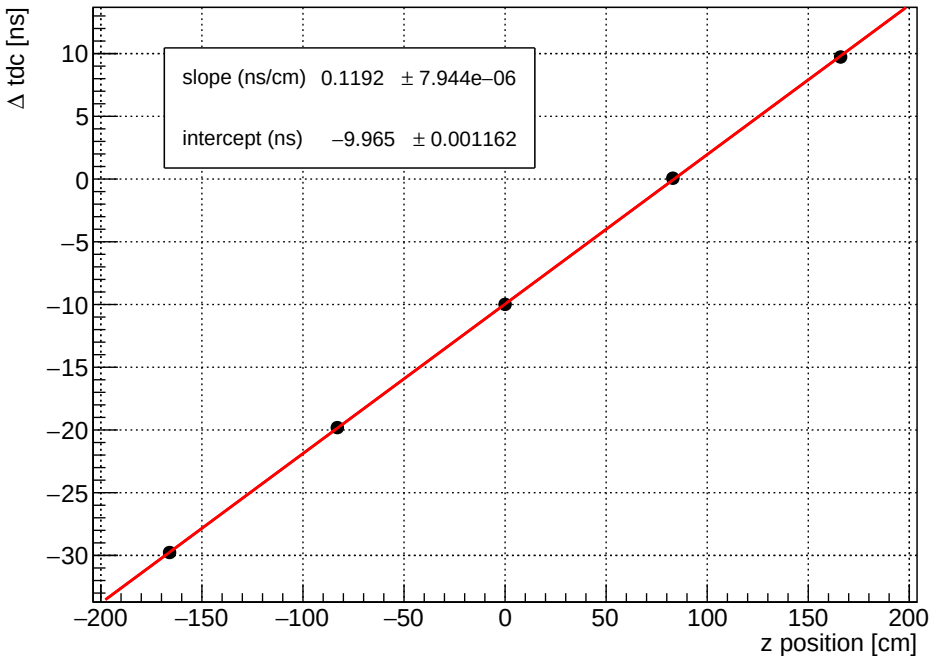

Figure 5.53: Δt vs z position along the module with linear fit overlayed.

In conclusion, while the cosmic-ray stand is still in its commissioning phase, these measurements already demonstrate the capability of the setup to mesure the detector performance. Future developments will include an improved trigger logic based on the logical sum of the signals from all PMTs of layer 5, in order to obtain a uniform time-of-flight distribution across the full bar length, together with a dedicated calibration campaign for all ECAL modules.

Conclusions

The Deep Underground Neutrino Experiment (DUNE) represents the forthcoming frontier in neutrino oscillation measurements, leveraging a high-intensity accelerator beam to deliver the event samples required for precision tests of neutrino physics. Within the Near Detector complex, the task of the on-axis SAND apparatus is the characterization the absolute neutrino flux, its flavor content, and its temporal and spatial stability, thereby providing tight constraints on the systematic uncertainties that propagate to the oscillation analysis at the far detector.

SAND integrates a 0.6 T superconducting magnet, a high-granularity electromagnetic calorimeter, a $\sim$1 ton liquid-argon active target (GRAIN), and a modular, low-density target-tracker. This configuration combines magnetic spectrometry with calorimetry and topological reconstruction, enabling percent-level momentum resolution for final-state particles while supplying the calibration and control samples essential for flux and cross-section modeling.

The electromagnetic calorimeter (ECAL) is central to SAND's physics reach, supplying precise electromagnetic energy and timing measurements that complement magnetic spectrometry, enable robust photon and electron reconstruction with E/p cross-checks, provide interaction-time inference, and tag delayed neutral activity that constrains detector and flux systematics.

Within this framework, the present work delivered a complete ECAL software reconstruction chain -implemented and integrated in the SAND analysis environment- covering clustering, time and energy estimation, and quality controls, together with a truth-matching procedure that links reconstructed clusters to Monte Carlo information for unbiased performance and calibration studies.

Building on these tools, a calibration strategy suited to the underground environment -where the cosmic-ray flux is strongly suppressed- was developed using beam-induced muons as an abundant minimum-ionizing particle sample. The method has been exploited for energy intercalibration via the MiP peak and for timing alignment across all ECAL channels. Its feasibility was assessed through cell-level occupancy maps and dedicated distribution fits, indicating uniform sampling and stable reference points for the relative energy scale and time offsets.

In addition, a preliminary vertex reconstruction relying solely on calorimetric observables was realized, and its stability was examined under increasingly realistic conditions, including the presence of heterogeneous cluster topologies and interactions with vertices outside the ECAL volume. Collectively, these results -and the associated reconstruction software- establish a practical, data-driven path to ECAL intercalibration and time alignment in SAND, and provide a validated foundation for subsequent performance optimization and systematic-uncertainty control.

Complementary to the simulation and reconstruction developments, a dedicated cosmic-ray stand was commissioned at LNF to characterise individual ECAL modules under controlled conditions. The stand, equipped with the original KLOE readout chain and a custom DAQ system, enables the measurement of ADC and TDC responses to cosmic muons and serves as an essential test bench for validating the detector performance and calibration models implemented in the SAND framework. The preliminary results obtained from this setup demonstrate the consistency between measured and simulated signal shapes, confirming the robustness of the adopted calibration approach and providing a direct hardware measurement for future commissioning of the SAND ECAL modules.

Future work will focus on refining and extending this framework. On the simulation side, the beam-induced muon methods will be complemented by a quantitative study of the underground cosmic-ray flux, to assess whether cosmic muons can recover statistics in the horizontally oriented modules and be integrated into a combined calibration scheme. The global time reference t_0^G will be improved by incorporating tracker information and by enhancing the rejection of interactions originating outside the ECAL. The impact of realistic spill structure and pile-up will be studied once an official spill overlay becomes available. The absolute energy scale will be anchored to channels with known kinematics, such as $\pi^0 \to \gamma\gamma$, through dedicated studies of rates, selection purity and systematics.

On the hardware side, the cosmic-ray stand at INFN Frascati will evolve from its commissioning phase to a full calibration facility, with an improved trigger logic ensuring more uniform coverage along the modules and a calibration campaign for all ECAL barrel modules. The system will be then replicated and optimise to perform the same measurements on the ECAL EndCap modules. Together, these developments will complete and consolidate the calibration and monitoring programme for the SAND ECAL in view of DUNE operation.

Bibliography

[1] C. D. Ellis and W. A. Wooster. "The Average Energy of Disintegration of Radium E". In: *Proc. Roy. Soc. A* 117 (1927), pp. 109–123. DOI: 10.1098/rspa.1927.0168.

[2] W. Pauli. *Open letter to the group of radioactive people in Tübingen*. 1930.

[3] J. Chadwick. "Possible Existence of a Neutron". In: *Nature* 129 (1932), p. 312. DOI: 10.1038/129312a0.

[4] E. Fermi. "Versuch einer Theorie der β-Strahlen". In: *Zeitschrift für Physik* 88 (1934), pp. 161–177. DOI: 10.1007/BF01351864.

[5] C. L. Cowan et al. "Detection of the free neutrino: a confirmation". In: *Science* 124 (1956), pp. 103–104. DOI: 10.1126/science.124.3212.103.

[6] M. Goldhaber, L. Grodzins, and A. W. Sunyar. "Helicity of neutrinos". In: *Phys. Rev.* 109 (1958), pp. 1015–1017. DOI: 10.1103/PhysRev.109.1015.

[7] R. Davis, D. S. Harmer, and K. C. Hoffman. "Search for neutrinos from the sun". In: *Phys. Rev. Lett.* 20 (1968), pp. 1205–1209. DOI: 10.1103/PhysRevLett.20.1205.

[8] J. N. Bahcall et al. "Solar neutrinos. I. Theoretical". In: *Phys.Rev.Lett* 12 (1964), pp. 300–302. DOI: 10.1103/PhysRevLett.12.300.

[9] Q. R. Ahmad et al. "Direct evidence for neutrino flavor transformation from neutral-current interactions in the Sudbury Neutrino Observatory". In: *Phys. Rev. Lett.* 89 (2002). DOI: 10.1103/PhysRevLett.89.011301.

[10] Y. Fukuda et al. "Evidence for oscillation of atmospheric neutrinos". In: *Phys. Rev. Lett.* 81 (1998), pp. 1562–1567. DOI: 10.1103/PhysRevLett.81.1562.

[11] M. H. Ahn et al. "Measurement of neutrino oscillation by the K2K experiment". In: *Phys. Rev. D* 74 (2006). DOI: 10.1103/PhysRevD.74.072003.

[12] K. Eguchi et al. "First results from KamLAND: Evidence for reactor antineutrino disappearance". In: *Phys. Rev. Lett.* 90 (2003). DOI: 10.1103/PhysRevLett.90.021802.

[13] Carlo Giunti and Chung Wook Kim. *Fundamentals of Neutrino Physics and Astrophysics*. Ed. by Oxford: Oxford University Press. 2007.

[14] A. Cervera et al. "Golden measurements at a neutrino factory". In: *Nuclear Physics B* 579 (2000). Erratum: Nuclear Physics B **593**, 731 (2001), pp. 17–55. DOI: 10.1016/S0550-3213(00)00221-2. URL: https://arxiv.org/abs/hep-ph/0002108.

[15] B. T. Cleveland et al. "Measurement of the solar electron neutrino flux with the Homestake chlorine detector". In: *Astrophys. J.* 496 (1998), pp. 505–526. DOI: 10.1086/305343.

[16] P. Anselmann et al. (GALLEX Collaboration). "Solar neutrinos observed by GALLEX at Gran Sasso". In: *Phys. Lett. B* 285 (1992), pp. 376–389. DOI: 10.1016/0370-2693(92)91521-A.

[17] M. Altmann et al. (GNO Collaboration). "GNO solar neutrino observations: Results for GNO I". In: *Phys. Lett. B* 490 (2000), pp. 16–26. DOI: 10.1016/S0370-2693(00)00915-1.

[18] J. N. Abdurashitov et al. (SAGE Collaboration). "Measurement of the solar neutrino capture rate with gallium metal". In: *Phys. Rev. C* 60 (1999), p. 055801. DOI: 10.1103/PhysRevC.60.055801.

[19] John N. Bahcall, Aldo M. Serenelli, and Sarbani Basu. *New solar opacities, abundances, helioseismology, and neutrino fluxes*. Vol. 621. 2005, pp. L85–L88. DOI: 10.1086/428929.

[20] K. S. Hirata et al. (Kamiokande-II Collaboration). "Observation of 8B solar neutrinos in the Kamiokande-II detector". In: *Phys. Rev. Lett.* 66 (1991), pp. 9–12. DOI: 10.1103/PhysRevLett.66.9.

[21] Y. Fukuda et al. (Super-Kamiokande Collaboration). "Evidence for oscillation of atmospheric neutrinos". In: *Phys. Rev. Lett.* 81 (1998), pp. 1562–1567. DOI: 10.1103/PhysRevLett.81.1562.

[22] Q. R. Ahmad et al. (SNO Collaboration). "Direct evidence for neutrino flavor transformation from neutral-current interactions in the Sudbury Neutrino Observatory". In: *Phys. Rev. Lett.* 89 (2002), p. 011301. DOI: 10.1103/PhysRevLett.89.011301.

[23] G. Bellini et al. (Borexino Collaboration). "Precision measurement of the ^{7}Be solar neutrino interaction rate in Borexino". In: *Phys. Rev. Lett.* 107 (2011), p. 141302. DOI: 10.1103/PhysRevLett.107.141302.

[24] T. Araki et al. (KamLAND Collaboration). "Measurement of neutrino oscillation with KamLAND: Evidence of spectral distortion". In: *Phys. Rev. Lett.* 94 (2005), p. 081801. DOI: 10.1103/PhysRevLett.94.081801.

[25] K. S. Hirata et al. (Kamiokande-II Collaboration). "Observation of a small atmospheric ν_μ/ν_e ratio in Kamiokande". In: *Phys. Lett. B* 280 (1992), pp. 146–152. DOI: 10.1016/0370-2693(92)90788-6.

[26] R. Becker-Szendy et al. (IMB Collaboration). "Neutrino measurements with the IMB detector". In: *Phys. Rev. D* 46 (1992), pp. 3720–3724. DOI: 10.1103/PhysRevD.46.3720.

[27] M. Ambrosio et al. (MACRO Collaboration). "Measurements of atmospheric muon neutrino oscillations, global analysis of the data collected with MACRO detector". In: *Eur. Phys. J. C* 36 (2004), pp. 323–339. DOI: 10.1140/epjc/s2004-01973-7.

[28] W. W. M. Allison et al. (Soudan-2 Collaboration). "Neutrino oscillation effects in Soudan-2 upward-stopping muons". In: *Phys. Lett. B* 449 (1999), pp. 137–144. DOI: 10.1016/S0370-2693(99)00054-6.

[29] S. Adrián-Martínez et al. (ANTARES Collaboration). "Measurement of atmospheric neutrino oscillations with the ANTARES neutrino telescope". In: *Phys. Lett. B* 734 (2014), pp. 137–144. DOI: 10.1016/j.physletb.2014.05.070.

[30] M. G. Aartsen et al. (IceCube Collaboration). "Measurement of Atmospheric Neutrino Oscillations at 6–56 GeV with IceCube DeepCore". In: *Phys. Rev. Lett.* 120 (2018), p. 071801. DOI: 10.1103/PhysRevLett.120.071801.

[31] M. H. Ahn et al. (K2K Collaboration). "Indications of neutrino oscillation in a 250 km long-baseline experiment". In: *Phys. Rev. Lett.* 90 (2003), p. 041801. DOI: 10.1103/PhysRevLett.90.041801.

[32] P. Adamson et al. (MINOS Collaboration). "Measurement of neutrino oscillations with the MINOS detectors in the NuMI beam". In: *Phys. Rev. Lett.* 101 (2008), p. 131802. DOI: 10.1103/PhysRevLett.101.131802.

[33] K. Abe et al. (T2K Collaboration). "Indication of Electron Neutrino Appearance from an Accelerator-Produced Off-Axis Muon Neutrino Beam". In: *Phys. Rev. Lett.* 107 (2011), p. 041801. DOI: 10.1103/PhysRevLett.107.041801.

[34] P. Adamson et al. (NOvA Collaboration). "First measurement of electron neutrino appearance in NOvA". In: *Phys. Rev. Lett.* 116 (2016), p. 151806. DOI: 10.1103/PhysRevLett.116.151806.

[35] K. Abe et al. (T2K Collaboration). "Combined Analysis of Neutrino and Antineutrino Oscillations at T2K". In: *Phys. Rev. Lett.* 118 (2017), p. 151801. DOI: https://doi.org/10.1103/PhysRevLett.118.151801.

[36] F. P. An et al. (Daya Bay Collaboration). "Measurement of the Electron Antineutrino Oscillation with 1958 Days of Operation at Daya Bay". In: *Phys. Rev. Lett.* 121 (2018), p. 241805. DOI: 10.1103/PhysRevLett.121.241805.

[37] Y. Abe et al. "Measurement of θ_{13} in Double Chooz using neutron captures on hydrogen with novel background rejection techniques". In: *JHEP* 01 (2016), p. 163. DOI: 10.1007/JHEP01(2016)163.

[38] J. K. Ahn et al. (RENO Collaboration). "Observation of Reactor Electron Antineutrino Disappearance in the RENO Experiment". In: *Phys. Rev. Lett.* 108 (2012), p. 191802. DOI: 10.1103/PhysRevLett.108.191802.

[39] A. Aguilar et al. (LSND Collaboration). "Evidence for neutrino oscillations from the observation of $\bar{\nu}_e$ appearance in a $\bar{\nu}_\mu$ beam". In: *Phys. Rev. D* 64 (2001), p. 112007. DOI: 10.1103/PhysRevD.64.112007.

[40] A. A. Aguilar-Arevalo et al. (MiniBooNE Collaboration). "Significant Excess of Electronlike Events in the MiniBooNE Short-Baseline Neutrino Experiment". In: *Phys. Rev. Lett.* 121 (2018), p. 221801. DOI: 10.1103/PhysRevLett.121.221801.

[41] G. Mention et al. "The Reactor Antineutrino Anomaly". In: *Phys. Rev. D* 83 (2011), p. 073006. DOI: 10.1103/PhysRevD.83.073006.

[42] C. Giunti and M. Laveder. "Statistical significance of the gallium anomaly". In: *Phys. Rev. C* 83 (2011), p. 065504. DOI: 10.1103/PhysRevC.83.065504.

[43] I. Esteban et al. "The fate of hints: updated global analysis of three-flavor neutrino oscillations". In: *JHEP* 09 (2020), p. 178. DOI: 10.1007/JHEP09(2020)178. arXiv: 2007.14792.

[44] M. Gonzalez-Garcia, M. Maltoni, T. Schwetz, et al. *NuFIT 5.2 (2024): Three-flavor global analysis of neutrino oscillation parameters*. http://www.nu-fit.org. Accessed 2025-08-16.

[45] K. Abe et al. (T2K Collaboration). "Constraint on the matter–antimatter symmetry-violating phase in neutrino oscillations". In: *Nature* 580 (2020), pp. 339–344. DOI: 10.1038/s41586-020-2177-0.

[46] K. Abe et al. (T2K Collaboration). "Improved constraints on neutrino mixing from the T2K experiment with 3.13×10^{21} protons on target". In: *Phys. Rev. D* 103.11 (2021), p. 112008. DOI: 10.1103/PhysRevD.103.112008. arXiv: 2101.03779.

[47] M. A. Acero et al. (NOvA Collaboration). "An improved measurement of neutrino oscillation parameters by the NOvA experiment". In: *Phys. Rev. D* 106.3 (2022), p. 032004. DOI: 10.1103/PhysRevD.106.032004. arXiv: 2108.08219.

[48] DUNE Collaboration. *Long-Baseline Neutrino Facility (LBNF) and Deep Underground Neutrino Experiment (DUNE): Conceptual Design Report, Volume 2: The Physics Program for DUNE at LBNF*. Tech. rep. Fermilab, 2016. DOI: 10.2172/1250883. arXiv: 1512.06148.

[49] K. Abe et al. (Hyper-Kamiokande Proto-Collaboration). "Hyper-Kamiokande Design Report". In: *arXiv preprint* (2018). arXiv: 1805.04163.

[50] B. Abi and others (DUNE Collaboration). "Deep Underground Neutrino Experiment (DUNE) Near Detector Conceptual Design Report". In: *Instruments* 5.4 (2021), p. 31. DOI: 10.3390/instruments5040031. arXiv: 2103.13910.

[51] B. Abi and others (DUNE Collaboration). "Deep Underground Neutrino Experiment (DUNE), Far Detector Technical Design Report, Volume II: DUNE Physics". In: *Eur. Phys. J. C* 80 (2020), p. 978. DOI: 10.1140/epjc/s10052-020-08456-z. arXiv: 2002.03005.

[52] James Strait et al. *Long-Baseline Neutrino Facility (LBNF) and Deep Underground Neutrino Experiment (DUNE): Conceptual Design Report, Volume 3: Long-Baseline Neutrino Facility for DUNE*. Tech. rep. Fermilab, 2016. arXiv: 1601.05823 [physics.ins-det]. URL: https://arxiv.org/abs/1601.05823.

[53] R. Alvarez-Garrote et al. "Measurement of the absolute efficiency of the X-ARAPUCA photon detector for the DUNE Far Detector 1". In: (2024). arXiv: 2405.12014 [physics.ins-det]. URL: https://arxiv.org/abs/2405.12014.

[54] A. Abed Abud et al. (DUNE Collaboration). "Snowmass Neutrino Frontier: DUNE Physics Summary". In: (Mar. 2022). arXiv:2203.06100 [hep-ex]. arXiv: 2203.06100 [hep-ex].

[55] *KLOE-2 Experiment*. https://www.lnf.infn.it/kloe2/. Accessed: February 10, 2026.

[56] M. Adinolfi et al. "The KLOE electromagnetic calorimeter". In: *Nuclear Instruments and Methods in Physics Research Section A: Accelerators, Spectrometers, Detectors and Associated Equipment* 482.1 (2002), pp. 364–386.

ISSN: 0168-9002. DOI: 10.1016/S0168-9002(01)01502-9. URL: https://doi.org/10.1016/S0168-9002(01)01502-9.

[57] M.Anelli et al. "Measurement of the detection efficiency of the KLOE calorimeter for neutrons between 22 and 174 MeV". In: *Nuclear Instruments and Methods in Physics Research Section A: Accelerators, Spectrometers, Detectors and Associated Equipment* 598.1 (2009), pp. 244–247. URL: https://doi.org/10.1016/j.nima.2008.08.120.

[58] *DUNE Geometry Description*. https://github.com/DUNE/dunendggd. Accessed: February 10, 2026.

[59] C. Andreopoulos et al. "The GENIE Neutrino Monte Carlo Generator". In: *Nucl. Instrum. Meth. A* 614 (2010), pp. 87–104. DOI: 10.1016/j.nima.2009.12.009. arXiv: 0905.2517 [hep-ph].

[60] Clark McGrew et al. *edepsim*. https://github.com/ClarkMcGrew/edep-sim. Accessed: February 10, 2026.

[61] T. Heindl et al. "The scintillation of liquid argon". In: *EPL (Europhysics Letters)* 91.6 (2010), p. 62002. DOI: 10.1209/0295-5075/91/62002. URL: http://stacks.iop.org/0295-5075/91/i=6/a=62002.

[62] DUNE Collaboration. *SANDReco*. https://github.com/DUNE/sandreco. Accessed: February 10, 2026.

[63] F. Ambrosino et al. "Data handling, reconstruction, and simulation for the KLOE experiment". In: *Nucl. Instrum. Meth. A* 534 (2004), pp. 403–433. DOI: 10.1016/j.nima.2004.07.190. URL: https://www.sciencedirect.com/science/article/pii/S0168900204015633.

[64] DUNE Collaboration, SAND ECAL. *ECAL-PID: Electromagnetic Calorimeter Truth matching algorithm (SAND/DUNE)*. https://baltig.infn.it/dune/analyses/ecal-pid/. INFN GitLab repository, branch `develop`. Accessed: February 10, 2026. 2025.

[65] DUNE Collaboration. *edep-reader*. https://baltig.infn.it/dune/edep-reader. INFN GitLab repository. Accessed: February 10, 2026. 2025.

[66] CAEN S.p.A. *CAENVMELib Library*. Accessed: 2025-10-08. 2024. URL: https://www.caen.it/products/caenvmelib-library/.